HIGH SPEED AND HIGH EFFICIENCY INFRARED PHOTODETECTORS

A DISSERTATION
SUBMITTED TO THE DEPARTMENT OF PHYSICS
AND THE INSTITUTE OF ENGINEERING AND SCIENCES
OF BİLKENT UNIVERSITY
IN PARTIAL FULFILLMENT OF THE REQUIREMENTS
FOR THE DEGREE OF
DOCTOR OF PHILOSOPHY

By
İBRAHİM KİMUKİN
DECEMBER 2004

I certify that I have read this thesis and that in my opinion it is fully adequate, in scope and in quality, as a dissertation for the degree of Doctor of Philosophy.

Prof. Ekmel Özbay (Supervisor)

I certify that I have read this thesis and that in my opinion it is fully adequate, in scope and in quality, as a dissertation for the degree of Doctor of Philosophy.

Asst. Prof. Oğuz Gülseren

I certify that I have read this thesis and that in my opinion it is fully adequate, in scope and in quality, as a dissertation for the degree of Doctor of Philosophy.

Assoc. Prof. Ahmet Oral

I certify that I have read this thesis and that in my opinion it is fully adequate, in scope and in quality, as a dissertation for the degree of Doctor of Philosophy.

_____

Asst. Prof. Özgür Aktaş

I certify that I have read this thesis and that in my opinion it is fully adequate, in scope and in quality, as a dissertation for the degree of Doctor of Philosophy.

_____

Prof. Tayfun Akın

Approved for the Institute of Engineering and Sciences:

_____

Prof. Mehmet Baray,
Director of Institute of Engineering and Sciences

Abstract

HIGH SPEED AND HIGH EFFICIENCY INFRARED PHOTODETECTORS

İbrahim Kimukin

Ph. D. in Physics

Supervisor: Prof. Ekmel Özbay

December 2004

The increasing demand for telecommunication systems resulted in production of high performance components. Photodetectors are essential components of optoelectronic integrated circuits and fiber optic communication systems. We successfully used resonant cavity enhancement technique to improve InGaAs based p-i-n photodetectors. The detectors had 66% peak quantum efficiency at 1572 nm which showed 3 fold increases with respect to similar photodetector without resonant cavity. The detectors had 28 GHz 3-dB bandwidth at the same time. The bandwidth efficiency product for these detectors was 18.5 GHz, which is one of the best results for InGaAs based vertical photodetector.

The interest in high speed photodetectors is not limited to fiber optic networks. In the recent years, data communication through the air has become popular due to

ease of installation and flexibility of these systems. Although the current systems still operate at 840 nm or 1550 nm wavelengths, the advantage of mid-infrared wavelengths will result in the production of high speed lasers and photodetectors. InSb based p-i-n type photodetectors were fabricated and tested for the operation in the mid-infrared (3 to 5 μm) wavelength range. The epitaxial layers were grown on semi-insulating GaAs substrate by molecular beam epitaxy method. The detectors had low dark noise and high differential resistance around zero bias. Also the responsivity measurements showed 49% quantum efficiency. The detectivity was measured as 7.98×10^{9} cm $Hz^{1/2}/W$ for 60 μm diameter detectors. Finally the high speed measurements showed 8.5 and 6.0 GHz bandwidth for 30 μm and 60 μm diameter detectors, respectively.

Keywords: Photodetector, high speed, high efficiency, resonant cavity enhancement, infrared wavelengths.

Özet

YÜKSEK HIZLI VE YÜKSEK VERİMLİ KIZILÖTESİ FOTODEDEKTÖRLER

İbrahim Kimukin
Fizik Doktora
Tez Yöneticisi: Prof. Ekmel Özbay
Aralık 2004

Telekomnikasyon sistemlerine ilginin artması yüksek performanslı elemanların üretimiyle sonuçlanmıştır. Fotodedektörler optoelektronik entegre devrelerin ve fiber iletiim sistemlerinin önemli bir parçasıdır. Resonant çınlaç arttırımı tekniğinini InGaAs temelli p-i-n tipi fotodedektörleri geliştirmek için kullandık. Dedektörlerin 1572 nm'deki %66 tepe kuantum verimi rezonatörsüz benzer bir dedektöre göre 3 kat fazladır. Dedektörler aynı zamanda 28 GHz 3-dB bantralığına

sahiptir, ki bu değerler InGaAs temelli düşey fotodedektörler için en iyi sonuçlardan biridir.

Yüksek hızlı fotodedektörlere ilgi sadece fiber optic ağlar ile sınırlı değildir. Yakın zamanda havadan data iletimi kolay kurulum ve değişken yapılarından dolayı populer hale gelmiştir. Hernekadar şu anda kullanılan sistemler 840 nm ve 1550 nm de çalışsa da, orta-kızılötesi dalagaboylarının avantajı yüksek hızlı lazer ve fotodedektörlerin üretimine sebep olacaktır. InSb temelli p-i-n tipi dedektörler orta-kızılötesi dalagaboylarında (3 ten 5 μm'ye) kullanılmak üzere üretilip testedildi. Dedektör katmanları yarı-yalıtkan GaAs altaşın üzerine moleküler ışın demeti metodu ile büyütüldü. Dedektörler sıfır volt civarında düşük karanlık akım ve yüksek dirence sahiptiler. 60 μm çaplı dedektörlerin hassasiyeti 7.98×10^{9} cm $Hz^{1/2}/W$ olarak ölçüldü. Son olarak yüksek hız ölçümlerine göre 30 μm ve 60 μm çaplı dedektörlerin hızları sırasıyla 8.5 GHz ve 6.0 GHz'tir.

Anahtar Kelimeler: Fotodedektör, yüksek hız, yüksek verim, resonant çınlaç arttırımı, kızılötesi dalgaboyları.

Acknowledgements

It is my pleasure to express my deepest gratitude to my supervisor Prof. Ekmel Özbay for his invaluable guidance, motivation, encouragement, confidence, understanding, and endless support. My graduate study under his supervision was my lifetime experience. It was an honor to work with him, and I learned a lot from his superior academic personality.

I would like to thank Prof. Orhan Aytür and Dr. Tolga Kartaloğlu for their help in high speed measurements in the infrared wavelengths. I would like to thank Prof. Cengiz Beşikçi, Selçuk Özer, and Orkun Cellek for their help in responsivity measurements of InSb photodetectors.

I also thank the members of the thesis committee, Asst. Prof. Oğuz Gülseren, Assoc. Prof. Ahmet Oral, Asst. Prof. Özgür Aktaş, and Prof. Tayfun Akın for their useful comments and suggestions.

I would like to thank all the former and present members of Advanced Research Laboratory for their continuous support. I want to especially thank the group members of the detector research team: Necmi Bıyıklı, Bayram Bütün,

Turgut Tut. It was a pleasure to work with these hard-working guys in the same group. Other special thanks go to Murat Güre and Ergün Kahraman for their technical help and keeping our laboratory in good condition.

Finally I would express my endless thank to my family for their understanding and continuous moral support. Very special thanks belong to my wife, Sevcan, for her endless moral support, understanding, and love.

Contents

List of Figures

List of Tables

Chapter 1

Introduction

The invention of the telephone led to an enormous world wide telecommunication network. Especially during and after the Second World War, the demand for the calling services resulted to both cheaper and faster services. The invention of the first solid-state transistor in 1947, and then the integrated circuit opened the age of computing and communication [1]. In 1960's researchers developed the first laser [2].

The development of the first commercially feasible optical fiber in 1970's made the fiber optic communication a promising candidate for telecommunication [3]. In the early 1980's satellites capable of carrying nearly 100,000 simultaneous calls are used for telephone calls. Demand for the faster, cheaper, and less noisy communication made the first transatlantic undersea fiber-optic telephone cable possible that replaced the copper one that had been installed in 1956. That was the first fiber-optic revolution in telecommunication.

The second revolution came with the introduction of wavelength division multiplexing (WDM). Telephone companies has laid cables containing 24 to 36 fibers with 2.5 Gbit/s rate, many had been reserved as “dark fiber”. But the tremendous traffic has crowded these cables that once seemed so

voluminous. This demand was due to the growth of the Internet, and the demand for more information transform for entertainment and communication. In the mid 1990's, companies began using systems capable of transmitting at four wavelengths, and soon this number increased to eight. Nowadays, systems with 40 channels of 10 Gb/s, or 80 channels of 2.5 Gb/s are available to be used with dispersion managed fibers [4].

This high demand for better fiber optics communication systems led scientist and engineers to work on components like lasers, modulators, photodetectors, optical amplifiers, and optical fibers. The optical fiber offers an operation bandwidth up to tens of THz. The research effort in optoelectronics is devoted to fully exploit the fiber bandwidth. This can be possible with high performance components.

Due to the properties of the commercial silica based fibers, optoelectronic research focused at three wavelengths, where the minimum attenuation occurs [5]. First one is located at 850 nm, which is called the first optical window. GaAs based detectors are usually used for the detection. Local area networks use this window, because the high loss in this wavelength prohibits the communication for long distances. These systems need only multimode fiber and transmitter, hence they are cheap. On the other hand, the second and the third windows are located at 1310 and 1550 nm respectively. The loss in these wavelengths is much less than the first optical window. Due to low loss, these wavelengths are used for long distance fiber optic communication. These systems require high speed modulator, detectors, and repeaters. Semiconductor based photodiodes demonstrate excellent features to fulfill the requirements of high speed optoelectronic receivers. GaAs and InGaAs are the most studied materials for high speed photodetection. Photodetectors have been demonstrated bandwidth capabilities as high as 200

GHz [6-9]. However, the efficiencies of these detectors have been less than 10%, due to thin absorption layer needed for short transit time.

Resonant cavity enhanced (RCE) photodetectors offer the possibility of overcoming this limitation of bandwidth-efficiency product of conventional photodetectors [10]. The RCE photodetectors are based on the enhancement of the optical field inside a Fabry-Perot cavity. This enhancement allows the usage of thinner active layers, which minimizes the transit time without sacrificing the quantum efficiency. This thesis reports the development of high efficiency photodetectors with the use of RCE effect in variety of our detectors.

Chapter 2 reviews the theory of photodetectors. It also examines the transport of carriers, and the high speed design. The chapter summarizes the theory of resonant cavity enhancement (RCE) and presents the simulation results of the RCE photodetectors. Finally it includes the techniques used for the optical design of multilayer photodetectors.

Chapter 3 gives the details of the fabrication steps. Details of the fabrication steps are also given. This chapter also includes the measurement setups and procedures used during the characterization.

Chapter 4 explains the design, fabrication and characterization of InGaAs based pin type photodetector. This detector includes RCE design for the operation around 1550 nm. The fabrication procedure is given with details. The results of the current-voltage, responsivity, and high-speed measurements are given at the characterization part.

Chapter 5 is devoted to InSb based photodetectors. Design, fabrication and measurement details are presented. This detector was designed for the operation in the 3–5 μm wavelength range, so that can be used for detection in the mid-infrared region. The design and fabrication were done at Physics Department of Bilkent University. Some of the measurements were done in

collaboration with the Electrical and Electronics Engineering Department of Bilkent University and Middle East Technical University.

Chapter 2

Theoretical Background

This chapter briefly explains the photodetector operation and the resonant cavity enhancement (RCE) technique that is used to achieve higher responsivity. Also design basics are presented. Section 2.1 explains the operation of a semiconductor junction photodetector. Basic formulation of the RCE technique is presented in Section 2.2. Finally, Section 2.3 explains the design basics and calculation methods of optical properties of multi-layered structures.

2.1 Photodetectors

Photodetectors can be classified into two categories: thermal detectors and quantum detectors. Thermal detectors sense the radiation by its heating effect. Thermal detectors have the advantage of wide spectral range and operation at the room temperature, but they are limited as far as speed and sensitivity are concerned. Bolometers, thermistors, pyroelectric detectors are widely used thermal detectors.

Operation of quantum detectors depend on the discrete nature of photons which can transfer energy of individual particles (electron and hole) giving rise to a photocurrent. These devices are characterized by very high sensitivity, high speed but limited spectral response. Photoemissive,

photovoltaic, and photoconductive detectors are classified in this category. The conductivity change in the photoconductive detectors is proportional to the intensity of the radiation falling on the semiconductor. Rectifying junctions are the basis of the photovoltaic detectors. Under the illumination, the excess carriers created within the semiconductor generate a proportional output current. In our work, we mostly design and fabricate photovoltaic detectors.

2.1.1 Photodetector Basics

A photovoltaic photodetector contains a depleted region with high electric field. When photons are absorbed, charged carriers are generated inside the depletion region. The photogenerated electron holes move in opposite directions until they reach a highly doped contact layer or recombine. While the charges move in the depletion region, a potential difference is created across it. This causes a current flow through the circuit that the detector is connected. The depletion region can be formed in different ways. Most popular are the p-n and metal-semiconductor junctions.

The most popular photodetector type with a p-n junction is *p-i-n* photodetector. In this structure, a lightly doped layer is placed between two highly doped layers, where ohmic contacts are made. The lightly doped layer is usually chosen to be n-type, hence a depletion region starting from the p-i junction is formed. The width of the depletion region can be controlled with the doping and applied voltage.

The highly doped layers are grown with a semiconductor having higher energy band than the intrinsic region. In this way, all the incoming light is absorbed in i-layer where the electric field intensity is high. As a result, the diffusion of photogenerated carriers from the highly doped regions is not present, and the speed of the photodetector is only limited by the transit time of

carriers and the junction capacitance. The only difficulty in such hetero junctions is the band discontinuities. If the discontinuity is high, charge trapping at the interfaces degrades the performance of the photodetector. Figure 2.1 shows an energy band diagram of a homojunction *p-i-n* photodetector.

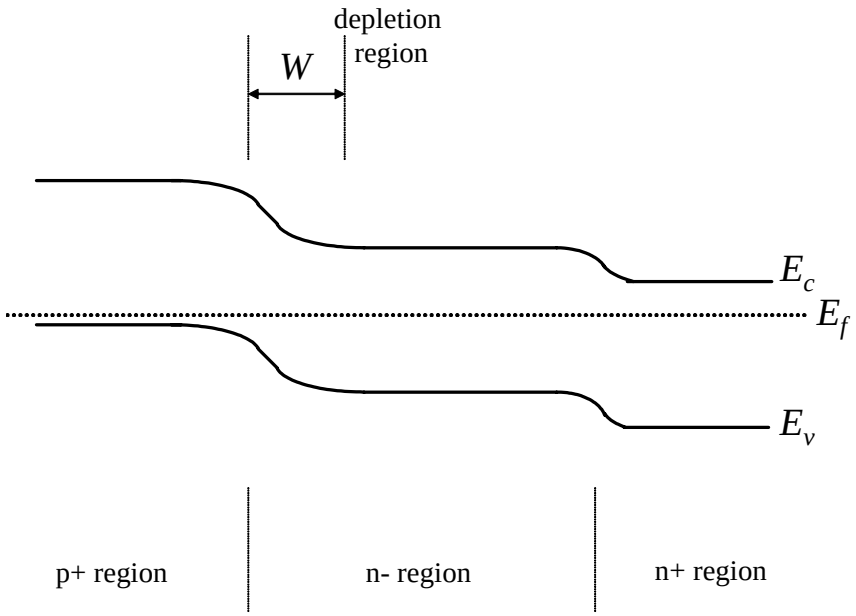

Figure 2.1: Energy diagram of a *p-i-n* photodetector.

When we investigate the current-voltage characteristics of the p-i-n photodetector, we see that the current is due to the sum of the diffusion and the generation-recombination currents inside the intrinsic region. Then the current density can be written as:

$$J = \left(\frac{qD_p n_i^2}{L_p N_D} + \frac{qD_n n_i^2}{L_n N_A} \right) \left[\exp\left(\frac{qV_A}{kT} \right) - 1 \right] + \frac{qWn_i}{2\tau} \left[\exp\left(\frac{qV_A}{2kT} \right) - 1 \right] \qquad (2.1)$$

Here W is the width of the depletion region, D_n and D_p are the diffusion coefficient of minority carriers, L_n and L_p are the diffusion lengths, N_d and N_a are the doping concentration of the n+ and p+ regions. n_i is the intrinsic carrier

concentration, τ is the carrier lifetime, and q is the electron charge. Usually N_A and N_D are very high, and the diffusion current is negligible. Forward current has an exponential dependence on the applied voltage. The reverse current (dark current if there is no illumination) is constant and given by:

$$J_{G-R} = \frac{qWn_i}{2\tau} \tag{2.2}$$

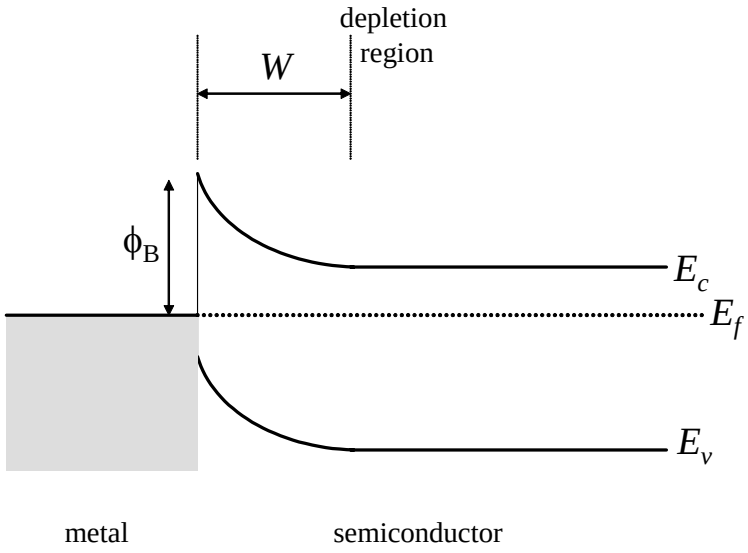

Figure 2.2: Energy diagram of a Schottky photodetector.

On the other hand, a Schottky type photodetector consists of a metal-semiconductor junction and the depletion region. The theory of rectification in metal-semiconductor junction was developed in 1930's by W. Schottky who attributed rectification to a space-charge layer in the semiconductor [11]. Figure 2.2 shows the energy band diagram after the contact is made and the equilibrium has been established. When the two substances are brought into intimate contact, electrons from the conduction band of the semiconductor, which have higher energy than the electrons in the metal, flow into the metal.

This process continues until the Fermi level on both sides is brought into coincidence. As the electrons move from semiconductor to metal, the free electron concentration in the semiconductor region near the boundary decreases. The length of this region is given by [12]:

$$W = \sqrt{\frac{2\varepsilon}{qN_d}(V_{bi} - V)} \tag{2.3}$$

where, N_d is the ionized donor density, ε is the dielectric constant of the semiconductor, V_{bi} is the built-in potential, V is the applied voltage. As the separation between the conduction band edge E_c and the Fermi level E_f increases with decreasing electron concentration and in thermal equilibrium E_f remains constant, the conduction band edge bends up. The conduction band electrons which cross over the metal leave a positive charge of ionized donor atoms behind, so the semiconductor region near the metal gets depleted of mobile electrons. Consequently an electric field is established from the semiconductor to the metal. The build-in potential due to that electric field is given by the difference of the work function of metal (ϕ_m) and semiconductor (ϕ_s):

$$qV_{bi} = \phi_m - \phi_s \tag{2.4}$$

The current transport in the metal-semiconductor contacts is mainly due to majority carriers, in contrast to p-n junctions. There are four different mechanisms by which the carrier transport can occur: (1) thermionic emission over the barrier, (2) tunneling through the barrier, (3) carrier recombination (or generation) in the depletion region, and (4) carrier recombination in the neutral region of the semiconductor. Usually the first process is the dominant mechanism in Schottky barrier junctions in Si and GaAs and leads to the ideal diode characteristics.

The thermionic emission theory is derived by Bethe [13] for high-mobility semiconductors, and the diffusion theory is derived by Schottky [11] for low-mobility semiconductors. A synthesis of the thermionic emission and diffusion approaches has been proposed by Crowell and Sze [14]. The complete expression of the J-V characteristics is given by:

$$J = J_s\left[\exp\left(\frac{qV_A}{nkT}\right)-1\right] \tag{2.5}$$

$$J_s = A^{**}T^2\exp\left(-\frac{q\phi_B}{kT}\right) \tag{2.6}$$

where A^{**} is the effective Richardson constant.

Some metal-semiconductor-metal (MSM) photodetectors have Schottky contacts while some of them have ohmic contacts between the metal and semiconductor.

2.1.2 Photodetector Structures

Conventionally, the photodetectors are illuminated vertically, i.e., normal to the epitaxial layers. Usually incoming light first travels through the detector layers, and the optical power not absorbed pass through the substrate, as shown in Figure 2.3(a). In some cases light is launched from the bottom, initially through the substrate (usually thinned for lower absorption) and finally through the detector layers (as shown on Figure 2.3(b)). This type of illumination is very easy to couple all the incident power into the active area of the photodetector. In some cases, the top contact (either ohmic or Schottky) is used as the mirror. In this case optical power passes through the active layer twice; hence the quantum efficiency is increased.

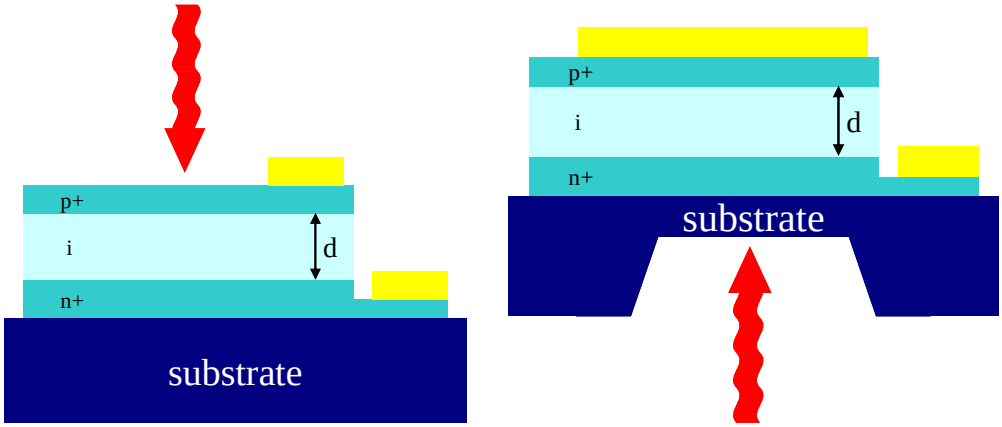

Figure 2.3: Crossection of vertical illuminated photodetectors.

The other possible illumination is from the edge of the wafer as shown on Figure 2.4. The width and the thickness of the waveguide must be small to operate the waveguide in the singe mode. In this configuration, the coupling of the incident power into the waveguide is the main problem. The coupled light travels along the waveguide, generating electron hole pairs. If the length is high enough, all the power can be absorbed in the waveguide. The loss due to the absorption in the contact metals must be minimized.

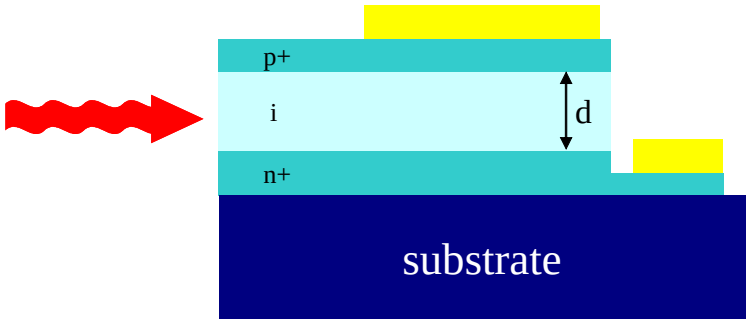

Figure 2.4: Crossection of edge illuminated photodetectors.

2.1.3 Photodetector Operation

We observe the transit of the photogenerated carriers inside the depletion region. We start with an optical excitation at some specific point. Modeling the depletion region as a parallel plate capacitor, we obtain the current flowing out of the capacitor as:

$$I_{out}(t) = \begin{cases} I_1 = \dfrac{q}{d}(v_e + v_h) & ,0 < t < t_h \\ I_2 = \dfrac{q}{d} v_e & ,t_h < t < t_e \end{cases} \qquad (2.7)$$

Here d is the width of the depletion region; v_e, and v_h are the drift velocity of electron and holes, respectively; and t_e, and t_h are the time of transit for electrons and holes, respectively. We assumed that the excitation is made at a location where $t_e > t_h$.

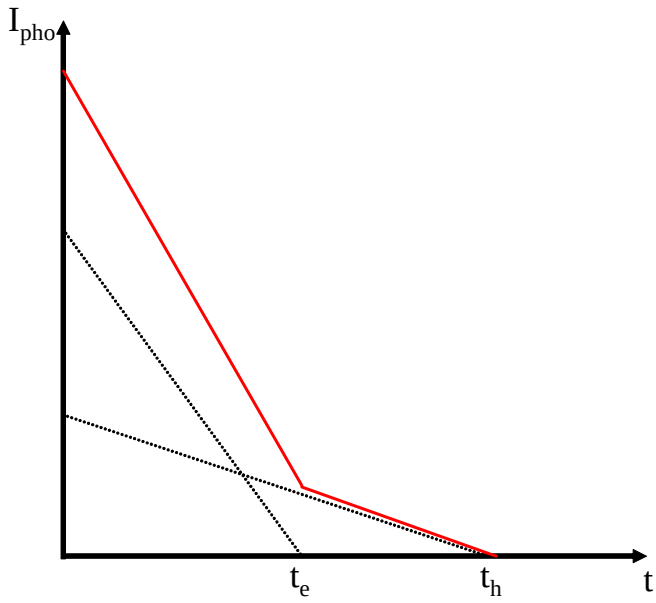

Figure 2.5: Output current versus time for a constant illumination across the depletion region.

For a constant illumination through the depletion region, the results found in Eq. 2.7 must be integrated for all points inside the depletion region. The result of this integration is shown in Figure 2.5. Here it is assumed that $v_e > v_h$, which is the case for most of the semiconductors. The measured voltage on the load resistance will depend on the capacitance of the photodetector and the load resistance.

The junction resistance (R_j) is much higher than both the series (R_s) and the load resistance (R_L), so that it can be neglected in the calculations. The junction capacitance and the series resistance form a low pass filter that limits the bandwidth of the photodetector. The junction capacitance can be simply found as $C_j = \varepsilon A/d$, where ε is the electrical permittivity, A is the area of the photodetector, and d is the width of the depletion region.

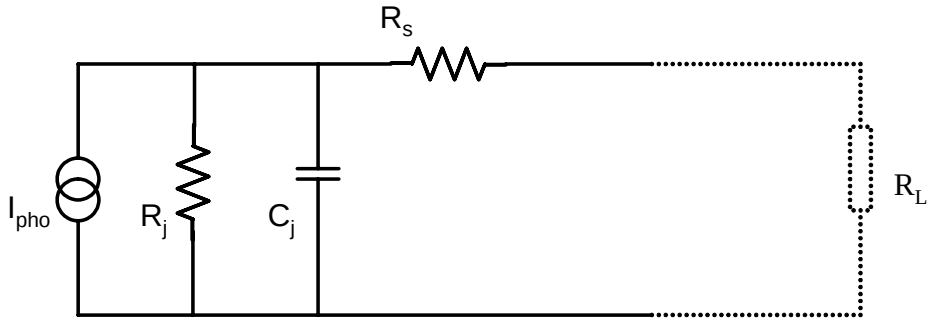

Figure 2.6: Small signal equivalent circuit for photodetector.

The 3-dB roll-off frequency of the RC limited photodetector can be found as:

$$f_{RC} = \frac{1}{2\pi} \frac{1}{(R_L + R_s)C_j} \tag{2.8}$$

The other limit on the frequency response is the transit time of the carriers. The 3-dB roll-off frequency for transit limited case is:

$$f_{tr} = 0.45 \frac{v_{car}}{d} \tag{2.9}$$

where, v_{car} is the velocity of the carriers.

Another important characteristic of the photodetector is the quantum efficiency or the responsivity. When a photon, with wavelength λ whose energy is larger than the bandgap, is absorbed in the depletion region, an electron hole pair is generated. These carriers are swept away by the electric field. The number of electrons generated per incident photon is defined as the quantum efficiency, which is expressed as [15]:

$$\eta = \frac{I_p / q}{P_{opt} / (h\nu)} \tag{2.10}$$

where, I_p is the photo-generated current, and P_{opt} is the optical power at frequency ν. The relation between the responsivity and the quantum efficiency can be written as:

$$\eta = \frac{1.24 \times \Re}{\lambda} \tag{2.11}$$

where, λ is in microns, and responsivity ($\Re$) is in amps per watt (A/W).

For classical single pass, vertical illuminated photodetectors, the quantum efficiency is given by:

$$\eta = (1 - R)(1 - e^{-\alpha d}) \tag{2.12}$$

where, *R* is the reflectivity of the front surface, α is the power absorption coefficient, and *d* is the thickness of the active layer. So, to maximize the quantum efficiency, the surface reflectivity must be minimized, and single pass absorption must be maximized. Reflectivity can be minimized using anti-reflection coatings, and single pass absorption can be maximized by increasing layer thickness.

For the transit time limited photodetector, the thickness is small, and αd is much smaller than one. In this case, the quantum efficiency can be reformulated as:

$$\eta = (1 - R)\alpha d \tag{2.13}$$

In this case, the bandwidth efficiency product can be obtained as:

$$f_{tr} \times \eta = 0.45(1-R)\alpha v_{car} \tag{2.14}$$

which is independent of the active layer thickness.

2.2 Resonant Cavity Enhancement

For transit time limited photodetectors, the depletion region must be kept thin enough to achieve high-speed operation. On the other hand, for high quantum efficiency, the depletion layer must be sufficiently thick to absorb a high fraction of incident light. To overcome this trade off between the response speed and efficiency, a conventional photodetector with a thinner active layer can be placed inside a Fabry-Perot micro-cavity. Thin active layer results in lower transit time, but performance of the photodetector with the help of the cycling of the optical power inside the cavity, is increased [10]. This kind of enhancement of the quantum efficiency is called Resonant Cavity Enhancement (RCE). The RCE effect was proposed in 1990 and was applied to a broad range of detectors: Schottky [16, 17], p-i-n [18-20], avalanche [21, 22], and MSM [50] photodiodes.

2.2.1 RCE Formulation and Optimization

Figure 2.7 shows a generalized structure of an RCE photodetector. Although metal coatings can be used as mirror, lossless distributed Bragg reflectors (DBR) are used as mirrors of the micro-cavity, as the aim is to achieve maximum efficiency. The active layer, where the absorption occurs, is placed between these mirrors. L is the length of the cavity, and d is the thickness of the active layer. The field reflection coefficients of the top and bottom reflectors are $r_1 e^{-i\varphi_1}$ and $r_2 e^{-i\varphi_2}$, where φ_1 and φ_2 are phase shifts due to the light penetration into the mirrors.

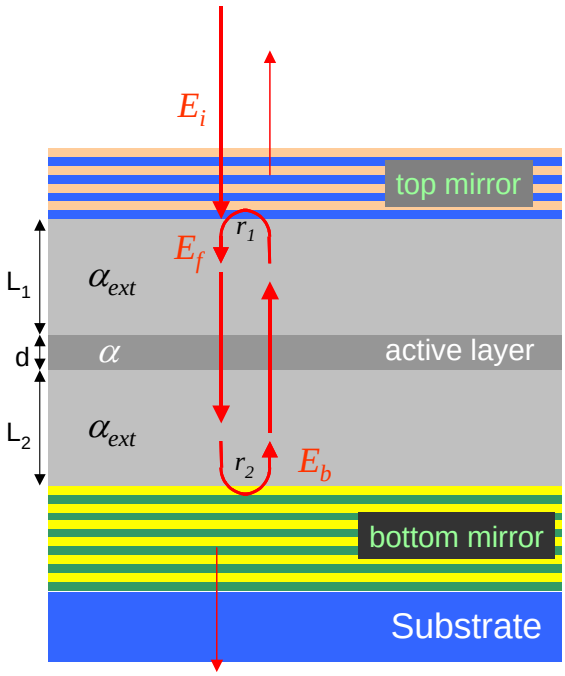

Figure 2.7: Generalized structure of a resonant cavity enhanced photodetector.

E_i represents the electric field amplitude of the incident light, while E_f is the forward traveling wave at $z = 0$, and E_b is the backward traveling wave at $z = L = L_1+d+L_2$. In the cavity, E_f is composed of the transmitted wave from the first mirrors and the reflected wave from the second mirror. Therefore, the forward traveling wave, E_f, at $z = 0$ can be obtained in a self-consistent way:

$$E_f = t_1 Ei + r_1 r_2 e^{-\alpha d - \alpha_{ext}(L_1+L_2)} e^{-i(2\beta L+\varphi_1+\varphi_2)} E_f \qquad (2.15)$$

where, $\beta = 2\pi n/\lambda_0$, α and α_{ext} are the absorption coefficients of the active and cavity layers respectively. Solving for E_f gives us

$$E_f = \frac{t_1}{1 - r_1 r_2 e^{-\alpha d - \alpha_{ext}(L_1+L_2)} e^{-i(2\beta L+\varphi_1+\varphi_2)}} Ei \qquad (2.16)$$

and the backward traveling wave, E_b, at z = L can be expressed as:

$$E_b = r_2 e^{\frac{-\alpha d}{2}} e^{\frac{-\alpha_{ext}(L_1+L_2)}{2}} e^{-i(\beta L+\varphi_2)} E_f \tag{2.17}$$

The optical power inside the resonant cavity is proportional to the refractive index of the medium and the square of the electric field amplitude.

$$P(z) \propto \left|E(z)\right|^2 n \tag{2.18}$$

If we neglect the standing wave effect, the power absorbed in the active layer in terms of the incident power is given by:

$$P_a = \frac{(1-r_1^{\,2})(e^{-\alpha_{ext}L_1} + r_2^{\,2} e^{-\alpha_{ext}L_2-\alpha_c L})(1-e^{-\alpha d})}{1-2r_1 r_2 e^{-\alpha_c L}\cos(2\beta L+\varphi_1+\varphi_2)+(r_1 r_2)^2 e^{-2\alpha_c L}} P_i \tag{2.19}$$

where $\alpha_c = (\alpha_{ext}(L1+L2)+\alpha d)/L$. Under the assumption that all the photogenerated carriers contribute to the current, η is the ratio of the absorbed power to the incident optical power, i.e., $\eta = P_a/P_i$. Hence:

$$\eta = \left[\frac{(e^{-\alpha_{ext}L_1} + R_2 e^{-\alpha_{ext}L_2-\alpha_c L})}{1-2\sqrt{R_1 R_2}e^{-\alpha_c L}\cos(2\beta L+\varphi_1+\varphi_2)+R_1 R_2 e^{-\alpha_c L}}\right](1-R_1)(1-e^{-\alpha d}) \tag{2.20}$$

While designing the detector, the cavity layers are chosen such that all the light is absorbed in the active layer $\alpha_{ext} \ll \alpha$. The expression in the square braces is called the enhancement, as it is the multiplier to the quantum efficiency of a conventional photodiode. Enhancement can be rewritten as:

$$enhancement = \frac{(1+R_2 e^{-\alpha d})}{1-2\sqrt{R_1 R_2}e^{-\alpha d}\cos(2\beta L+\varphi_1+\varphi_2)+R_1 R_2 e^{-\alpha d}} \tag{2.21}$$

From this expression, it is seen that η is enhanced periodically at the resonant wavelengths of the cavity, $2\beta L + \varphi_1 + \varphi_2 = 2\pi m$ (m = 1,2,3...). This term introduces the wavelength selectivity of the RCE effect.

From the expression for the quantum efficiency (η), it is seen that three parameters R_1, R_2, and αd effect η. R_2, the reflectivity of the bottom mirror, should be designed as high as possible. Otherwise, due to the transmission from the bottom mirror, the performance of the detector decreases dramatically. The other parameter is the reflectivity of the top mirror. When the quantum efficiency is maximized with respect to R_1, the following condition is obtained:

$$R_1 = R_2 e^{-2\alpha d} \tag{2.22}$$

If top mirror reflectivity is low, the light is lost from the cavity in the form of reflection. On the other hand, if it is high, incoming light cannot be coupled into the cavity.

2.2.2 Standing Wave Effect

While deriving the formula of the quantum efficiency, the spatial distribution of the optical field inside the cavity was neglected. This spatial distribution arises from the standing wave formed by the two counter propagating waves. This is referred as standing wave effect (SWE). The SWE is conveniently included in the formalism of η as an effective absorption constant, i.e., α_{eff} = SWE × α. The effective absorption constant α_{eff} is the normalized integral of α and the field intensity across the absorption region.

$$\alpha_{eff} = \frac{\frac{1}{d}\int_0^d \alpha(z)\left|E(z,\lambda)\right|^2 dz}{\frac{2}{\lambda}\int_0^{\lambda/2}\left|E(z,\lambda)\right|^2 dz} \tag{2.23}$$

When detectors with thick active layers, which span several periods of the standing wave, are considered, SWE can be neglected. For very thin active layers, which are necessary for strained layer absorbers, SWE must be considered.

2.3 Optical Design

Our detector designs, like other RCE photodetectors, vertical cavity surface emitting lasers (VCSEL), and distributed feedback lasers (DFB) are quite complicated. The devices contain micro cavities, which are formed with low loss mirrors. The reflection amplitude and phase from these mirrors are not trivial. Also the optical properties of the materials used in the cavities are wavelength dependent and this makes rather difficult to predict the optical field in such multilayer devices, therefore a good simulation method is needed for the analysis before the growth. Transfer matrix method (TMM) is commonly used, which provides a simple and accurate technique to calculate electric and magnetic field distributions inside the cavity.

2.3.1 Transfer Matrix Method

When a layer is modeled from an optical point of view, it is seen that it consists of two elements; an interface where an abrupt refractive index difference occurs, and a slab where refractive index is constant and extends for a certain width. Refractive index is defined as the square root of the dielectric constant of the medium; $n = \sqrt{\varepsilon}$. Usually the dielectric constant is complex and the imaginary part is due to the absorption in the medium, and refractive index can be simplified as $n = n_{real} - in_{imag}$, where both n_{real} and n_{imag} are real and positive numbers.

The electric field at any point can be modeled as superposition of forward and backward going waves as shown in Figure 2.8. When the Maxwell equations are solved, the continuity of the electric and magnetic field at the interface is obtained.

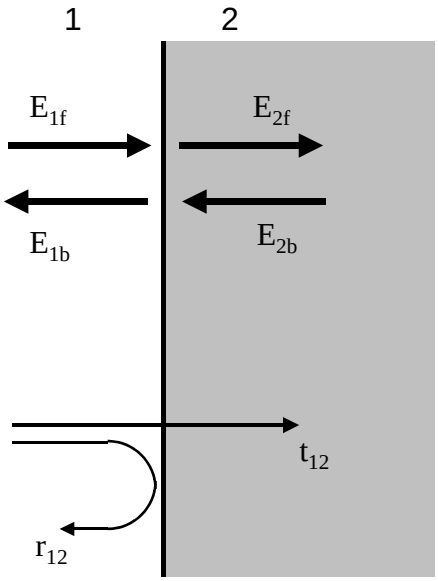

$$\frac{1}{t_{12}}\begin{bmatrix} 1 & r_{12} \\ r_{12} & 1 \end{bmatrix}$$

$$t_{12} = \frac{2n_1}{n_1 + n_2}$$

$$r_{12} = \frac{n_1 - n_2}{n_1 + n_2}$$

Figure 2.8: Electric field amplitudes at the interface.

The relation between the forward and backward field amplitudes before and after the interface has the relation:

$$\begin{bmatrix} E_{1f} \\ E_{1b} \end{bmatrix} = \frac{1}{t_{12}}\begin{bmatrix} 1 & r_{12} \\ r_{12} & 1 \end{bmatrix} \cdot \begin{bmatrix} E_{2f} \\ E_{2b} \end{bmatrix} \tag{2.24}$$

where, $t_{12}=(2*n_1)/(n_1+n_2)$, $r_{12}=(n_1-n_2)/(n_1+n_2)$. n_1 and n_2 are the refractive indexes of the consecutive layers.

The electric field inside the layer can be found by propagation of plane wave:

$$\begin{bmatrix} E_{2f}(x) \\ E_{2b}(x) \end{bmatrix} = \begin{bmatrix} e^{-ik_2 x} & 0 \\ 0 & e^{ik_2 x} \end{bmatrix} \cdot \begin{bmatrix} E_{2f} \\ E_{2b} \end{bmatrix} \tag{2.25}$$

where, $k=(2\pi n)/\lambda$ is the wave vector in the medium. When x is chosen as the width of the layer (as shown in Figure 2.9), the electric field just at the left of the next interface can be found.

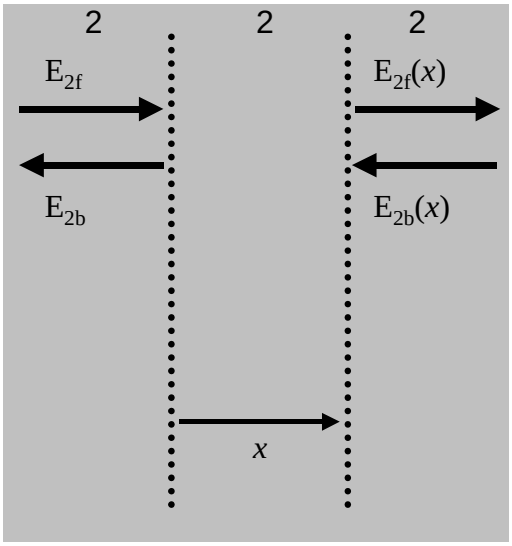

$$k_2 = \frac{2\pi}{\lambda} n_2$$

$$\begin{bmatrix} e^{-ik_2 x} & 0 \\ 0 & e^{ik_2 x} \end{bmatrix}$$

Figure 2.9: The propagation of wave inside the same medium.

If the two matrices given by eq. 2.24 and eq. 2.25 are combined, a transfer matrix of the layer for the field amplitudes is given as:

$$T_m = \frac{1}{t_m} \begin{bmatrix} e^{i\delta_m} & r_m e^{i\delta_m} \\ r_m e^{-i\delta_m} & e^{-i\delta_m} \end{bmatrix} \tag{2.26}$$

where, $t_m=(2\ n_m)/(n_m+ n_{m+1})$, $r_m=(n_m-n_{m+1})/(n_m+ n_{m+1})$, and $\delta_m=k_m d_m$. Cascading these matrices for N layers, total matrix of the multiplayer structure can be constructed as:

$$T_{total} = T_0 T_1 T_2 \cdots T_{N-1} T_N \tag{2.27}$$

The relation between the electric field at electric field at the left and at the right sides of our system as depicted in Figure 2.10 is given by:

$$\begin{bmatrix} E_{if} \\ E_{ib} \end{bmatrix} = T_{total} \cdot \begin{bmatrix} E_{ff} \\ E_{fb} \end{bmatrix} \tag{2.28}$$

For a detector structure shown in Figure 2.10, E_{fb} is zero; hence E_{ff} and E_{ib} can be solved in terms of E_{if} easily.

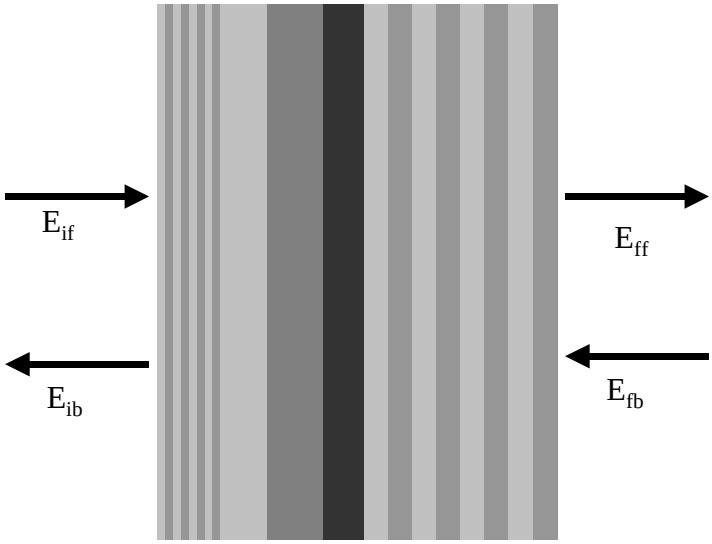

Figure 2.10: Electric field values before and after the structure.

When a measurement like reflectivity is made, the reflected power is measured not the electric field. The same is valid for the transmission and absorption. The power associated with a plane wave can be found by:

$$\vec{S} = \frac{1}{\mu}\vec{E} \times \vec{B} \tag{2.29}$$

and using the relation between the electric and magnetic field amplitudes for a plane wave:

$$\vec{B} = \frac{1}{\omega}\vec{k} \times \vec{E} \tag{2.30}$$

The power is proportional to the square of the electric field amplitude and the refractive index of the medium. Then the reflectivity and transmittivity of the structure are given by:

$$R = \frac{\left|E_{ib}\right|^2}{\left|E_{if}\right|^2} \tag{2.31}$$

$$T = \frac{\left|E_{ff}\right|^2 n_{final}}{\left|E_{if}\right|^2 n_{init}} \tag{2.32}$$

Calculating the total power entering and leaving that layer, we can find absorption of this layer [23-25]. Also the same calculations apply for the oblique incidence with small modifications. Sample TMM calculations are shown at the appendix.

2.3.2 Distributed Bragg Reflectors

As shown in the previous sections, the aim is to place the active layer inside a cavity formed by two mirrors. Good designs require bottom mirrors with high reflectivities. Although metals are good reflectors, their reflectivities (R≈95 can be achieved) are wavelength dependant, and semiconductor layers cannot be grown on them.

Distributed Bragg reflectors (DBR's) are widely used in optoelectronic applications such as detectors and semiconductor lasers. A DBR is a periodic stack with two alternating quarter-wave thick materials with different optical properties. Each pair consists of two layers with refractive indices n_1 and n_2, and layer thickness of $\lambda_c/4n_1$ and $\lambda_c/4n_2$ respectively. λ_c is the central wavelength of the mirror where reflectivity is maximum.

When the light is reflected from different interfaces of one pair, it is observed that all the light is at the same phase resulting in a constructive interference hence increasing the reflectivity. Applying TMM for a DBR at center wavelength λ_c, results in a simple expression for the reflectivity as:

$$R_{\max} = \left(\frac{1 - \left(\frac{n_2}{n_1} \right)^{2N}}{1 + \left(\frac{n_2}{n_1} \right)^{2N}} \right)^2 \tag{2.33}$$

where N is the number of mirror pairs in the stack. For large values of N reflectance approaches unity, and for a fixed N reflectivity increases as n_2/n_1

increases. Also width of the highly reflective wavelength span increases as the index difference between the layers increases.

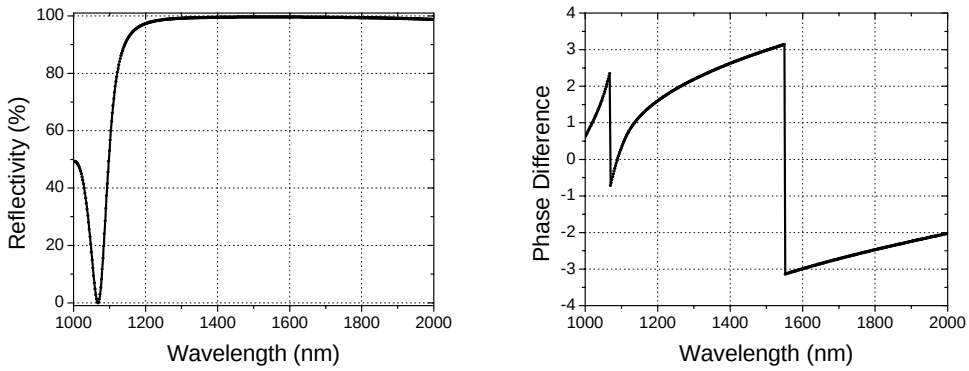

Figure 2.11: Reflection spectrum and phase difference of InP/Air DBR with 3 pairs.

The phase difference between the incidence and reflected wave is a function of the wavelength. The reflectivity and the phase difference between the incidence and reflected waves for InP/Air and InP/InAlGaAs DBRs are shown in Figure 2.11 and Figure 2.12.

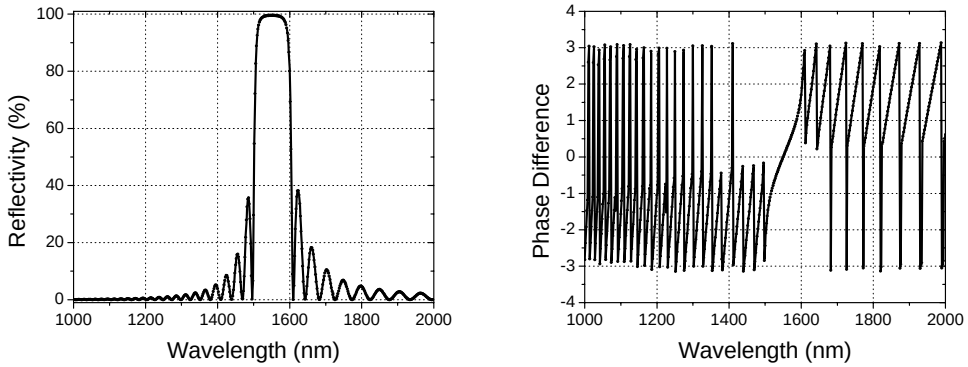

Figure 2.12: Reflection spectrum and phase difference of InP/InAlGaAs DBR with 40 pairs.

In the InP/Air DBR, the index difference is 2.167. Three pairs are enough to get 99.6% reflectivity with this structure. If the high reflectivity band of this structure is observed, it is seen that its FWHM is higher than 1000 nm. While InP/InAlGaAs DBR has index difference of only 0.293. This DBR needs 40 pairs to achieve 99.5% reflectivity. Also due to lower index contrast, FWHM is less than 100 nm.

With a small change in the design of the DBRs, the nature of these mirrors can be changed. If the width of one of the layers (with a refractive index of n_1) increased from $\lambda_c/4n_1$ to $\lambda_c/2n_1$, the structure becomes transparent around λ_c, while still reflecting other wavelengths. In this case, the multiplayer stack functions as a notch filter. Such filters have been demonstrated at various wavelengths on both silicon and GaAs based devices [26-28]. Figure 2.13 shows the transmission spectra of notch filter, which consists of Si and SiO_2 layers operating around 1550 nm.

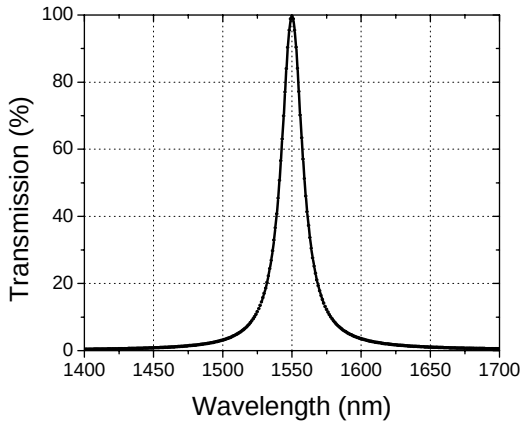

Figure 2.13: Transmission spectrum of Si/SiO_2 notch filter centered to 1550 nm.

Chapter 3

Fabrication and Characterization

This chapter presents the fabrication and characterization process that was completed in Advanced Research Laboratories at Bilkent University. Section 3.1 explains the basic fabrication steps, while section 3.2 presents the measurement setups.

3.1 Basic Fabrication Steps

This section explains the details of fabrication steps completed in a Class-100 clean room environment. With the application of three or four of them, usually one fabrication step of the photodetectors are completed.

3.1.1 Sample Cleaving

The wafers that are used for the fabrication of photodetectors in this thesis are usually quite expensive and hard to grow. That's why we prefer working with small samples cleaved from the wafer. Sample sizes are around 7×7 mm^2, and the mask is 6×6 mm^2. We use a diamond tipped scriber-pen to define a line at the back of the substrate. After defining the shape of the sample, the wafer can be easily cleaved. The thicknesses of the wafer are usually 350 μm for 3-inch wafers, and 600 μm for 4-inch wafers.

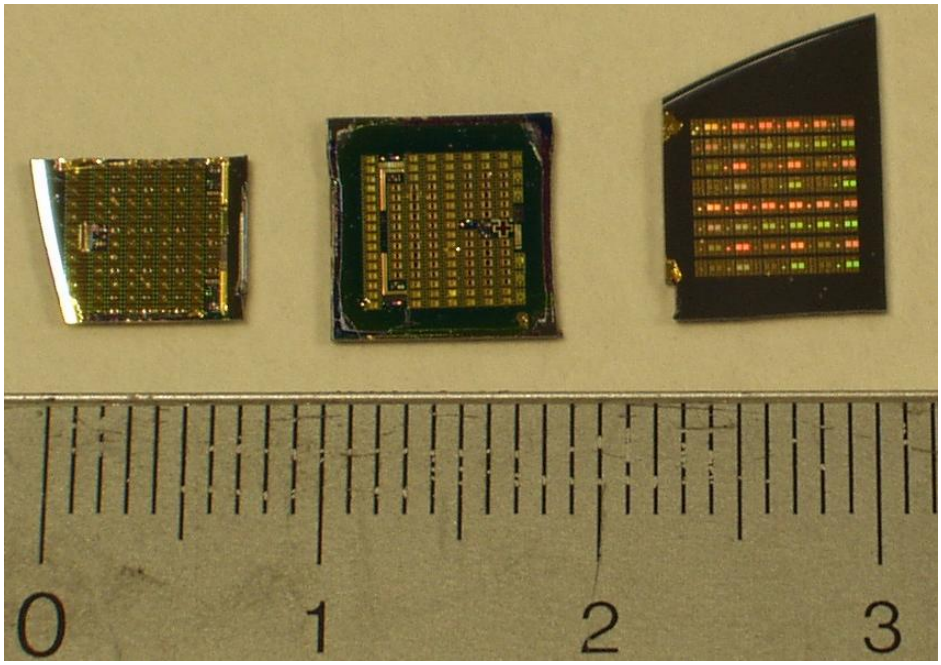

Figure 3.1: Photographs of some samples with fabricated photodetectors on them.

3.1.2 Sample Cleaning

The samples are cleaned at every step. The residues from the previous step must be cleaned. Three different solvents are used for the cleaning, namely trichloroethane, aceton, and isopropanol alcohol. Samples are dipped into them in order. The details of the cleaning are as follows:

- Samples are immersed into the boiling trichloroethane for 2 minutes.
- Then the samples are kept in acetone at room temperature for 5 minutes. Acetone dissolves organic molecules, and the photoresist.
- Next samples are kept in boiling isopropanol alcohol for 2 minutes. This alcohol cleans the residues from the previous step.
- Samples are rinsed in the de-ionized (DI) water flow and dried with nitrogen gun.

- Although the sample is dried with nitrogen flow, there remains a very thin layer of water at the surface. To evaporate this water, samples are baked at 120 ^{o}C on the hat plate for 2 minutes. This bake is called dehydration bake.

3.1.3 Photolithography

Before the fabrication, the mask is prepared which contains the features to be transformed onto the samples. The CAD program named Wavemaker is used for the preparation of the digital file. The features for each step are placed on 6×6 mm^2 area. These features are the photodetectors, test diodes that does not contain interconnect metallization, ohmic test patterns, development marks that are used to check the quality of the photolithography and development, and the alignment marks that are used to align the mask with respect to the sample at each step. One mask usually contains 25 dies, where each die has the patterns for one lithography step. The size of the masks is 4×4 inch^2 so that all the dies can be used with the mask aligner. Figure 3.2 shows photographs of our masks. Figure 3.3 has some plots from the digital mask file.

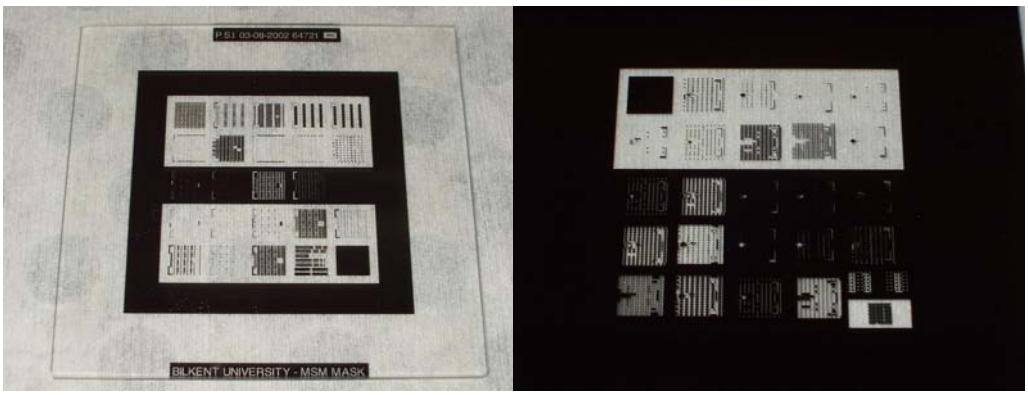

Figure 3.2: Photographs of the masks.

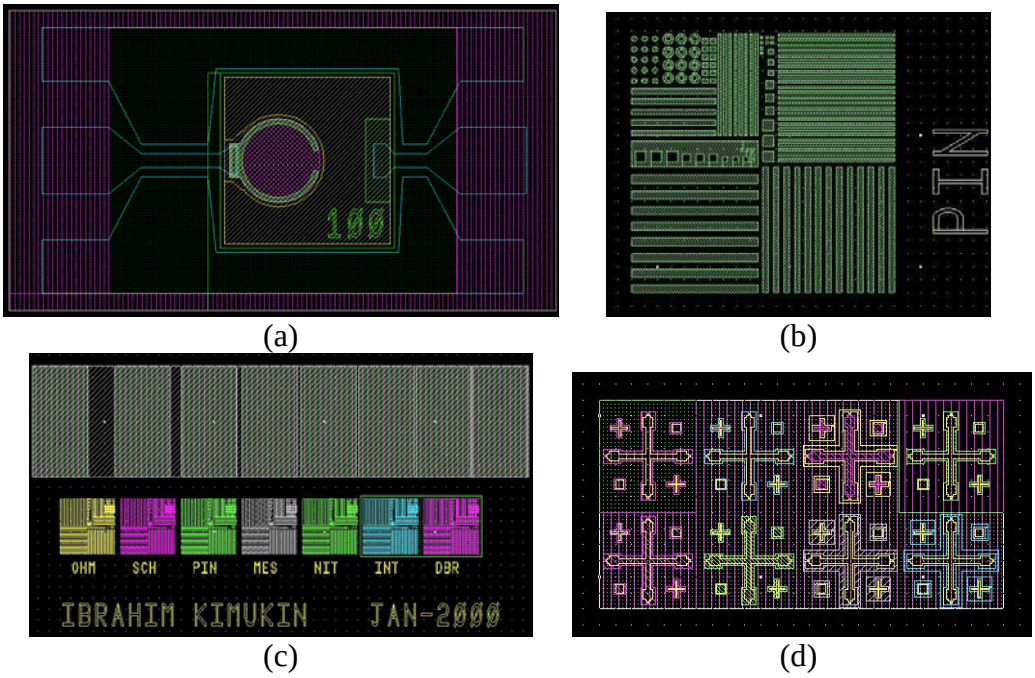

(a) (b)

(c) (d)

Figure 3.3: Plots from the mask file (a) a photodiode with 100 μm diameter active area, (b) development marks used in the p+ ohmic step, (c) p+ ohmic transmission lines and the development marks, and (d) alignment marks.

Photolithography starts with covering the surface of the sample with a chemical, which contains polymer that is sensitive to ultraviolet radiation. This chemical is called photoresist. The AZ-5214E type photoresist produced by Clarient is used. To achieve a uniform thickness, the sample is spinned at 5000 rpm for 40 seconds. The thickness of the photoresist obtained after this spin is around 1.35 μm. The thickness can be changed by changing the spin rate [29]. This photoresist is sensitive to UV radiation in the 310 – 420 nm spectral range. The Karl-Suss MJB3 mask aligner is used for the alignment of the samples and exposure. The aligner has a mercury lamp that has a high power emission around 365 nm. Before the exposure, the sample is baked on a hot plate at

110^{o}C for 55 seconds. This bake is called the soft-bake. At this point, the process can be varied to get both positive and negative resist.

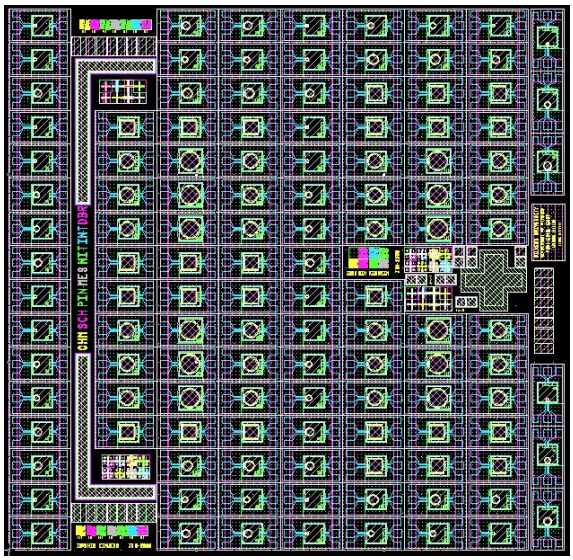

Figure 3.4: Plot of the mask containing large area photodetectors. All the fabrication steps are shown aligned to each other. The mask contains around 115 photodetectors.

- **Normal Photolithography:** After the soft-bake, the sample is exposed with the mask with a total energy of 150 mJ/cm^2**.** The photoresist at the exposed area becomes soluble in the developer.
- **Image-reversal Photolithography:** After the pre-bake, the sample is exposed with the mask with a total energy of 50 mJ/cm^2. Then the sample is baked at 110 ^{o}C for 2 minutes. The exposed photoresist becomes inert after this step. Then the whole sample area is exposed without a mask with a total energy of 150 mJ/cm^2. Then the unexposed area in the first exposure becomes soluble in the developer. The explanation of this process is also shown in Figure 3.5.

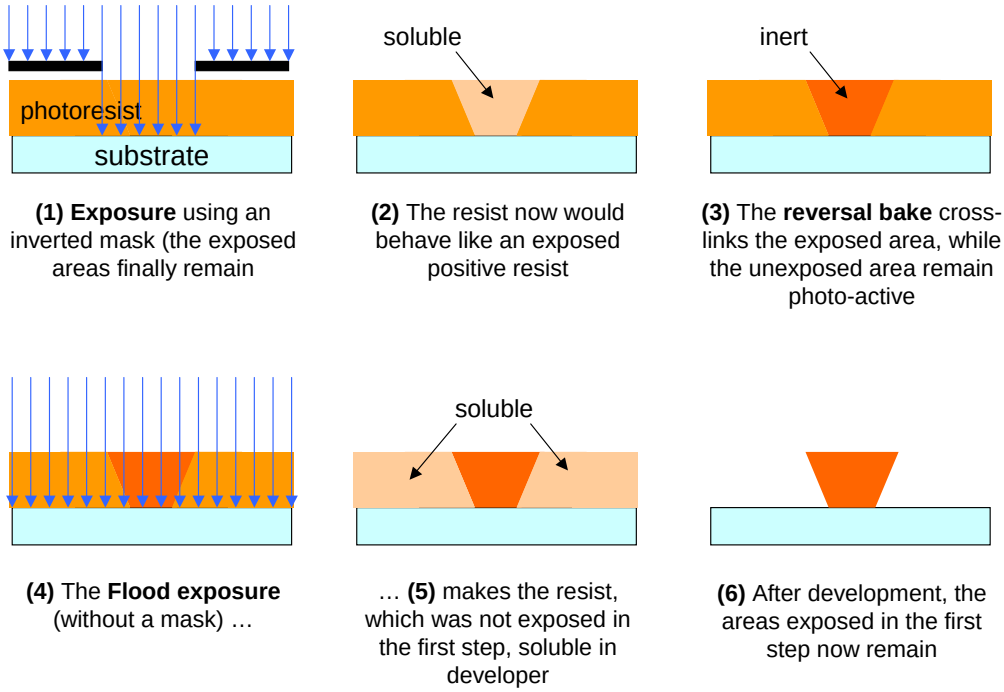

Figure 3.5: Image-reversal photolithography (after reference [30]).

3.1.4 Development

For the development of the exposed samples, AZ400K developer is used with a 1:4 (Developer:H_2O) volume ratio. As the soluble regions of the resist are etched by the developer, change in the color can be observed with naked eye. When this color change stops, the sample is rinsed under DI water. After drying the sample, the alignment and the development is checked. The resolution patterns must be sharp, and for a good photolithography about 1 μm resolution should be observable. The resolution of the image-reversal photolithography is less than the normal photolithography. The AZ400K developer contains metal ions and is based on potassium hydroxide. This developer affects the semiconductor layers containing Aluminum.

3.1.5 Etch

The etch process is used for transforming the defined patterns onto the underlying metal, semiconductor or dielectric layers, so that the desired layer is reached for the subsequent process. Etching is also used for cleaning and thinning photoresist, removing damaged material, polishing, and removing surface oxides. Etching is done in two different methods, either by using chemical reactants present in aqueous solution (wet etch) or with the help of ions and molecules present in a plasma (dry etch).

- **Wet Etch:** Chemical reactions that occur at the surface of the material with the reactants present in the solution. For the semiconductors, the etching is basically done by oxidation or reduction of the surface and then removal of the soluble reaction product. The etch rate may be limited by the transport of the reactants and the products. This type of etches are diffusion-controlled etches. This type of etch is usually anisotropic and agitation of the solution changes the etch rate and profile. The etch is called reaction-limited etch, if the reaction has a rate-limiting step. These type of etches can be isotropic, and the rate is insensitive to agitation [31]. We bake the resist at 120 ^{o}C for 1 min, to refrain the photoresist from the tension that occurs during the development. This bake enhances the adhesion to the substrate at the contours of the photoresist, which decreases the under-etch for deep etches. Figure 3.6 (a) shows a wet etch profile of GaAs where the under-etch is more than expected. Some of the etch recipes that are used in our lab are listed in Table 3.1.

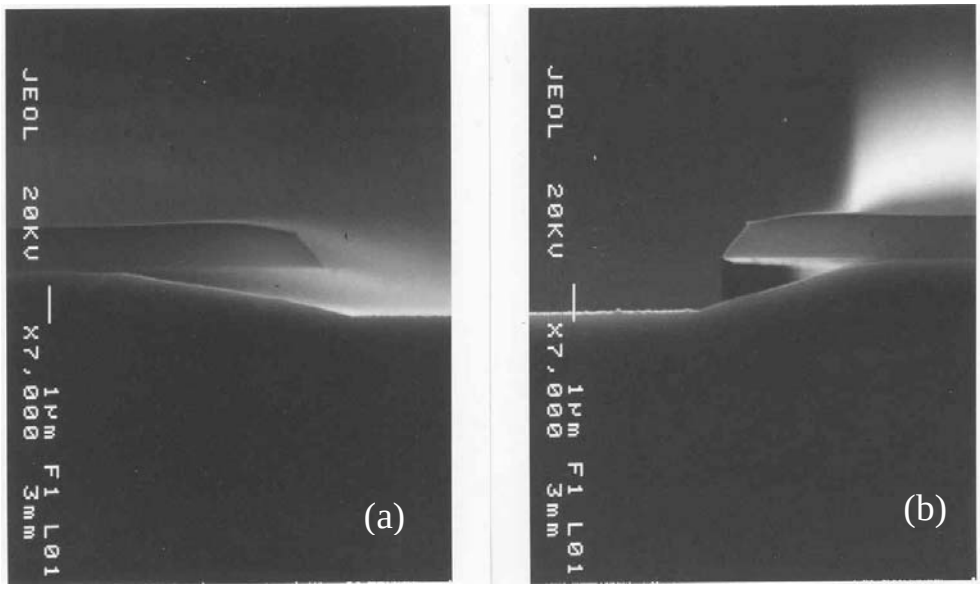

Figure 3.6: SEM picture wet etch profiles.

Table 3.1: Etch rates of some recipes used in our processes.

Etchant		Etched Layer	Etch Rate (nm/sec)
$H_3PO_4 : H_2O_2 : H_2O$	(1:3:40)	InGaAs, InAlAs	4.5, 5.0
$HCl : H_3PO_4$	(1:3)	InP	12.5
$H_3PO_4 : H_2O_2 : H_2O$	(1:1:5)	InAs	12.5
Citric acid : H_2O_2	(1:1)	InSb	~ 0.4 - 0.5
$HF : H_2O_2 : H_2O$	(2:1:100)	GaSb	30.0
$NH_3 : H_2O_2 : H_2O$	(2:1:75)	GaAs, $Al_{0.2}Ga_{0.8}As$	5.0, 8.1

- **Dry Etch:** Dry etching techniques use plasma-driven chemical reactions or energetic ion beams. Some of dry etching techniques are plasma etching, reactive ion etching (RIE), reactive ion-beam etching (RIBE), sputter etching, and ion milling. Plasma etch occurs either by the bombardment of the surface with highly energetic ions where the etching is made mechanically, or by the chemical reactions between the

gases and the surface. In the later, volatile products are generated which are pumped out of the reaction chamber. Changing the gas pressure and ion energy can control degree of isotropy. Usually higher gas pressure results isotropic etch. Ultra high vacuum (UHV) RIE machine is used for dry etching. With appropriate gases, dielectrics, semiconductors, resist, even metals can be etched with this system [32-34]. Currently CCl_2F_2, SF_6, CHF_3, O_2, CF_4, and H_2 gases are available in our system. Some of the recipes are listed in Table 3.2.

Table 3.2: Etch rates of some recipes used in RIE etch.

Plasma Condition	Etch Results
RF Power : 51 W Pressure : 7 μBar O_2 : 20 sccm Self Bias : 350 V	Hardened Photoresist : 70 nm/min
RF Power : 51 W Pressure : 4 μBar CCl_2F_2 : 20 sccm Self Bias : 360 V	GaAs : 100 nm/min $Al_{0.3}Ga_{0.7}As$: 30 nm/min Photoresist : 10 nm/min
RF Power : 99 W Pressure : 10 μBar CCl_2F_2 : 20 sccm Self Bias : 490 V	InP : 50 nm/min InGaAs : 55 nm/min Photoresist : 12 nm/min
RF Power : 200 W Pressure : 15 μBar CH_4 : 10 sccm H_2 : 20 sccm O_2 : 0 sccm Self Bias : 570 V	InP : 36 nm/min (CH_4 currently not available) (Damages the photoresist) (Polymer deposition on the mask)

RF Power : 69 W Pressure : 20 μBar CHF_3 : 60 sccm O_2 : 5 sccm Self Bias : 350 V	Si : 12.5 nm/min Si_3N_4 : 70 nm/min SiO_2 : 1.1 nm/min Photoresist : 32 nm/min
RF Power : 99 W Pressure : 8 μBar CCl_2F_2 : 20 sccm Self Bias : 490 V	GaAs : 300 nm/min InAs : 60 nm/min Si_3N_4 : 40 nm/min SiO_2 : 25 nm/min ITO : 20 nm/min Photoresist : 45 nm/min GaN : 31 nm/min $Al_{0.38}Ga_{0.62}N$: 13 nm/min Hardened Photoresist : 22 nm/min
RF Power : 150 W Pressure : 10 μBar CHF_3 : 60 sccm O_2 : 5 sccm Self Bias : 550 V	SiO_2 : 17 nm/min Photoresist : 42 nm/min

While most of the III-V semiconductors materials can be etched using a wet etch techniques, GaN and related materials cannot be etched easily in this way. We use only RIE with CCl_2F_2 gas to etch GaN and other wide band-gap materials [35].

3.1.6 Metallization

Metals are deposited onto the sample for ohmic, Schottky, or interconnect metallization. Metals and dielectric coatings are deposited inside ultra high vacuum LE590 box coater, using thermal evaporation or radio frequency (RF) sputtering technique. In both methods, the pressure of the process chamber is lowered to 5×10^{-6} mBar. The deposition rate and the total thickness of the film are monitored during the process.

We usually pattern the metal layer using a technique called lift-off. Metal is deposited on patterned photoresist. Deposited metals stick to the surface of the sample at the openings. The metals on the photoresist are lifted-off later. For the thick metallization, image-reversal photolithography is preferred. The negative slope of the photoresist enables a discontinuity between the metal at the openings and the photoresist.

- **Thermal Evaporation:** Pallets or powder of metals are placed inside tungsten boats. When we pass current though the boat, metals start evaporating. By changing the current, we can control the evaporation rate of the metals. Hot metal atoms from the boats spread inside the vacuum and stick to the sample and cold surfaces. Gold (Au), Germanium (Ge), Nickel (Ni), Titanium (Ti), and Aluminum (Al) are deposited with this method in our lab.
- **RF sputtering:** Samples are placed on top of the target. The target contains the material to be deposited on the sample. With the help of argon and the RF power, argon atoms break bonds of the target. The ions from the target move up to the sample. If enough ions accumulate at the surface, they join and nucleate. After forming islands on the surface, they combine and for a layer of film. Indium-tin-oxide (ITO) is deposited with this method.

3.1.7 Lift-off

After the metallization, the metals deposited on top of the photoresist must be removed from the sample. Samples are soaked into the acetone. As acetone dissolves the photoresist, the metals on them also are lifted-off from the sample.

This process is quite easy if these metals have no connection with the ones at the openings. Otherwise ultrasound must be used to agitate the sample

and break the contact between these two metal regions. It is easier to use the lift-off technique if thermal evaporation is used compared to the sputter technique, as thermal evaporation does not produce a good step coverage on the sidewalls of the photoresist.

3.1.8 Thermal Annealing

Rapid thermal annealing (RTA) is used to heat the samples very rapidly to very high temperatures (as high as 1400 ^{o}C) to form ohmic contacts. Flash lamps are embedded into the RTA device as the heat source. Samples are heated under the radiation of these flash lamps for a certain time. The environment contains forming gas, which is a mixture of hydrogen (5%) and nitrogen (95%).

The contact between the metal and the semiconductor surface has a barrier called Schottky barrier, hence this is a rectifying contact. The electrons can flow from one region to the other either by thermionic emission over the barrier or by tunneling though it. Most ohmic contacts are achieved by decreasing the width of the potential barrier.

As the doping of the semiconductor increases, the width of the barrier decreases, and the tunneling can begin without a resistance, i.e., resulting in a good ohmic contact. The high doping can be achieved by alloying the metal with the semiconductor, which is possible with the thermal treatment. The alloy temperature and time has an important effect on the resistance of the contact. Increasing the temperature to the optimum value decreases the contact resistance down to the minimum achievable value. Further increase of the temperature usually increases both the resistance and the morphology of the contact [37]. The optimum annealing conditions of each ohmic contact must be determined for every different wafer.

The resistance of the contact is determined using a series of ohmic contacts with varying distance between them. The crossection of such contacts are shown in Figure 3.7 (a). The total resistance can be modeled as two contact resistances (R_c) and the sheet resistance (R_s) of the semiconductor as shown on Figure 3.7 (b). By plotting the resistance versus distance between contacts (L) graph, we determine the contact resistance (half of the y-intercept) and the sheet resistance of the semiconductor layer (slope of the line times the width of the ohmic contact). Figure 3.7 (c) shows the series of ohmic contacts used for this measurement.

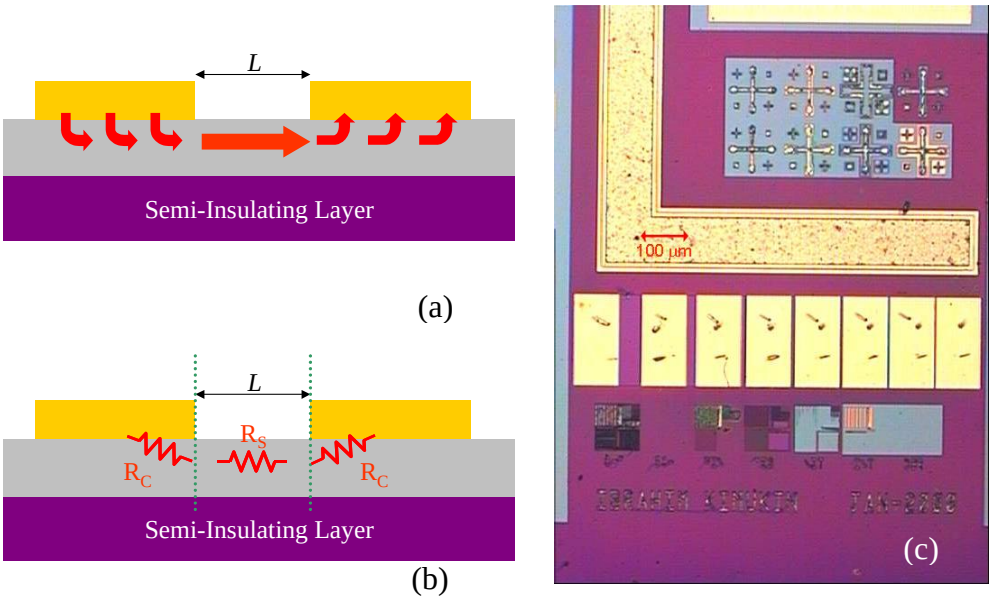

Figure 3.7: (a) The current flow between the contacts. (b) The schematics of the model used for the ohmic contact characterization. (c) The p+ ohmic transmission line (center) is used for ohmic quality measurements. Also the alignment marks (up) and the development marks (bottom) can be seen.

3.1.9 Dielectric Deposition

Dielectric layers are used for metal-insulator-metal capacitors, CMOS devices, and photodetectors. The dielectric coatings in our process are used for surface

passivation, anti-reflection coating, and top DBRs. These dielectric layers can be deposited by RF sputtering or plasma enhanced chemical vapor deposition (PECVD) technique in our lab. The repeatability of the first method isn't very good. The optical and mechanical properties of the films can fluctuate very much through the sample. Instead, PECVD method is preferred, which has high uniformity and repeatability. Also the optical and mechanical properties of the films can be controlled with the flow rates of the gases and process temperature.

Our device is a computer controlled Plasmalab 8510C reactor. It has a chamber that contains a parallel plate for the application of RF (at 13.56 MHz), heater, temperature controller, gas flow controllers, and pressure controller. With the application of RF signal, we produce chemically active species inside the plasma and reaction takes place at the hot surface of the sample. The gases used in our lab are silane (2% SiH_4:98% N_2), ammonia (NH_3), and nitrious oxide (N_2O). The deposited films are amorphous, and byproducts are pumped out of the process chamber. The overall reactions for the deposition of SiO_2 and Si_3N_4 films are as follows:

$$3SiH_4 + 4NH_3 \rightarrow Si_3N_4 + 12H_2$$

and

$$SiH_4 + 2N_2O \rightarrow SiO_2 + 2H_2 + 2N_2$$

It is better to use lower RF powers (10–50W) and moderate temperatures (200–350 ^oC) to get a good quality films. The refractive index of the films can be controlled by changing the flow rates of the gases [36]. In our process, we try to get high index nitride layers for the antireflection coatings. Increasing the silane flow rate can increase the refractive index. But increasing it to high values results in films that can't be etched easily with diluted HF. We usually prefer 20 W RF power during the growth. Our process conditions and

the properties of the resulting films are given in Table 3.3. Figure 3.8 contains pictures of the devices used during these process steps.

Figure 3.8: Pictures of equipments: (a) mask aligner, (b) surface profilometer, (c) thermal evaporator and RF sputter, (d) PECVD, (e) RIE, (f) RTA

Table 3.3: Growth conditions and properties of dielectric films.

Plasma Condition	Film Properties		
	RF Power =10 W	RF Power =20 W	RF Power =50 W
Silane : 180 sccm NH_3 : 45 sccm Pressure: 1000 mTorr Temp : 250 ^oC	Rate: 10.7nm/min Index: 1.72	Rate: 12.8nm/min Index: 1.76	Rate: 17.0nm/min Index: 1.77
Silane : 180 sccm N_2O : 710 sccm Pressure: 1000 mTorr Temp : 250 ^oC	Rate: 32.0nm/min Index: 1.46	Rate: 40.6nm/min Index: 1.46	Rate: 43.2nm/min Index: 1.47

3.2 Measurement Setups

This section briefly explains the measurement setups and techniques in our measurement lab in Class-10000 environment.

3.2.1 Reflection and Transmission Measurements

The reflectivity of the grown wafer is the first data that can be used to understand the layer properties of our detectors. Also the reflection and transmission results of dielectric films give us the optical properties of these films. A fiber optic based setup is used for these measurements. The light source and the detector change for different wavelength range.

For the measurements at the ultraviolet (UV) and visible range, deuterium-tungsten light source is used, and the light is coupled to reflection probe. The reflected or the transmitted light is again coupled to another fiber, which delivers the light to the spectrometer located in one of the PCI bus of the computer.

For the infrared region we use two different setups. First consists of a halogen lamp whose light passes through a monochromator and coupled to the fiber arrangement explained before. Then the optical power is measured with optical powermeter. The other setup consists of the halogen light source and the fiber probes. But the reflected of transmitted light is measure with optical spectrum analyzer. The setup used for the infrared measurement is shown in Figure 3.9.

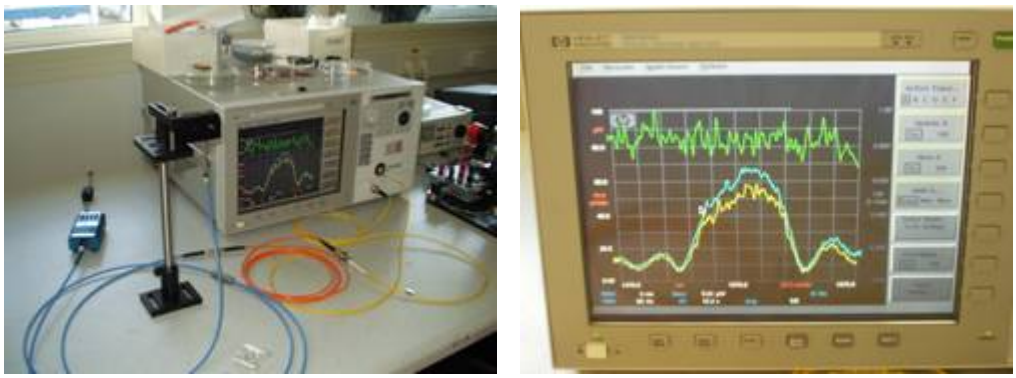

(a) (b)

Figure 3.9: (a) The reflectivity measurement setup. The light source (blue) the fiber probe and the optical spectrum analyzer can be seen. (b) The reflectivity of the InGaAs based photodetector wafer.

3.2.2 Current Voltage Measurements

We make the on-wafer measurements with the help of probe station (shown in Figure 3.10(a)), where various probes including DC contact probes, fiber holder, and microwave connection probes can be placed. These probes are used for the electrical and optical characterization.

For the current-voltage characterization we use computer controlled HP4142B DC Source monitor unit. Using the computer, either current or voltage inputs are provided, and the corresponding characteristics are measured with the same module. This setup is also used for the characterization of the

ohmic contacts with the help of accurate voltage measurement ports. Figure 3.11 shows the unit and the computer control.

(a) (b)

Figure 3.10: (a) The probe station. With the help of objectives, we can make contact to the pads of the photodetectors. (b) The sample on the probe station, where two DC probes touch the pads, while the active are is illuminated with the fiber.

(a) (b)

Figure 3.11: HP4142B and the computer control.

3.2.3 Quantum Efficiency Measurements

The responsivity characterization can be made with two measurement setups. First setup consists of a wide spectrum light source and a monochromator for wavelength selection. The light is chopped and coupled to a multimode fiber.

Using the probe station and the fiber probe, the active area of the detector is illuminated. The detectors are biased with a DC power supply, and the photocurrent is measured with a lock-in amplifier. The data is collected using a computer equipped with a GPIB control. This setup has a wide spectrum range, starting from UV to mid mid-IR wavelengths. The schematic diagram and the pictures of this are shown in Figure 3.12.

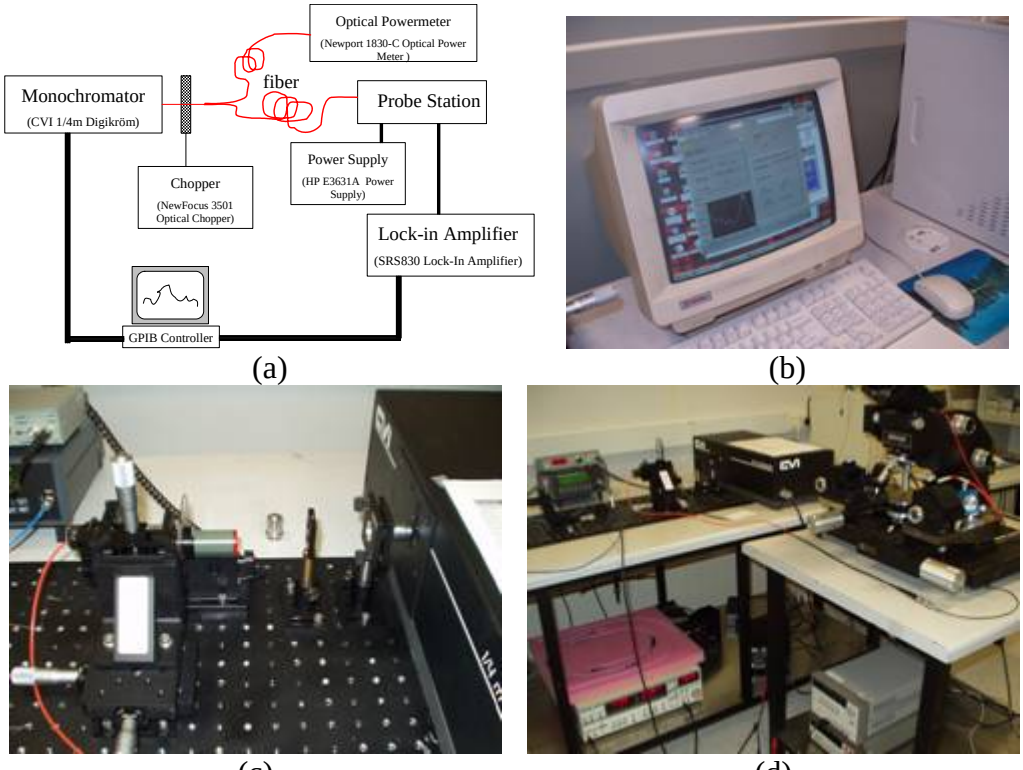

Figure 3.12: Quantum efficiency measurement setup with the monochromator.

The second setup consists of a tunable laser as the light source. It covers the spectrum from 1500 to 1620 nm. The maximum optical power output is a function of wavelength. The output wavelength and power is controlled with a computer and the laser is coupled to a single mode fiber. The light is delivered to the active area of detectors as described before. The

detectors are biased with DC power, supply and the photocurrent is measured directly with multimeter. The data is then collected by a computer. The schematic diagram and the picture of the setup are shown in Figure 3.13.

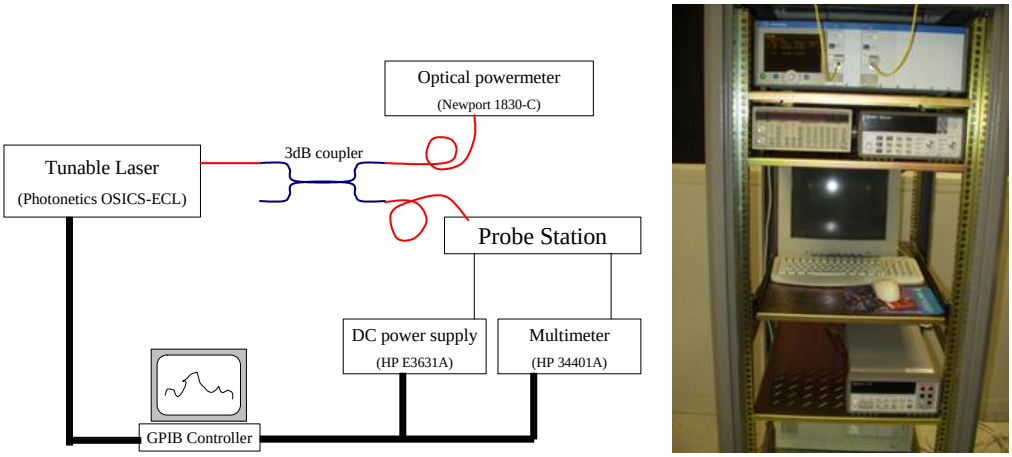

Figure 3.13: Quantum efficiency measurement setup with the tunable laser.

3.2.4 High Speed Measurements

High speed measurements are done with a laser that can generate optical pulses with femtosecond widths. The pulses are generated using erbium doped fiber laser, and coupled to single mode fiber. The detectors are biased with DC power supply using bias-tee, and the temporal response of the detectors is measured with a 50 GHz sampling scope. Although the scope is 50 GHz, the bias-tee can operate up to 40 GHz, and this setup is limited with this frequency. The response of the detector is stored as a function of bias voltage and the light intensity. The schematics of the setup are shown in Figure 3.12 along with its pictures.

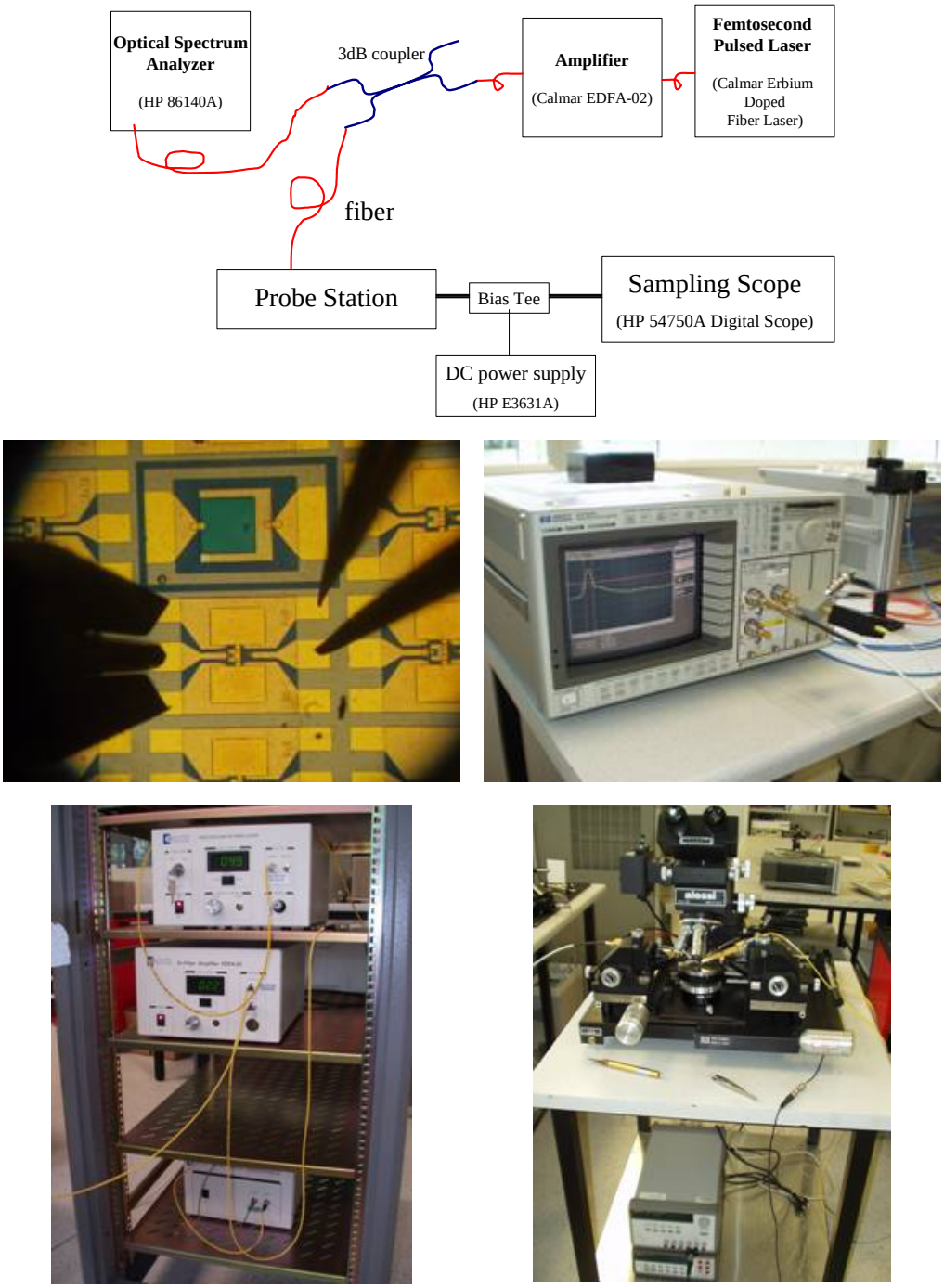

Figure 3.14: High Speed measurement setup.

Chapter 4

InGaAs p-i-n Photodetector

This chapter presents our effort to fabricate high speed and high efficiency RCE photodetector operating around 1550 nm wavelength. Photodetectors based on InP lattice matched materials are most commonly used in the optical fiber communication systems, eye-safe rangefinders, free space communication systems, and laser pulse shaping. These applications require fast photodetectors that can operate in tens of gigahertz range. Mixed materials lattice matched to InP makes possible to make heterojunctions where this is impossible for Silicon and Germanium. These materials are formed by mixing Group-III and Group-V elements to form ternary and quaternary compounds. Figure 4.1 shows the lattice parameters and energy gap values of common III-V compound semiconductors.

The photodetector performance is measured by the bandwidth-efficiency product (BWE) and is limited for conventional vertically illuminated photodetectors (VPDs) due to the bandwidth-efficiency trade-off [10]. This tradeoff is due to the fact that the quantum efficiency and bandwidth of a conventional VPD have inverse dependencies on the photoabsorption layer thickness.

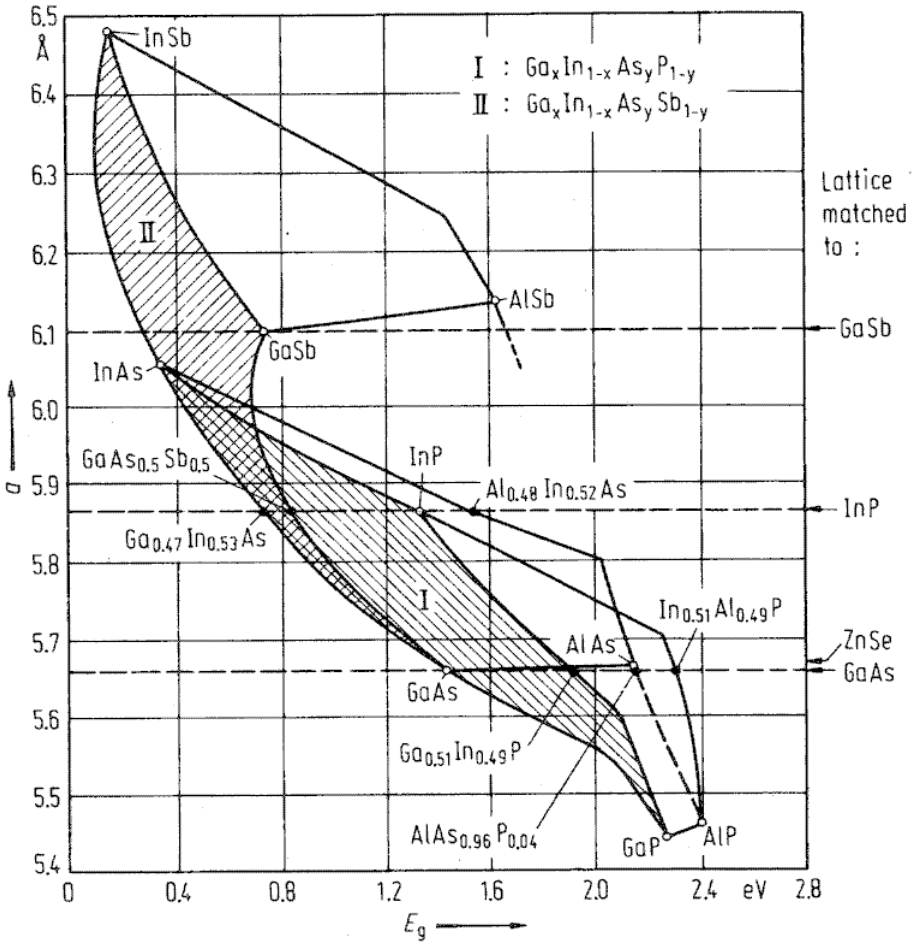

Figure 4.1: Lattice parameter vs. energy gap of III-V compounds used with InP and GaAs based devices (after reference [61]).

One detection scheme to overcome this limitation is edge-coupled photodiodes. This scheme has been used to achieve very high speed metal-semiconductor-metal (MSM) [38] or p-i-n waveguide photodiodes with bandwidths above 500 GHz [39], distributed MSM photodetectors with 78 GHz bandwidth [40], avalanche photodiodes with 120 GHz gain-bandwidth product [41], traveling-wave photodetectors with high output current [42] or 115 GHz bandwidth [43], and 110 GHz 50%-efficiency mushroom-mesa

waveguide photodetectors [44]. The disadvantages of edge-illuminated detectors are complex fabrication and integration along with difficult light coupling.

The ease of fabrication, integration, and optical coupling makes the resonant cavity enhanced (RCE) PDs attractive for high-performance photodetection [10, 45-27, 20]. The incident photons, which are at the resonance wavelength of the detector cavity, are recycled, so that the quantum efficiency (QE) is enhanced at this wavelength. Therefore, by using RCE-PD with a thin active layer, high efficiency values can be achieved without lowering the detector bandwidth [48, 49]. Using the RCE structure, InGaAs based MSM PDs with 77% QE and 10 GHz bandwidth at 1.3 μm wavelength [50], Schotttky PDs with 55% QE and 22.5 GHz bandwidth [51], p-i-n [52], and avalanche PDs with ~70% QE and 24 GHz at unity gain [54] have been reported by other researchers. A comparison of this work and the other research results are given in Table 4.1.

4.1 Design

$In_{0.53}Ga_{0.47}As$ was chosen to be the active layer of the detector. This ternary compound is lattice matched to InP, and it can be easily grown by molecular beam epitaxy (MBE) or metal-organic chemical vapor deposition (MOCVD) techniques. $In_{0.53}Ga_{0.47}As$ is direct band-gap material with the band-gap energy of 0.75 eV, which corresponds to 1650 nm cut-off wavelength. InP based photodetectors are superior to Ge photodetectors as, $In_{0.53}Ga_{0.47}As$ is capable of detecting optical signals transmitted at non-dispersion wavelength (1300 nm) and minimum-loss wavelength (1550 nm) of the silica based fibers used in the

Table 4.1: Comparison of this work with the previous research

RCE	Illum.	Type	λ (μm)	Q.E.	Bandw. (GHz)	BEP (GHz)	I_{max} (mA)	Comment	Ref.
√	vert.	APD	1.58	0.66	24.0	16.0			[54]
√	vert.	Pin & Sch	1.57	0.20				Bottom illuminated, metal top mirror	[52]
√	vert.	Schottky	1.55	0.55	22.5	14.6		ITO Schottky with substrate removel	[51]
×	vert.	Schottky	1.55	0.46	25.0	11.5		ITO Schottky	[53]
√	vert.	pin	0.98		120			Very small area, power coupling is a problem	[39]
√	vert.	pin	1.47	0.86				Waferfused to AlAs/GaAs mirror	[55]
√	vert.	MSM	1.30	0.77	10.0	7.7			[50]
×	vert.	MSM	1.55	0.13	38.0	4.9		Integrated to receiver with optimized vaveguide	[56]
×	vert.	MSM	1.30	0.25	16.0	4.0			[57]
×	vert.	MSM	1.30	0.92	4.0	3.7		Bottom illuminated	[58]
×	WG	APD	1.55	0.23	27.0	6.2			[41]
×	WG	pin	1.55	0.50	110	55		Waveguide specially shaped for high respons.	[44]
×	WG	MSM	1.55	0.33	18.0	6.0	12	Velocity matched design	[59]
×	WG	pin	1.55	0.38	35	13.1	45.3	Velocity matched design	[60]
√	vert.	pin	1.57	0.66	28	18.5	6.2	This work	

modern communication systems. $In_{0.53}Ga_{0.47}As$ based detector structures have a few disadvantages when compared to GaAs based structures:

1. $In_{0.53}Ga_{0.47}As$ has an absorption coefficient 64% lower than GaAs as shown on Table 4.2 [62]. Also the drift velocities of electron and holes are around 80% lower than the carriers in GaAs as shown on Figure 4.2. When both of these properties are combined, the bandwidth efficiency product of $In_{0.53}Ga_{0.47}As$ based photodetectors is 50% lower than GaAs based detectors.

Table 4.2: Optical properties of various III-V semiconductor compounds.

	Energy band-gap E_g (eV)	Cut-off wavelength λ_g (nm)	Refractive Index	Absorption Coefficient
			n (λ=1550nm)	α (λ=1550nm) (cm^{-1})
InP	1.35	920	3.167	0
$In_{0.52}Al_{0.48}As$	1.45	855	3.200	0
$In_{0.53}Ga_{0.47}As$	0.75	1650	3.589	0.81×10^4
$In_{0.53}Al_{0.13}Ga_{0.34}As$	0.91	1360	3.428	0
$In_{0.66}Ga_{0.34}As_{0.73}P_{0.27}$	0.86	1440	3.425	< 40
			n (λ=820nm)	α (λ=820nm) (cm^{-1})
GaAs	1.42	870	3.670	1.27×10^4
AlAs	2.18	570	2.990	0
$Al_{0.20}Ga_{0.80}As$	1.61	770	3.460	0

2. Band discontinuities are the results of heterojunctions. Although this is a desired property for lasers, modulators, and quantum well devices where the charges are confined inside the structure, we try to avoid this in the high speed photodetectors. These discontinuities result in charge trapping, and degrade the performance in terms of speed and

responsivity. The semiconductors used in the $In_{0.53}Ga_{0.47}As$ based photodetectors have larger energy band discontinuities compared to GaAs based ones. Graded regions are usually formed to get a smoother variation. Table 4.3 lists properties of a few junctions commonly used in the InP and GaAs based photodetectors.

Table 4.3: Band discontinuities of some heterostructure systems.

	Energy band-gap difference ΔE_g (eV)	Conduction band discontinuity ΔE_c (eV)	Valance band discontinuity ΔE_v (eV)
InP / $In_{0.53}Ga_{0.47}As$	0.60	0.25	0.35
$In_{0.52}Al_{0.48}As$ / $In_{0.53}Ga_{0.47}As$	0.71	0.52	0.19
$In_{0.52}Al_{0.48}As$ / InP	0.11	0.35	-0.24

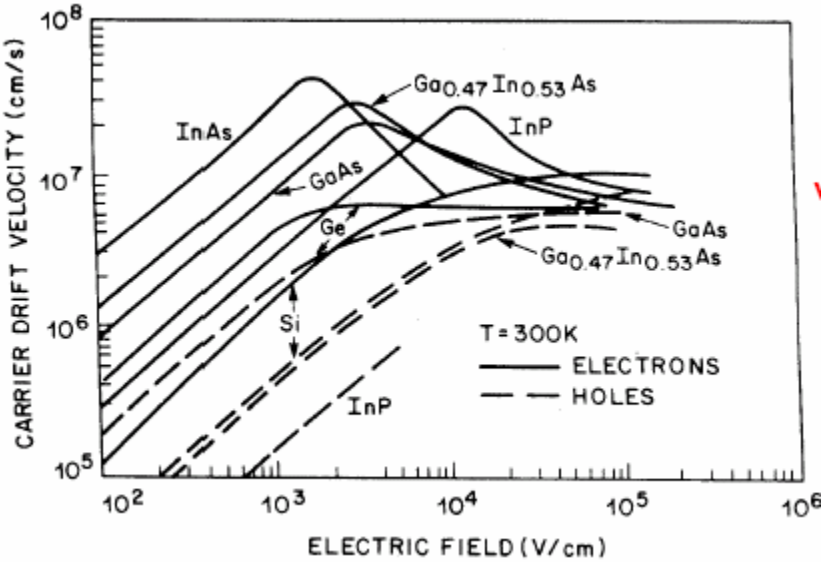

Figure 4.2: Charge drift velocity as a function of electric filed strength for various semiconductors (after reference [61]).

Alloy	Matching Condition *y*
$Al_xGa_{1-x}P_ySb_{1-y}$	$(0.227+0.040x)/(0.645+0.040x)$
$Al_xGa_{1-x}As_ySb_{1-y}$	$(0.227+0.040x)/(0.443+0.033x)$
$Al_xGa_yIn_{1-x-y}As$	$(0.189-0.398x)/0.405$
$Al_xIn_{1-x}P_yAs_{1-y}$	$(0.189-0.398x)/(0.189+0.020x)$
$Al_xIn_{1-x}P_ySb_{1-y}$	$(0.610-0.343x)/(0.610+0.075x)$
$Al_xIn_{1-x}As_ySb_{1-y}$	$(0.610-0.343x)/(0.421+0.055x)$
$AlP_xAs_ySb_{1-x-y}$	$(0.267-0.685x)/0.058$
$Ga_xIn_{1-x}P_yAs_{1-y}$	$(0.189-0.405x)/(0.189+0.013x)$
$Ga_xIn_{1-x}P_ySb_{1-y}$	$(0.610-0.383x)/(0.610+0.035x)$
$Ga_xIn_{1-x}As_ySb_{1-y}$	$(0.610-0.383x)/(0.421+0.022x)$
$GaP_xAs_ySb_{1-x-y}$	$(0.227-0.645x)/0.443$

(a)

Alloy	Energy gap (eV)
Ternaries	
$Al_xIn_{1-x}As$	$E_g(\Gamma) = 0.37+1.91x+0.74x^2$
	$E_g(X) = 1.82+0.4x$
$Ga_xIn_{1-x}As$	$E_g(\Gamma) = 0.324+0.7x+0.4x^2$
$GaAs_{1-x}Sb_x$	$E_g(\Gamma) = 1.43-1.9x+1.2x^2$
$InAs_{1-x}P_x$	$E_g(\Gamma) = 0.356+0.675x+0.32x^2$
Quaternaries	
$Ga_xIn_{1-x}As_yP_{1-y}$	$E_g(\Gamma) = 1.35+0.668x-1.068y+0.758x^2+0.078y^2-0.069xy-0.322x^2y+0.03xy^2$
	$E_g(\Gamma) = 1.35-0.775y+0.149y^2$ (x=0.47y : lattice matched to InP)
$Al_xGa_yIn_{1-x-y}As$	$E_g(\Gamma) = 0.36+2.093x+0.629y+0.577x^2+0.436y^2+1.013xy-2.0xy(1-x-y)$
	$E_g(\Gamma) = 0.764+0.495z+0.203z^2$ ($0.98x+y=0.47$, x=0.48z : lattice matched to InP)

(b)

Figure 4.3: (a) Lattice match conditions of quaternary compounds to InP (after reference [68]). (b) Energy gap of III-V compounds (after reference [69]).

3. Another big issue is the growth of highly reflective DBR for the RCE photodetectors operating in the infrared region. The semiconductor

compounds lattice matched to InP have lower index contrast compared to materials lattice matched to GaAs. AlAs / $Al_{0.20}Ga_{0.80}As$ pair is a perfect candidate for DBR centered around 800 nm. The index contrast of $\Delta n = 0.47$ makes high reflective mirrors with fewer pairs of semiconductor layers. Unfortunately the index contrast available with the InP matched systems is substantially smaller than between GaAs and AlAs. The maximum available contrast $\Delta n = 0.40$ is between InP and $In_{0.53}Ga_{0.47}As$, and this DBR is not suitable for operation at 1550 nm due to absorption in the $In_{0.53}Ga_{0.47}As$ layer. Thus some other ternary or quaternary compounds with cut-off wavelength smaller than 1550 nm are used in high quality DBRs. These compounds are obtained with adding Al or P to $In_{0.53}Ga_{0.47}As$. Figure 4.3(a) gives a summary of quaternary compounds lattice matched to InP. The low index materials are $AlAs_{0.56}Sb_{0.44}$, InP, or $In_{0.52}Al_{0.48}As$ with refractive indexes 3.07, 3.17, and 3.20 respectively. While the high index materials can be AlGaAsSb, AlGaInAs, or InGaAsP with the cut-off wavelength around 1450 nm where the refractive indexes of these materials hover around 3.45 [63-66]. The available index contrast Δn is around 0.25, which is half of the index contrast available in GaAs based materials. Due to this lower contrast, the number of DBR pairs is around 36 to achieve reflectivity higher than 99% [67].

The design started with the bottom DBR. Although higher index contrast can be achieved with antimony (Sb) containing compounds, they are not easy to grow. Other common alternatives are InAlAs/InAlGaAs and InP/InGaAsP systems, which are commonly grown with MBE or MOCVD reactors. We

decided on the Al based DBR due to an MBE system available during the design.

$In_{0.53}Al_{0.13}Ga_{0.34}As$ was chosen as the high reflective index material, and it corresponds to $\chi = 0.27$ for the definition given by ref [70]. The optical properties of this semiconductor compound can be obtained by the equation Eq.(4.1):

$$n(\lambda)^2 = A + \frac{B\lambda^2}{\lambda^2 - C^2} \tag{4.1}$$

where A=9.255, B=1.599, and C=928.3nm. The refractive index of this compound is 3.428 at 1550 nm while $In_{0.52}Al_{0.48}As$ has refractive index of 3.200 as shown on Figure 4.4. The index contrast is 0.23 for this DBR pair.

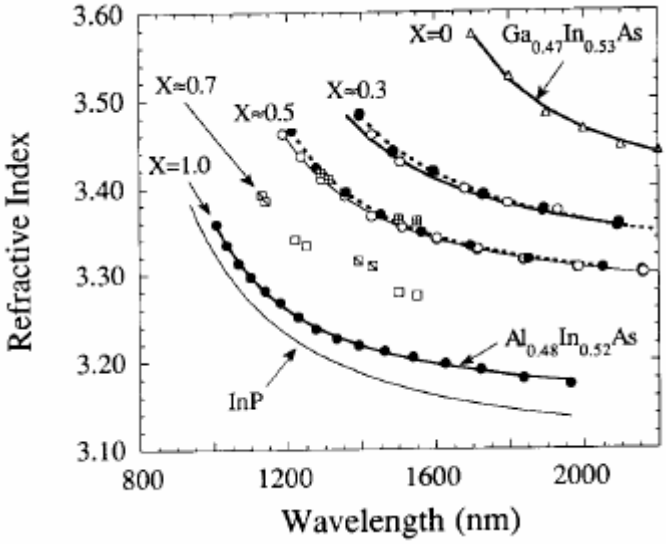

Figure 4.4: Refractive index of $(In_{0.52}Al_{0.48}As)\chi(In_{0.53}Ga_{0.47}As)1\text{-}\chi$ as a function of wavelength for different values of χ (after reference [70]).

The energy bandgap of $In_{0.53}Al_{0.13}Ga_{0.34}As$ was calculated according to the formula given in Figure 4.3 (b). It was found that the energy bandgap was 0.912 eV, which corresponds to the cutoff wavelength of 1360 nm that is well below 1550 nm. The TMM simulations show that the bottom DBR should have

a maximum reflectivity of nearly 90% at 1548 nm. Calculated spectral reflectivity of the DBR is shown in Figure 4.5.

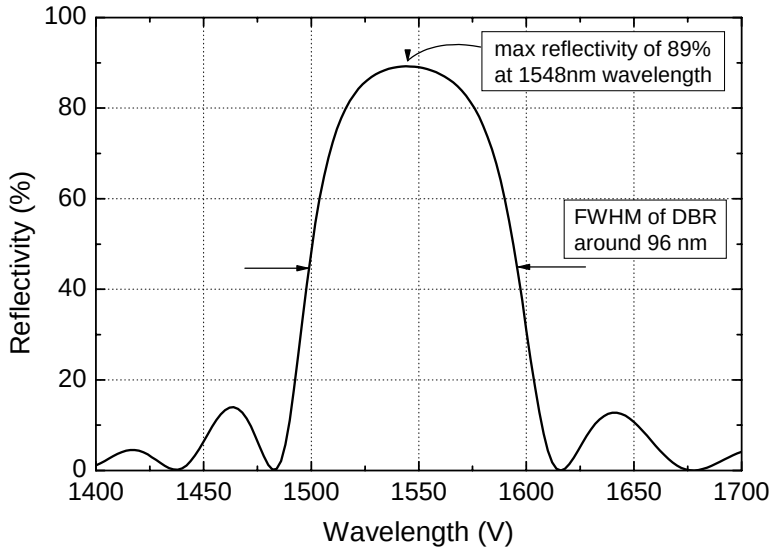

Figure 4.5: Spectral reflectivity of the bottom DBR calculated using TMM.

On top of the bottom DBR, the cavity started with a spacer $In_{0.52}Al_{0.48}As$ layer with the thickness chosen to fix the resonance around 1550 nm. This layer was also used as the insulating layer that the interconnect metals are deposited. On top of this layer, a silicon doped $In_{0.52}Al_{0.48}As$ layer was used to make the n+ ohmic contacts. Before the active lightly n type doped $In_{0.53}Ga_{0.47}As$ layer a thin $In_{0.52}Al_{0.48}As$ layer and a digital grading was used. The digital grading was formed by varying the thickness of $In_{0.52}Al_{0.48}As$ and $In_{0.53}Ga_{0.47}As$ layers, which effectively changes the energy bandgap of the layers seen by the charges. On top of the active layer a similar grading was placed for the holes. P+ ohmic contact layer was also transparent $In_{0.52}Al_{0.48}As$ layer doped with beryllium. The thickness of this layer was chosen to be thick

enough to tune one resonance of the cavity by post-process etching. A thin highly doped $In_{0.53}Ga_{0.47}As$ layer was used at the top of the structure, which makes a lower resistive p-type ohmic contact possible. This layer also prevents the oxidation of the wafer before the fabrication. The total thickness of the photodetector exceeds 7.1 micron. The thickness and the doping information of the layers are given in Table 4.4. A similar structure without the bottom DBR was also designed to see the effect of the RCE effect directly by comparing the quantum efficiency measurements.

Table 4.4: Epitaxial structure of the InGaAs based pin detector wafer.

	Material	Thickness (nm)	Doping Type	Dopant	Concant. (cm^{-3})
	$In_{0.53}Ga_{0.47}As$	30	p+	Be	1×10^{19}
	Digital Grading	30	p+	Be	1×10^{19}
	$In_{0.52}Al_{0.48}As$	210	p+	Be	1×10^{19}
	$In_{0.52}Al_{0.48}As$	50	n-	Si	1×10^{16}
	Digital Grading	30	n-	Si	1×10^{16}
	$In_{0.53}Ga_{0.47}As$	300	n-	Si	1×10^{16}
	Digital Grading	30	n-	Si	1×10^{16}
	$In_{0.52}Al_{0.48}As$	60	n-	Si	1×10^{16}
	$In_{0.52}Al_{0.48}As$	300	n+	Si	3×10^{18}
	$In_{0.52}Al_{0.48}As$	240	S.I.	none	none
25 pairs {	$In_{0.52}Al_{0.48}As$	121	S.I.	none	none
25 pairs {	$In_{0.53}Al_{0.13}Ga_{0.34}As$	112	S.I.	none	none
	600 μm thick Semi-Insulating InP Substrate				

The TMM based calculations showed that the quantum efficiency of the photodetector was 74% while the reflectivity and transmittivity of the photodetector were 7% and 14% respectively. Some of the power was also lost in the bottom DBR. As a result of the low reflectivity of the bottom DBR, we saw that the enhancement of quantum efficiency with the deposition of the top

DBR would be small. This is mainly due to more power loss from the bottom of the detector. According to these results, we decided not to deposit silicon nitride - silicon dioxide top mirror layer, instead use the reflectivity of the top semiconductor layer. The calculations used during the design of the detector are shown on appendix.

We also made calculations to predict the frequency response of the photodetector. The high speed measurements were usually done under 7 to 9 volts of reverse bias. For our structure, this corresponded to electric field strength of 20×10^3 V/cm. The drift velocities of the charged carriers were around 8×10^6 cm/s and 5×10^6 cm/s for electrons and holes respectively. Corresponding transit times were 7.6 ps and 4.9 ps. For a 14×14 μm^2 area photodetector, the calculated 3-dB bandwidth was 45 GHz for 50 Ω load resistance [71]. As the sum of load and serial resistance increased, the 3-dB bandwidth of the photodetector decreased. A sample calculation of the frequency response of these photodetectors is given on appendix.

With the above electrical and optical properties, the calculated bandwidth efficiency product was 33 GHz. The enhancement was more than 3 times compared to a similar single-pass structure. The calculations show that the quantum efficiency of the single pass structure was 22% at 1550 nm.

4.2 Fabrication

The structure was grown by MBE method by Quantum Epitaxial Designs, Inc. in USA. Initial visual inspection showed that the wafer of the resonant structure was not as shinny as the single-pass structure wafer. This was most probably due to the growth of the quaternary compound used in the DBR. Our

measurements of the completed detectors fabricated from both wafers showed no difference in terms of electrical characteristics.

Before the fabrication, we measured the spectral reflectivity of the wafer which gives useful information about the thicknesses of the DBR and cavity layers. Our reflectivity measurement and TMM calculations showed that the bottom DBR had grown %3 to %4 thicker than our design. This shifted the center wavelength of the DBR to around 1600 nm. The measurement and calculation results for a region on the wafer where the shift was %4 are shown on Figure 4.6. The lower and upper edge of highly reflective spectrum was 1550 nm and 1690 nm.

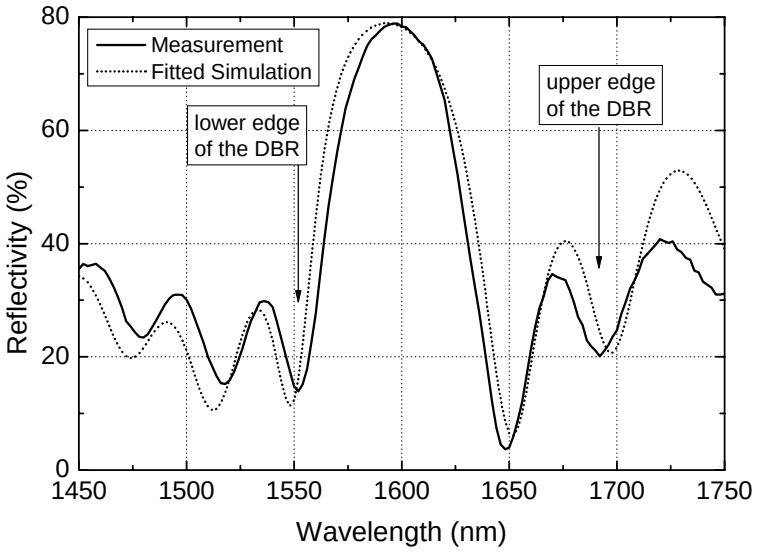

Figure 4.6: The measurement (solid line) and calculation (dotted line) results for a region on the wafer where the shift was %4.

The fabrication was made with two different masks. The first mask had 5 lithography steps having larger area photodiodes. These photodiodes were

used during quantum efficiency measurements, as it was easier to couple all the light from cleaved single mode (~9 μm core diameter) and multi mode (~85 μm core diameter) fibers to the active area of the photodetectors. The area of the photodetectors was ranging from 30 μm to 200 μm in diameter. The second mask had 7 lithography steps having smaller area photodiodes. These photodiodes were used during high speed measurements, not to limit the responses of the photodetectors with the capacitance of the detector. Although we used cleaved fiber during the high speed measurements, lensed fiber can be used to couple the entire laser power into the photodetector. The area of the photodetectors was ranging from 5×5 μm^2 to 20×20 μm^2, as well as a few 150×150 μm^2. These photodetectors also had airbridge for lower parasitic capacitance and integrated biasing capacitors for providing constant bias during the excitation of the detector with high powered pulses.

4.2.1 Large Area Photodetector Fabrication

1. **n+ Ohmic Contact Formation:** After the normal photolithography, the layers were etched down to the middle of the n+ doped InAlAs layer. Wet (chemical) etch was used during this step. A phosphoric acid based solution was used for etching both InGaAs and InAlAs layers. The composition was chosen as H_3PO_4:H_2O_2:H_2O (1:3:40) which had the etch rate of 4.5 nm/sec for both of the materials. Increasing the ratio of H_2O_2 to H_3PO_4, the etch rate of Al containing layers increased which caused high under etch. A list of available etchants used with the InP base materials are given in Table 4.5. After the wet etch, germanium, gold, and nickel were evaporated onto the sample. The layers and the thicknesses were Ge/Au/Ge/Au + Ni/Au (10.8/10.2/6.3/23.6 + 10/200

nm). Then the sample was soaked into the acetone. The photoresist dissolves in the acetone and the metal on top of it was lifted-off. After the cleaning, the sample was treated at 400 ^{o}C for 60 sec. Figure 4.7 shows the n+ ohmic contacts before and after the thermal process.

Table 4.5: Etch rates of some common etchants. The rates are indicated as nm/sec. Stop means no etch.

Etchant	InGaAs	InAlAs	InP	InGaAsP
H_3PO_4 : H_2O_2 : H_2O (1:3:40)	4.5	5.0	stop	stop
Citric acid : H_2O_2 (1:2)	2.1	stop	stop	
H_2SO_4 : H_2O_2 : H_2O (1:8:80)	8.3		stop	
H_2SO_4 : H_2O_2 : H_2O (1:1:10)			stop	1.7
HCl : H_2O (3:1)	stop	10.8	etches	
HCl : H_2O (2:1)	stop		133	
HCl : H_2O (1:1)	stop		11.6	
HCl : H_3PO_4 (1:1)	stop		41.7	
HCl : H_3PO_4 (1:3)	stop		12.5	

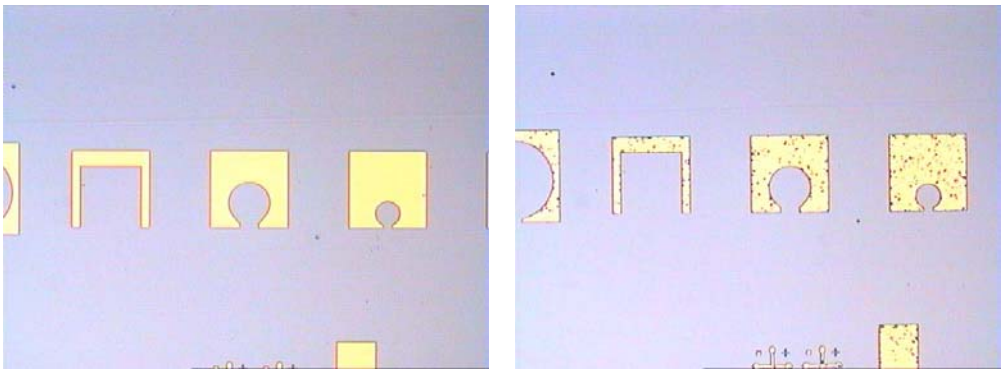

(a) (b)

Figure 4.7: The n+ ohmic contacts before (a) and after (b) the RTA.

2. **p+ Ohmic Contact Formation:** After the cleaning, the photoresist was exposed by using normal photolithography. Then Ti/Au (15/200 nm) metals were evaporated onto the sample. The metals were lifted of using the same method used in the previous step. After cleaning the

sample, it was thermally processed at 450 ^{o}C for 30 sec. We could not increase the RTP temperature, because the quality of the n+ ohmic contacts started to degrade. Figure 4.8 shows the p+ metal contacts before deposition of the metal and after the thermal process.

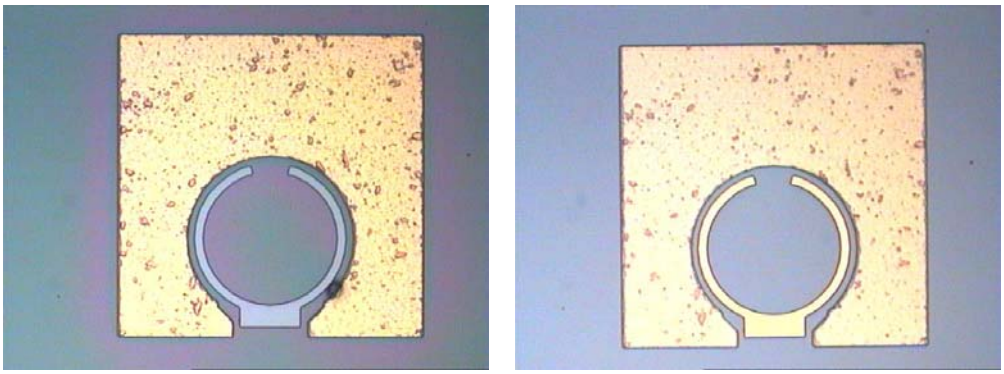

(a) (b)

Figure 4.8: The p+ ohmic contacts before the metal deposition (a) and after the RTA.

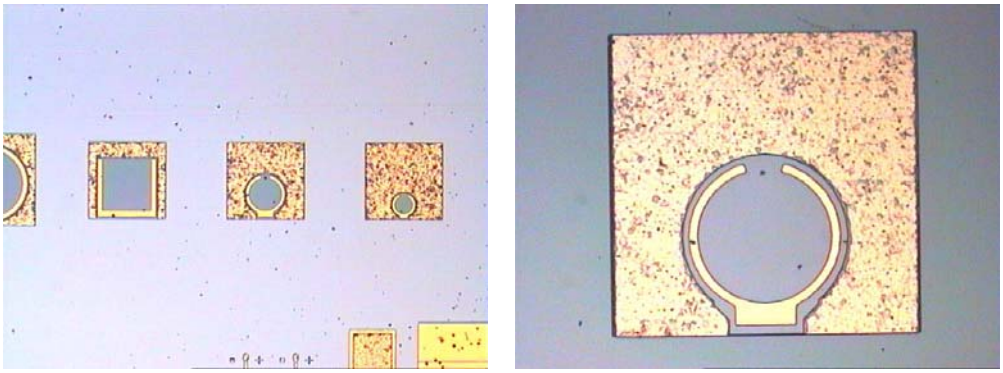

(a) (b)

Figure 4.9: (a) The color change on the surface is due to the variation of the etch depth (b) the mesa contour can be seen as a thin black line below the p contact.

3. **Mesa Isolation:** With a normal lithography, the active area and the ohmic contacts were covered with photoresist. Then the layers were etched down to the undoped InAlAs layer for RCE wafer and down to

InP substrate for the single-pass wafer. The etch was done in several steps and the etch depth was monitored with DEKTAK surface profilometer. The sidewalls of the mesa had an inclination, which was good for further metallization.

4. **Surface Passivation:** After the cleaning, the surface was covered with Si_3N_4 layer. This layer was deposited at 250 ^oC with the PECVD technique. Normal lithography was used to define the area to be etched away. Dilute hydrofluoric acid solution was used to etch the dielectric layer. The sidewalls and the active area of the photodetector was kept covered, while the area that the interconnect metal will be deposited was cleaned. Figure 4.10 shows the photograph of the devices before and after the HF etches.

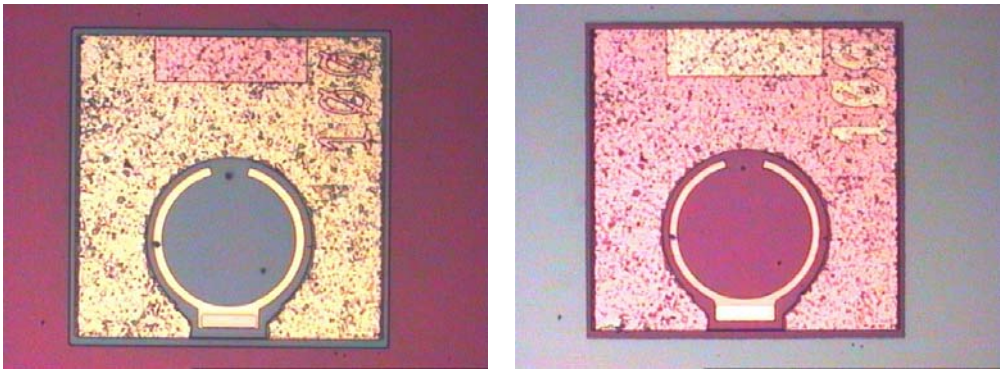

(a) (b)

Figure 4.10: (a) The surface was covered with silicon nitride, and the photograph shows the surface after photolithography, (b) the surface of the sample after the HF etch and the cleaning. Some area on top of the contacts was open, and the sidewalls were covered.

5. **Interconnect Metallization:** Image-reversal photolithography was used to define the metallization area. Then 0.7 ~ 0.8 μm thick Ti/Au metals were evaporated onto the sample. The sample was soaked into

acetone, and the metals were lifted off from the unwanted area. The Interconnect metals formed two connections to the ohmic contacts for DC measurements. Also the ground-signal-ground type of the coplanar waveguide was used during the high speed measurements. The metals were on the highly resistive layers, and went over the insulating layer deposited on the sidewalls of the mesa.

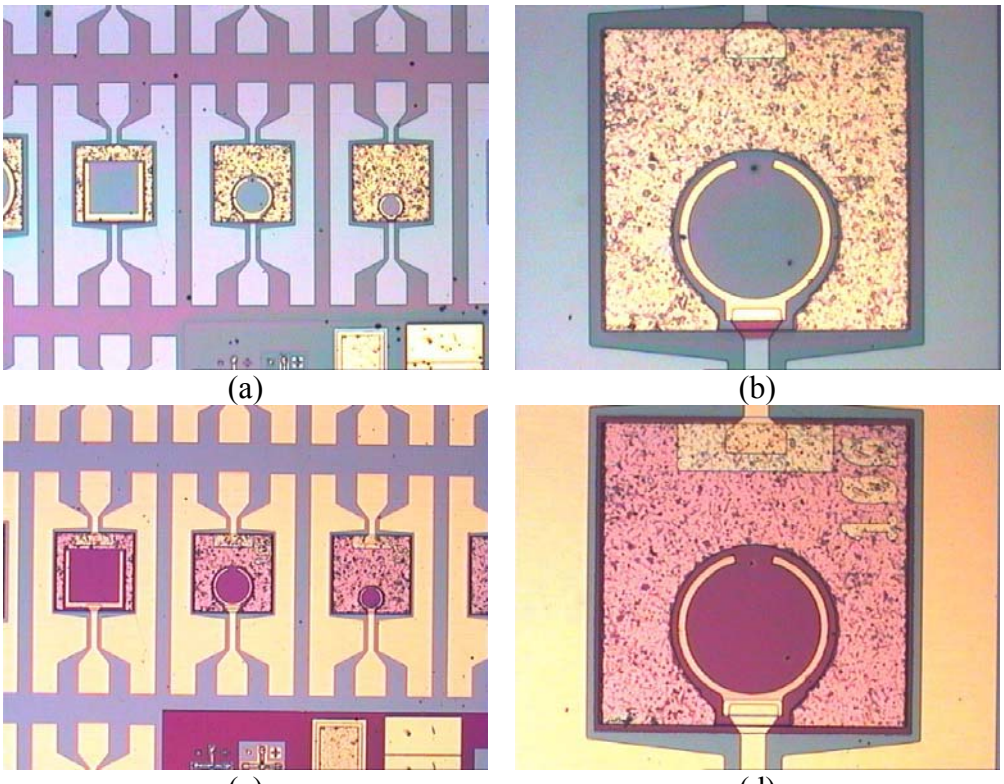

(a) (b)

(c) (d)

Figure 4.11: (a, b) The photoresist before the metallization, (c, d) interconnect metals after the cleaning.

After the interconnect metallization, the photodetectors were ready for the measurements. Figure 4.12 shows SEM picture of these photodetectors.

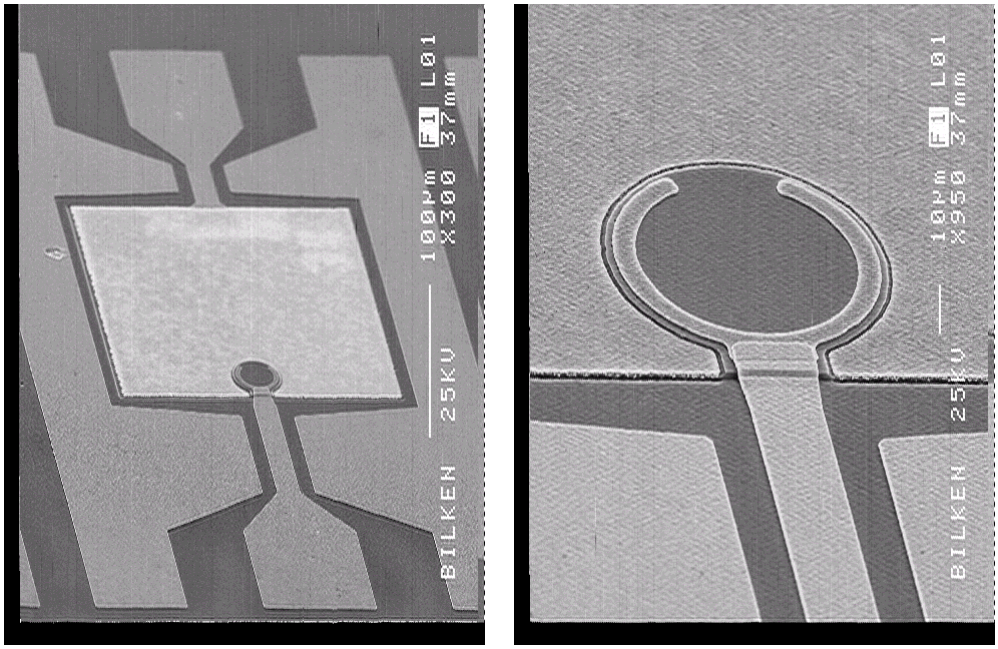

(a) (b)

Figure 4.12: SEM images of large area photodetectors.

4.2.2 Small Area Photodetector Fabrication

The first three fabrication steps were same as the above fabrication. The rest of the fabrication is as follows:

4. **Interconnect Metalization:** The photolithography and the metal deposition were similar to the interconnect metallization used for large area photodetector fabrication. Except the metals were deposited only onto the highly resistive layer without connections to the ohmic contacts.
5. **Surface Passivation and Dielectric Deposition:** After the cleaning, the surface was covered with Si_3N_4 layer. This layer was deposited at 250 ^oC with the PECVD technique. Normal lithography was used to define the area to be etched away. Dilute hydrofluoric acid solution was

used to etch the dielectric layer. The sidewalls and the active area of the photodetector were kept covered. To make an electrical connection in the final step, the top of the ohmic contacts and the nearest connection point of the interconnect metals were cleaned from the dielectric. Also the dielectric coating was etched from the area of the interconnect metal where the high speed and DC probes are touched. This dielectric layer was used for both passivation of the detector surface and formation of the bias capacitors between the n+ ohmic contact of the photodetector and the ground of the coplanar waveguide.

6. **Post layer formation:** After the sample cleaning, the surface was covered with photoresist and normal lithography was used for patterning. Then the sample was baked in the oven at 140 ^{o}C for 30 minutes to harden the photoresist. Then the photoresist was thinned with RIE using oxygen gas.
7. **Airbridge Formation:** Without cleaning, a new layer of photoresist was deposited on the sample. Using the image-reversal photolithography, the connections were patterned on the sample. Then 0.7 ~ 0.8 μm thick Ti/Au metals were evaporated onto the sample. The sample was soaked into acetone, and the metals were lifted off from the unwanted area. With this metallization, the connections between the ohmic contacts and the interconnect metals were formed, and also the top plate of the biasing capacitor deposited. The schematics of this fabrication step are shown in Figure 4.13.

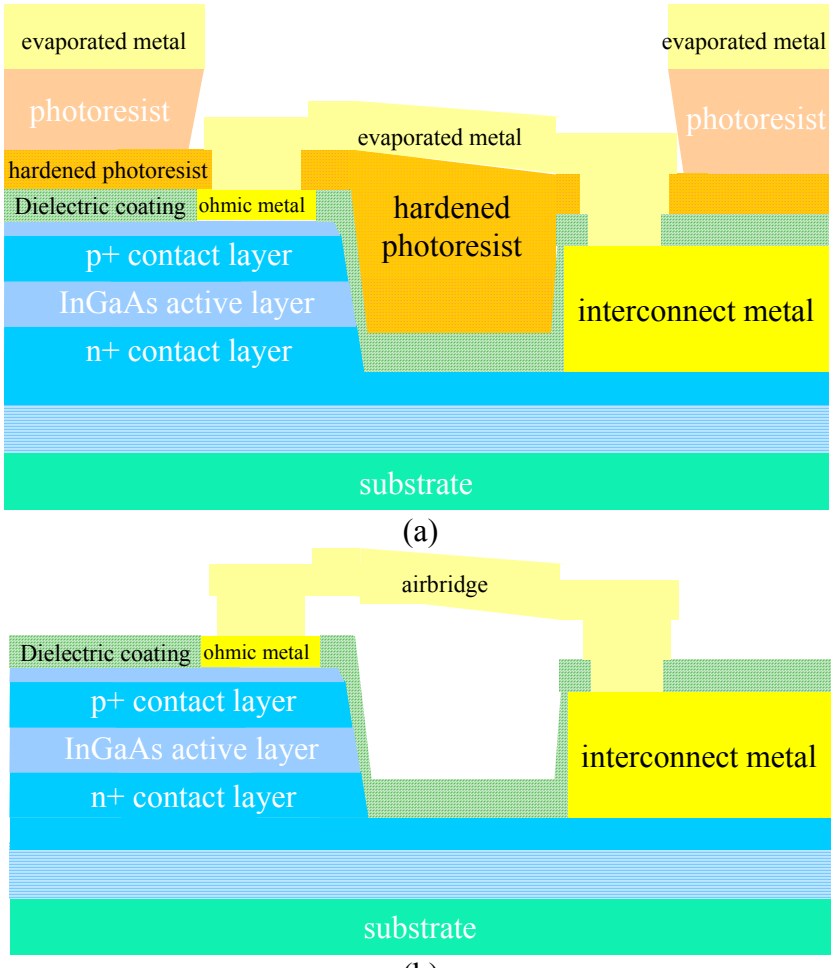

Figure 4.13: Cross-section of the sample (a) after airbridge metallization, and (b) after the liftoff of the metal.

After the airbridge metallization, the photodetectors were ready for the measurements. Figure 4.14 shows SEM picture of the airbridge connections, while Figure 4.15 has the 3D illustration of the photodetector, and the connections made during the current-voltage and responsivity measurements. Figure 4.16 has detailed pictures of small area photodetector.

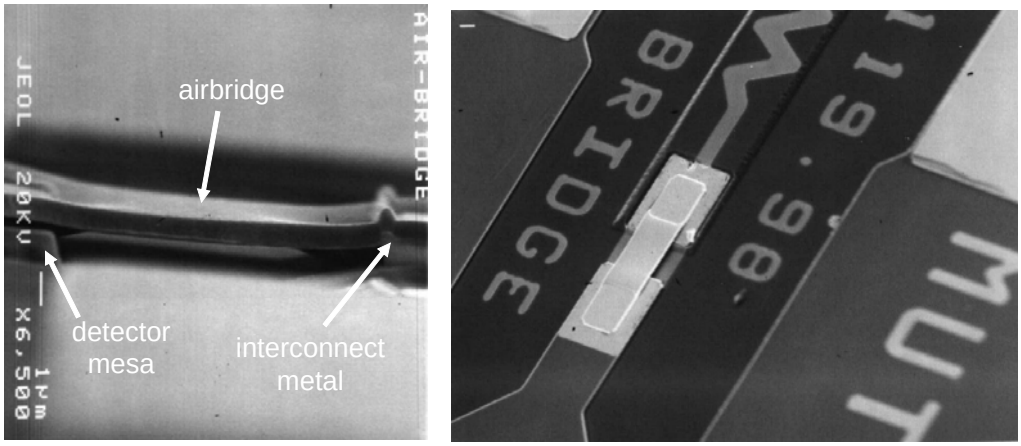

(a) (b)

Figure 4.14: SEM picture of airbridges.

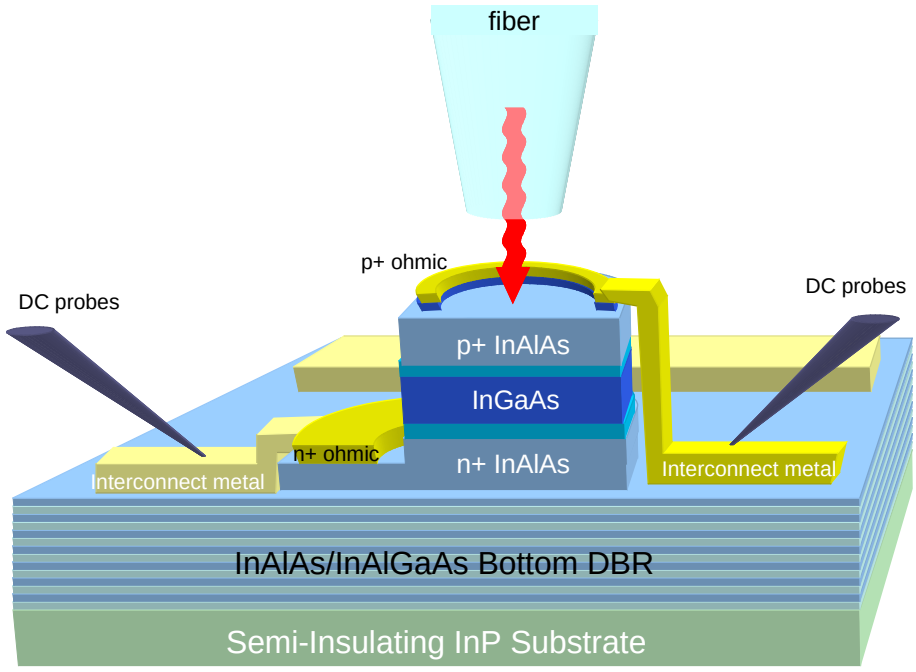

Figure 4.15: 3D illustration of a fabricated photodetector.

4.3 Measurements

Properties of the photodetectors were measured at room (300 K) temperature.

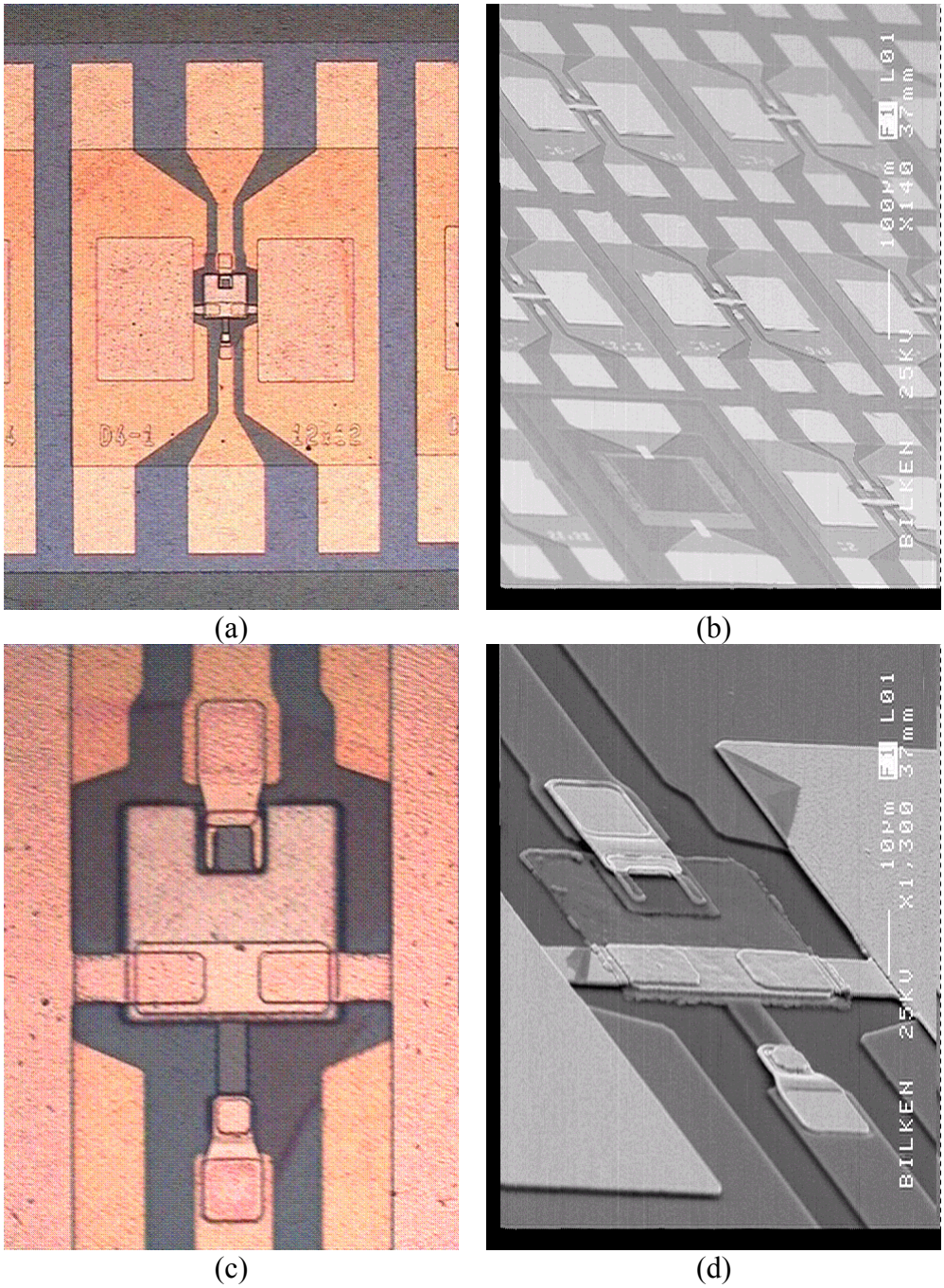

(a) (b)

(c) (d)

Figure 4.16: Pictures of small area photodetectors obtained with optical microscope and SEM.

4.3.1 Current-Voltage Characteristics

The current-voltage (I-V) measurements were done for different area photodetectors between the reverse breakdown voltages to a few volts of forward bias. The current limited not to damage the photodetectors. High forward current caused damage by heating the contact between the interconnect metal and the p+ ohmic metal. The reverse breakdown occurred around 14 volts of bias as shown on Figure 4.17 (a). This breakdown was mainly due to the band-to-band tunneling. Figure 4.17 (b) shows the I-V measurement results for different area photodetectors. The increase of the dark current with the area can be clearly seen.

The analysis of dark current versus area showed that the dark current density decreased linearly with the area for the detectors having diameter greater than and equal to 60 μm. The dark current density of 30 μm diameter photodetectors was 8×10^{-3} A/cm^2 while 60 μm diameter photodetectors was 5×10^{-3} A/cm^2. The dark current for smaller area detectors was similar to the 30 μm diameter photodetector. This showed us that the dark current was governed by generation-recombination current in the surface depletion region. This current can be decreased by using a better passivation layer, or can be completely eliminated by using planar type photodetectors.

We also calculated the differential resistance (R_d) of the photodetectors by simply differentiating the current-voltage data. The maximum value of R_d was at 0.25 V reverse bias for all the photodetectors. The maximum value of R_d had an exponential decay with the area, and the limit value for very large area detectors was 188 MΩ. The differential resistance at zero bias (R_0) had similar behavior. The R_0*A product was 310 Ω·cm^2 for 200 μm diameter photodetectors.

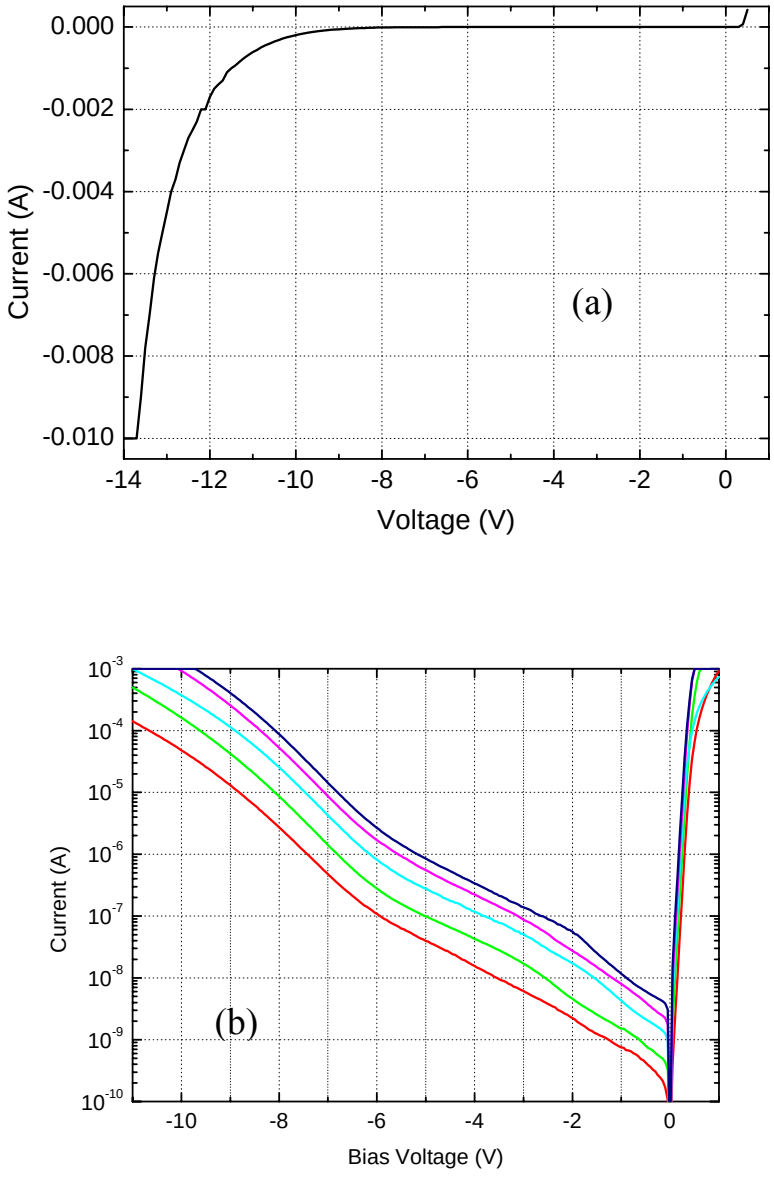

Figure 4.17: (a) Current voltage characteristics of a 30 μm diameter photodetector, where the breakdown can be seen around -14 V bias. (b) The logarithmic plot of I-V characteristics of 30, 60, 100, 150, and 200 μm diameter photodetector (from bottom to top respectively)

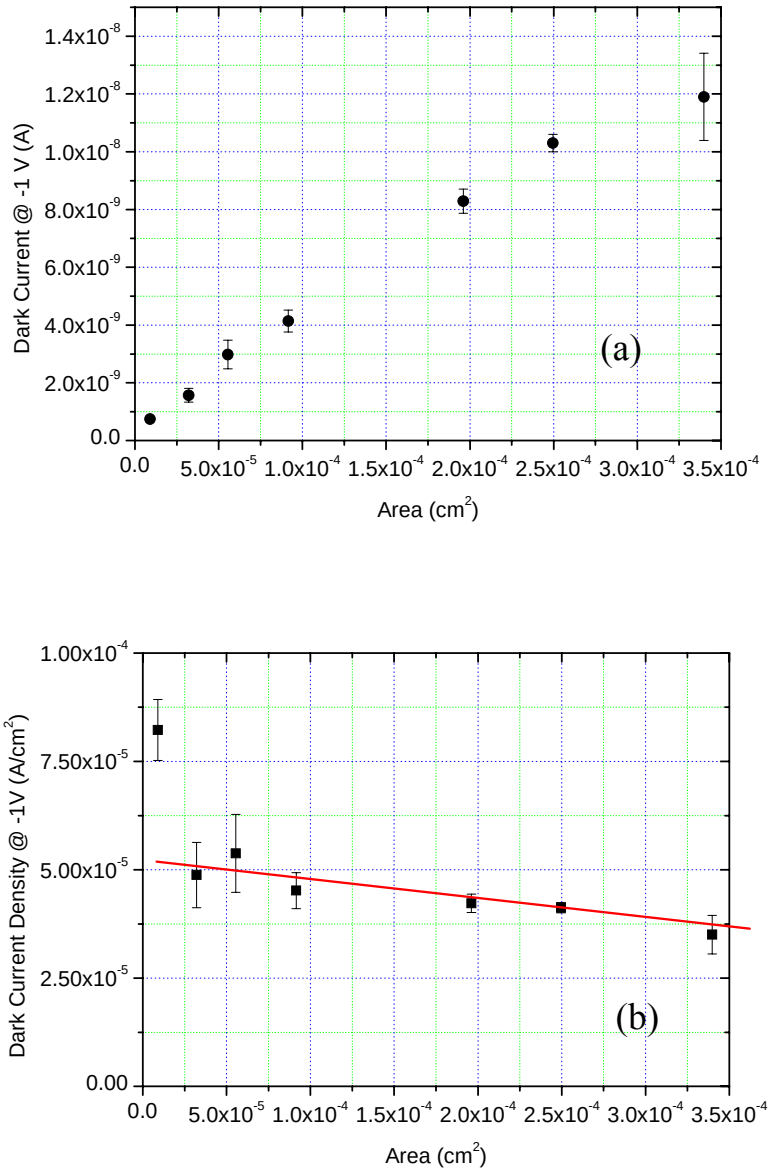

Figure 4.18: (a) Dark current of photodetectors at 1 V reverse bias as a function of detector area. (b) Dark current density of photodetectors at 1 V reverse bias as a function of detector area. The linear decrease can be seen for detectors having 60 μm diameter.

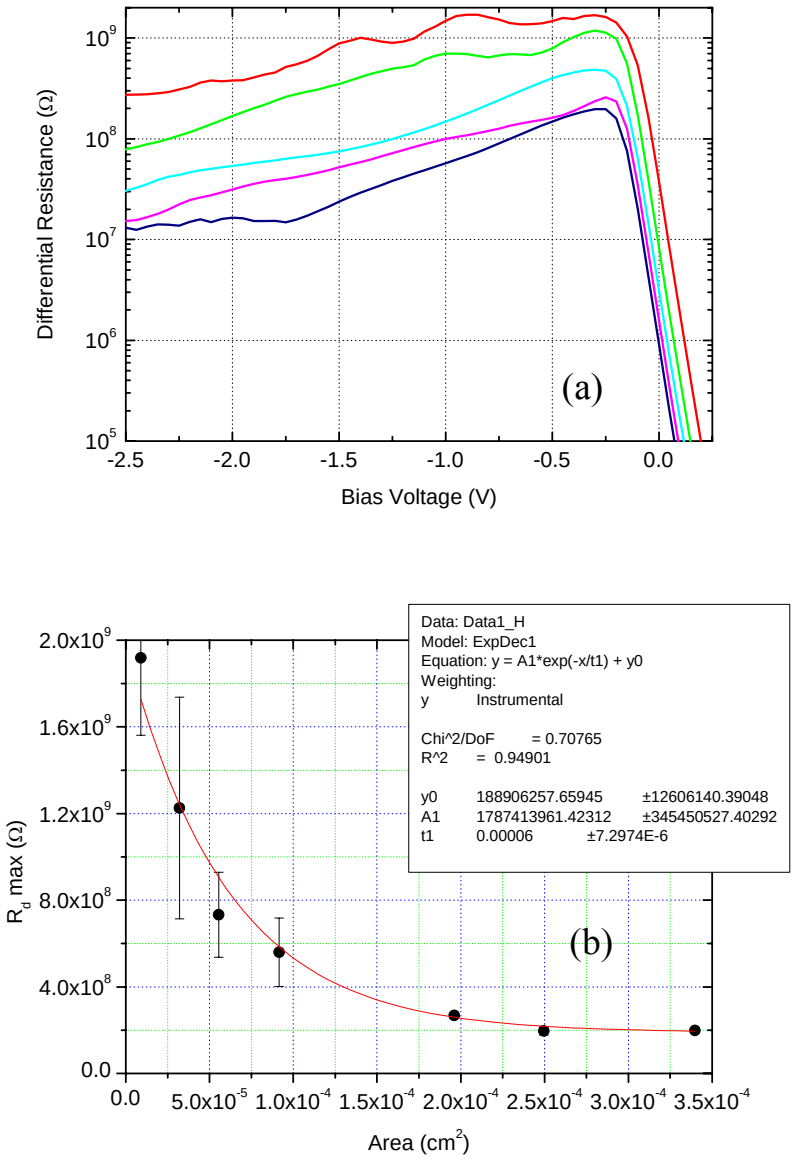

Figure 4.19: (a) Calculated differential resistance of the photodetectors with 30, 60, 100, 150, and 200 μm diameter (from top to bottom respectively). (b) The maximum differential resistance of photodetectors as a function of detector area.

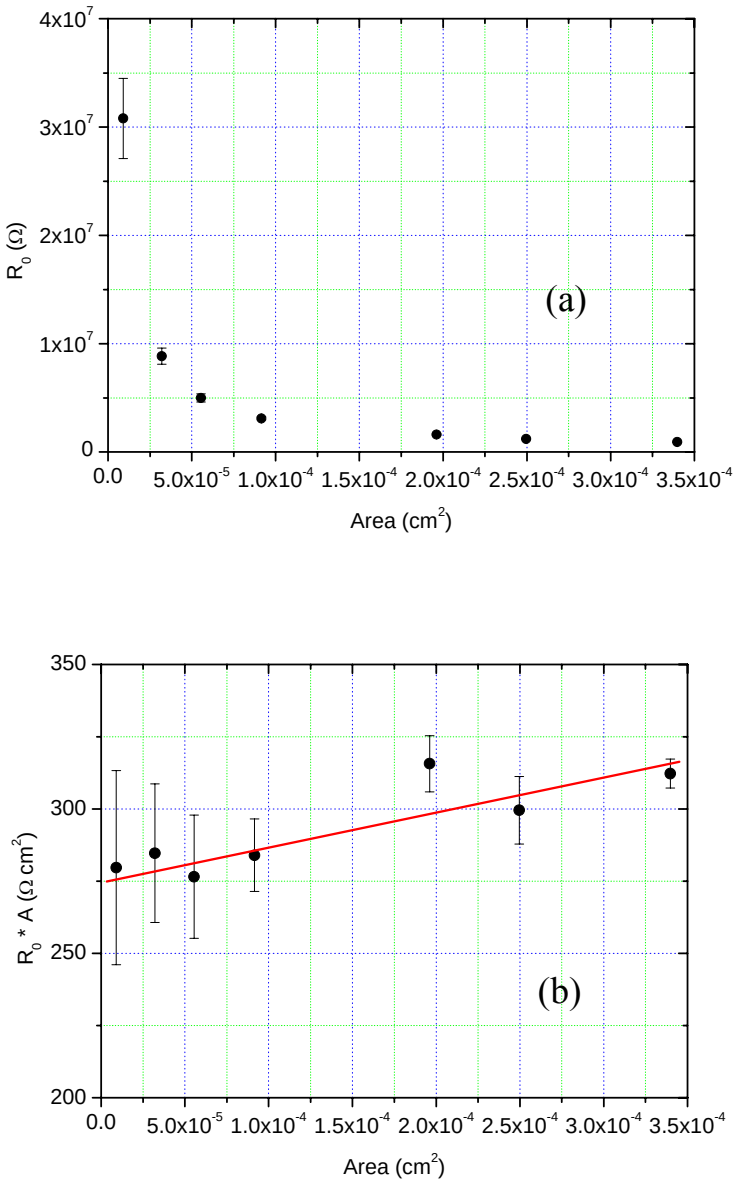

Figure 4.20: (a) Calculated differential resistance of the photodetectors at zero bias. (b) R_0A product as a function of detector area.

4.3.2 Responsivity Characteristics

Photoresponse measurements were carried out in the 1530-1630 nm range using a tunable laser source. The output of the laser was coupled to a single mode fiber. The light was delivered to the devices by a lightwave fiber probe, and the electrical characterization was carried out on a microwave probe station. The top p+ layers were recess etched in small steps, and the tuning of the resonance wavelength within the high reflectivity spectral region of the DBR was observed.

Figure 4.21 (a) shows the spectral quantum efficiency measurements of a device under 5 V reverse bias obtained by consecutive recess etches. Plot 1 is the quantum efficiency after the top InGaAs layer etch, while plots 2, 3, 4, 5, 6, and 7 correspond to cumulative recess etches of 80, 105, 150, 180, 210 and 240 nm, respectively. The peak experimental quantum efficiency 30% of the as-grown sample at 1645 nm increases to 55% at 1614 nm after the first etch. The peak quantum efficiency increased up to 66% with tuning until the resonance wavelength reached 1572 nm. This increase was due to the increase of the absorption coefficient of InGaAs at shorter wavelengths. As we continued the recess etch, the peak quantum efficiency decreased due to the decrease of the reflectivity of the Bragg mirror. The resonance wavelength was tuned for a total of 47 nm (1538 – 1605 nm) while keeping the peak efficiencies above 60%. The peak efficiency was above 50% for the resonant wavelengths between 1550 and 1620 nm, corresponding to a tuning range of 70 nm.

Figure 4.21 (b) shows the quantum efficiency measurement and simulation results of the photodetector when the cavity resonance had been tuned to 1572 nm. The difference between the simulation and the measurement can be explained with the ±3% measurement error of the commercial photodiode that was used for calibration purposes, and the uncertainty of the

layer thickness used during the simulation [72]. The full width at half maximum (FWHM) of the devices was around 35 nm. The quantum efficiency measurements were done at 5 V reverse bias under 0.5 mW optical input power. When we increased the reverse bias beyond 3 V the active layer was fully depleted, and the quantum efficiency increased 6% with respect to zero bias.

The responsivity of the PDs were also measured under various reverse biases up to 7.4 mW optical power, which was the maximum power that could be obtained from the laser. Figure 4.22 (a) shows the photocurrent versus input optical power at the resonance wavelength of 1572 nm. Under 4 V and higher reverse biases, the PDs had a linear photoresponse up to 7.4 mW optical power. At 7.4 mW optical power, the device exhibited a 6.18 mA photocurrent. The corresponding responsivity of the photodetectors was 0.835 A/W. The detector responded linearly to the optical power in four orders of magnitude range under 4 V bias. Figure 4.22 (b) shows the photocurrent versus optical power for 0 and 4 V reverse bias values. The saturation was mainly due to the electric field screening caused by photo-generated carriers inside the active layer [73].

4.3.3 High-Speed Characteristics

High-speed measurements were made with a picosecond fiber laser operating at 1550 nm. The 1 ps FWHM optical pulses from the laser were coupled to the active area of the p-i-n photodiodes by means of a fiber probe. At zero bias, the response of the photodetectors had a long tail due to the diffusion of the carriers in the active layers. Measurements were done under bias to deplete the active layer completely and to get rid of the diffusion tail. Above 5 V reverse bias, we got a Gaussian response with a short tail. Figure 4.23 (a) shows the temporal response of a small area (5×5 μm^2) photodetector measured at 7 V bias by a 50 GHz sampling scope.

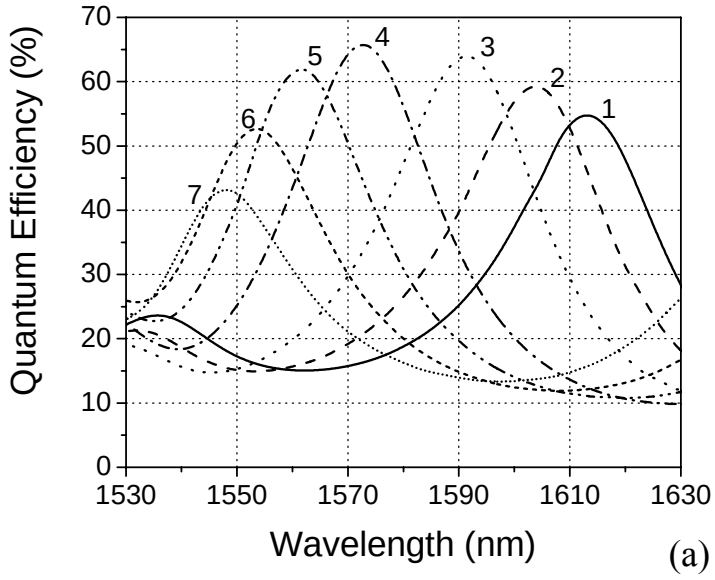

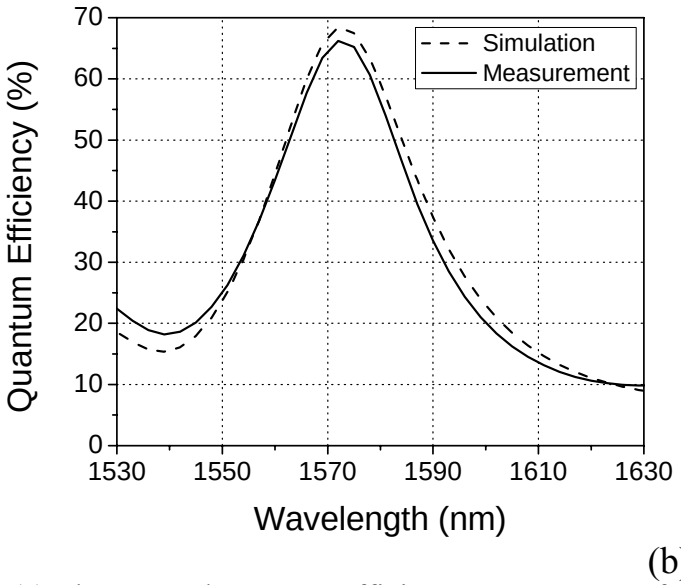

Figure 4.21: (a) The spectral quantum efficiency measurement for successive recess etches. (b) The measurement and calculation of the spectral quantum efficiency with the peak at 1572 nm.

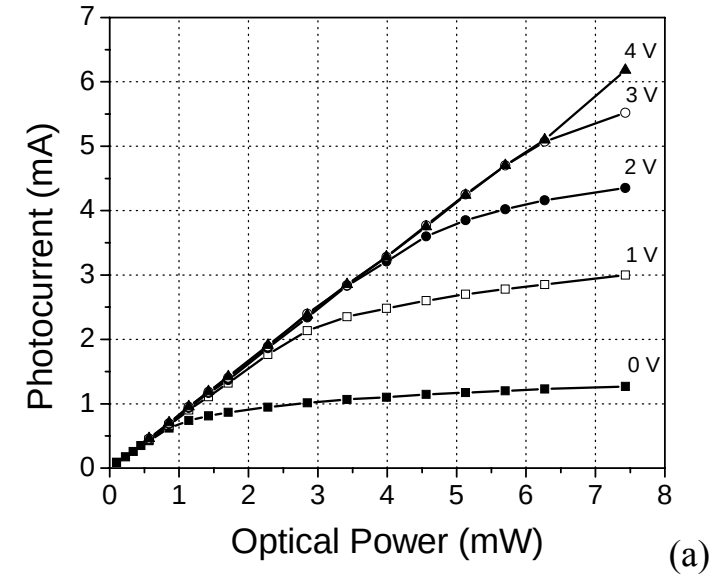

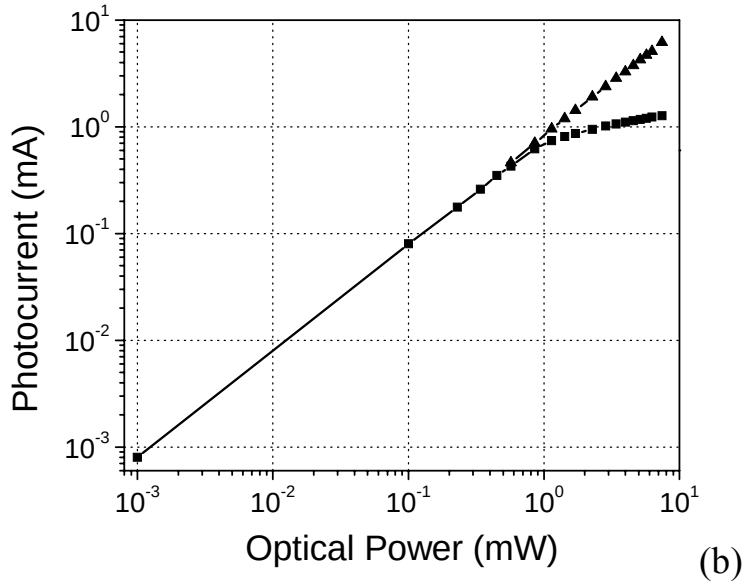

Figure 4.22: (a) The photocurrent vs optical power measurement of the photodetectors under various bias voltages. (b) Log-Log plot of the previous data for 0 and 4 V bias voltages.

The photodiode output had 16 ps FWHM. The measured data was corrected by deconvolving the effect of the 40 GHz bias-tee. After the deconvolution, the device had a 3-dB bandwidth of 31 GHz. Larger area devices (80 μm^2) also showed similar responses, which showed that the temporal response was limited by the transport of the photogenerated carriers. The 120 μm^2 area photodetectors had 28 GHz bandwidth. The measured bandwidth is lower than the theoretically predicted 3-dB bandwidth of 45 GHz. Although grading layers have been implemented to avoid carrier trapping, our measurement data shows that the device performance is still limited by the carrier trapping. In our devices, we used a digital grading that consisted of InP lattice matched InGaAs/InAlAs layers. A linear grading may further improve the device performance [74].

4.4 Conclusion

We have demonstrated high-speed, and high-efficiency resonant cavity enhanced (RCE) InGaAs based p-i-n photodetectors. A peak quantum efficiency of 66% was measured along with 28 GHz bandwidth, which corresponds to 18.5 GHz bandwidth-efficiency product. The photoresponse was linear up to 7.4 mW optical power, where the devices exhibited 6.18mA photocurrent.

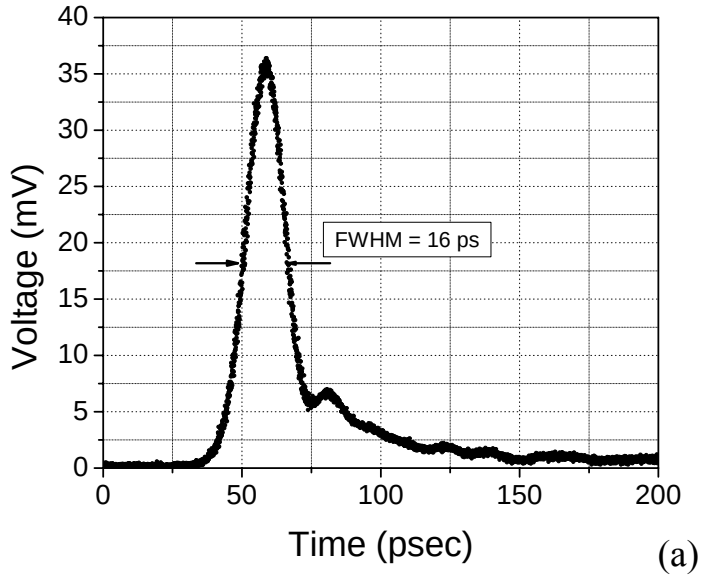

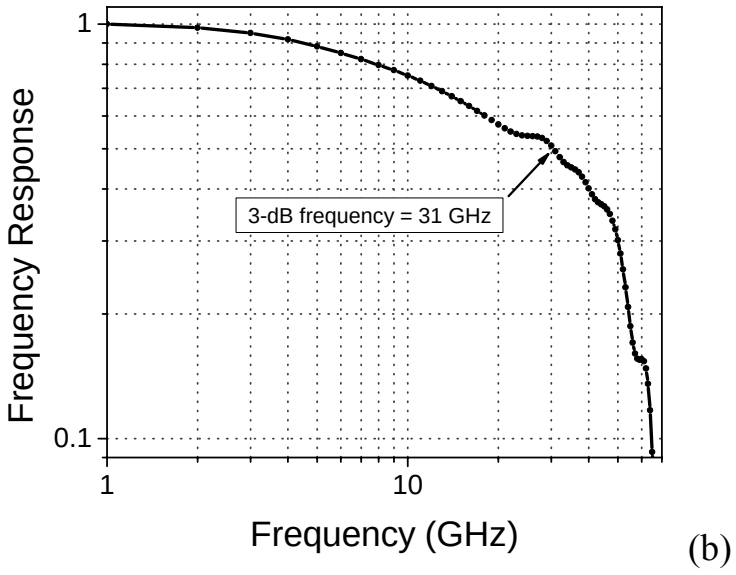

Figure 4.23: (a) The temporal response of 5×5 μm^2 area photodetector under 7 V reverse bias. (b) The calculated frequency response of the photodetector.

Chapter 5

InSb p-i-n Photodetector

The spectral region above the visible range is called as the infrared spectrum. The electromagnetic spectrum with the wavelength 1 μm and 14 μm is divided into three regions that are separated by strong atmospheric absorption. These absorptions are mainly due to carbon dioxide (CO_2), carbon monoxide (CO), and water (H_2O) vapor present at the atmosphere. Near-infrared radiation (near-IR) lies in the most energetic window, stretching from the upper edge of the visible spectrum around 850 nm to a region of strong attenuation near 3 μm. The mid-wavelength infrared (mid-IR) region lies between 3 and 5 μm, with the long-wavelength infrared (long-IR) window stretching from the upper edge of the broad absorption to an upper limit of 14 μm. Figure 5.1 shows the spectral transmission of the atmosphere at the sea level.

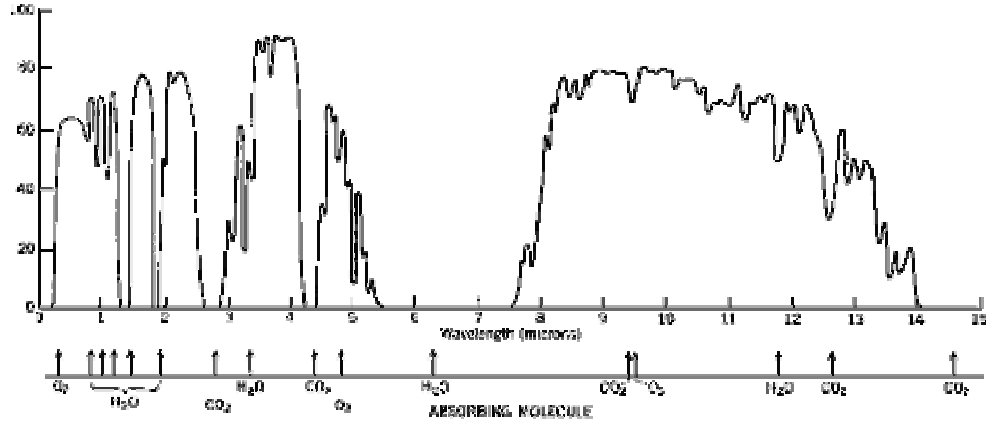

Figure 5.1: Spectral transmission of the atmosphere at the sea level.

Infrared detectors can be used in thermal imaging systems, free space communication, and chemical agent monitoring. The peak black body emission from hot surfaces has the in the mid-IR spectrum. Hence military applications include early warning systems, and night vision. Most of the carbon hydrates (HC) such as methane, propane, and natural gases used for the heating, carbon dioxide (CO_2), carbon monoxide (CO), nitrous oxide (NO_x) has absorption band in the mid-IR region. Table 5.1 lists a few of these gases that have absorption in the mid-IR region.

Table 5.1: Gases and their absorption properties.

Gas	Absorption Wavelength (μm)	
Methane (CH_4)	3.20 ~ 3.45	Flammable
Acetylene (C_2H_2)	2.99 ~ 3.04	Fire
Ethylene (C_2H_4)	3.10 ~ 3.40	Fire
Ethane (C_2H_6)	3.30	Fire
Methyl Chloride (CH_3Cl)	3.22 ~ 3.38	Fire
Hydrogen Chloride (HCl)	3.33 ~ 3.70	Inhale Hazard
Hydrogen Bromide (HBr)	3.82	
Carbon Dioxide (CO_2)	4.23	
Carbon Monoxide (CO)	4.60	
Nitric Oxide (NO)	5.25	
Nitrous Oxide (N_2O)	4.47	
Nitrogen Dioxide (NO_2)	6.14	

The detection of these gases in the atmosphere has many industrial and indoor applications, such as indoor air quality measurement, automotive and flue gas emissions, hazardous are warning signals, gas leak detection, patient monitoring, and alcohol breath analyzers. In all these applications, it is possible to use non-dispersive infrared (NDIR) sensors. These sensors contain a light

source emitting light only in a specified spectrum, and an infrared detector to measure the absorbance of the atmosphere. Another application is the free space communication, which is becoming popular for short distance high speed communication. These systems do not require cables or fibers, instead send the optical signals directly in the atmosphere between two endpoints.

Although variable-bandgap HgCdTe has been used for many years in military and commercial applications, it is being replaced by quantum well or InSb photodetectors due to the technological difficulties [75]. Other possible option is the quantum-well infrared photodetectors. But the normal incidence operation is not possible for these detectors, unless special gratings are integrated on the surface.

InSb is the common material for the mid-infrared (mid-IR) range photodetectors with the cut-off wavelength of 5.4 μm at 77 K as shown in Table 5.2. Ternary compounds of InSb has been used with the addition of As, Bi, or Tl to extend the responsivity to the far infrared region [76,77]. Although these detector structures can be fabricated on InSb, GaSb or InAs substrates, this method is not preferred due to low resistance of the substrate and the difficulty of thinning process for the back illuminated focal plane arrays [78-80]. Instead Si and GaAs substrates are more attractive even there is a significant lattice mismatch between the substrate and epitaxial layers [81-83]. Although optical and electrical properties have been studied over the years, high-speed properties of InSb based photodetectors have not been reported before in the scientific literature.

This chapter presents our effort to fabricate high speed and high efficiency photodetector operating in the mid-infrared (MIR) wavelength range.

Table 5.2: Properties of some low energy gap semiconductors.

	InSb	InAs	GaSb	AlSb
Energy band-gap E_g (eV)	0.235 (0K) 0.170 (300K)	0.418 0.354	0.811 0.720	1.686 1.615
Cut-off wavelength λ_g (μm)	5.28 (0K) 7.29 (300K)	2.97 3.50	1.53 1.72	0.74 0.77
Band Type	D	D	D	I
Crystal structure	Z	Z	Z	Z
Lattice parameter (Å)	6.4794	6.0584	6.0959	6.1355
Density (g cm^{-3})	5.775	5.667	5.614	4.26
Melting point (K)	800	1215	985	1338
Intrinsic carrier conc. (cm^{-3})	2.0×10^{16}	1.3×10^{15}		
Electron mobility (cm^2 / V·s)	80000	33000	5000	200
Hole mobility (cm^2 / V·s)	1250	460	850	420
Effective electron mass (m_0)	0.0145	0.023	0.042	0.12
Effective hole mass (m_0)	0.40	0.40	0.40	0.98

5.1 Design

We designed a p-i-n type InSb based photodetector structure to be grown on semi-insulating GaAs wafer. The detector structure was grown by molecular beam epitaxy method by SVT Associates in USA. A 0.1 μm thick GaSb layer was grown as a buffer between lattice mismatched GaAs and InSb layers. InSb growth conditions and the thickness of the buffer layer were controlled using a Reflection High Energy Electron Diffraction (RHEED). After the buffer layer a 1.5 μm thick n+ InSb layer, 1.5 μm thick n- InSb layer, and finally the 0.5 μm thick p+ InSb layer were grown. The n- active layer was unintentionally doped to 2×10^{15} cm^{-3}. Tellurium and Beryllium were used as the n- and p- layer dopants, respectively. The properties of these layers are also shown on Table 5.3. Doping level was 10^{18} cm^{-3} for both highly doped layers to decrease the serial resistance. The thickness of the top p+ layer was kept lower than the n+ layer to increase the quantum efficiency.

Table 5.3: Epitaxial layers of InSb p-i-n photodetector.

Material	Thickness (nm)	Type	Doping	Concentration (cm^{-3})
InSb	500	p+	Be	1×10^{18}
InSb	1500	n-	Te	2×10^{15}
InSb	1500	n+	Te	1×10^{18}
GaSb Buffer Layer				
Semi-Insulating GaAs Substrate				

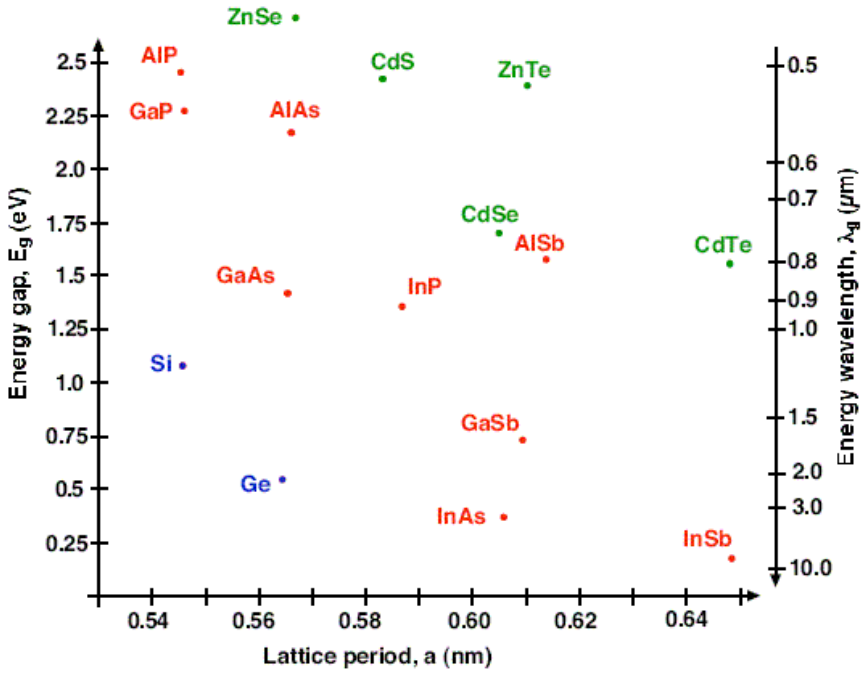

Figure 5.2: Lattice constant and energy gap of semiconductors.

5.2 Fabrication

Before a complete fabrication, we tried to optimize etch of InSb. Due to thick epitaxial layers, deep etches had to be performed. RIE etch was impossible with the gases present in our system due to nonselective etch of InSb and photoresist. A few wet etch recipes were used for the optimization process.

- HNO_3 : HCl : H_2O (1:1:8) solution was use and no significant etch was observed after 12 min etch.
- HNO_3 : HF : H_2O (1:1:6) solution was used. Reasonable etch rate was observed at first, but this solution was not suitable for further etch due to surface corrugation.
- H_3PO_4 : H_2O_2 : H_2O solution had etch rates between 3 nm/sec (1:1:8) to 5 nm/sec (1:1:4). But this solution either non-uniformly etched InSb and GaSb layers or did not etch some regions. Fig 5.3(a) shows the etch profile of ohmic transmission line rectangle. The InSb layer was etched more at the edges. Fig 5.3(b) shows the photograph of the same pattern. All the layers can be seen as the result of non-uniform etch. Fig 5.3(c) shows the area that has not been etched.
- Citric acid ($C_6H_8O_7$): H_2O_2 (1:1) solution had the best result in terms of uniformity. Citric acid was prepared mixing citric acid monohydrate and water (100 g to 100 ml) at 80 ^oC. Then citric acid was cooled to room temperature. During etch, the solution was kept at 30 ^oC, and stirred for uniformity. The etch rate of the InSb was around 25 nm/min, which is much lower than the above solutions. As the duration of etch was high, the solution usually penetrates through the edge of the resist and causes high under-etch. Thus the surface had to be protected by a dielectric layer. A combination of Si_3N_4 and photoresist was used as the mask during wet etches. This etch is isotropic and the under-etch and the Si_3N_4 mask can be seen on the figure 5.3(d).

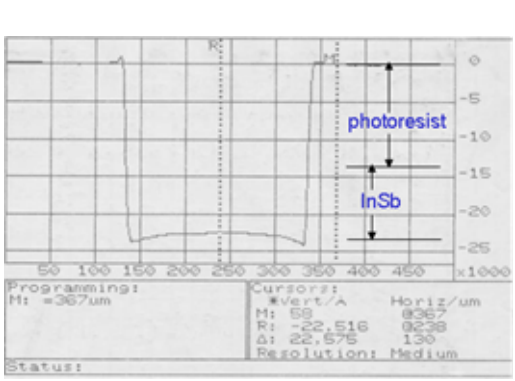

(a)

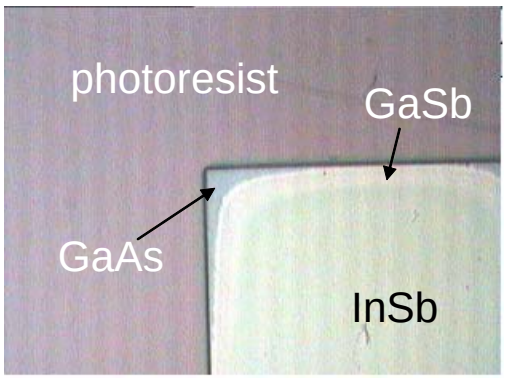

(b)

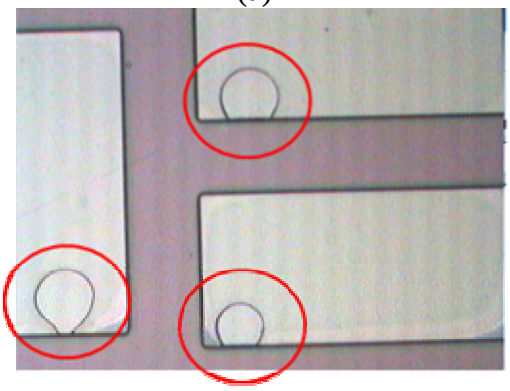

(c)

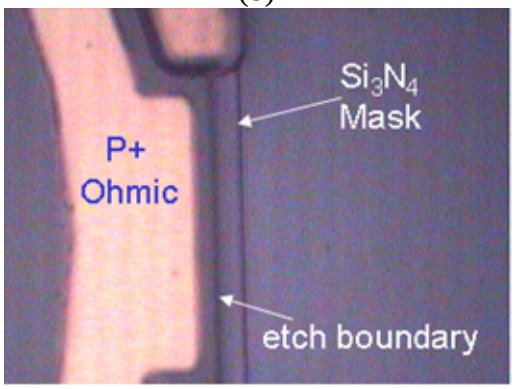

(d)

Figure 5.3: Details from InSb wet etch.

Before the fabrication, the surface was covered with 100 nm thick Si_3N_4 using PECVD. This layer was kept until the end of the mesa etch step. The devices were fabricated by a microwave-compatible process and completed in five steps.

1) **n+ ohmic contact formation:** After the lithography, the Si_3N_4 layer was etched with RIE. Using citric acid solution, the sample was etched down to the top of the n+ InSb layer with a total depth of 2.4 μm. The under-etch was around 2 μm. This amount of under-etch was not critical for the consecutive contact. Titanium (12 nm) and gold (240 nm) were deposited and lifted-off.

2) **p+ ohmic contact formation:** Following the lithography, Si_3N_4 was etched using dilute hydro fluoric acid. After etch, titanium (12 nm) and gold (160 nm) were deposited and lifted-off.

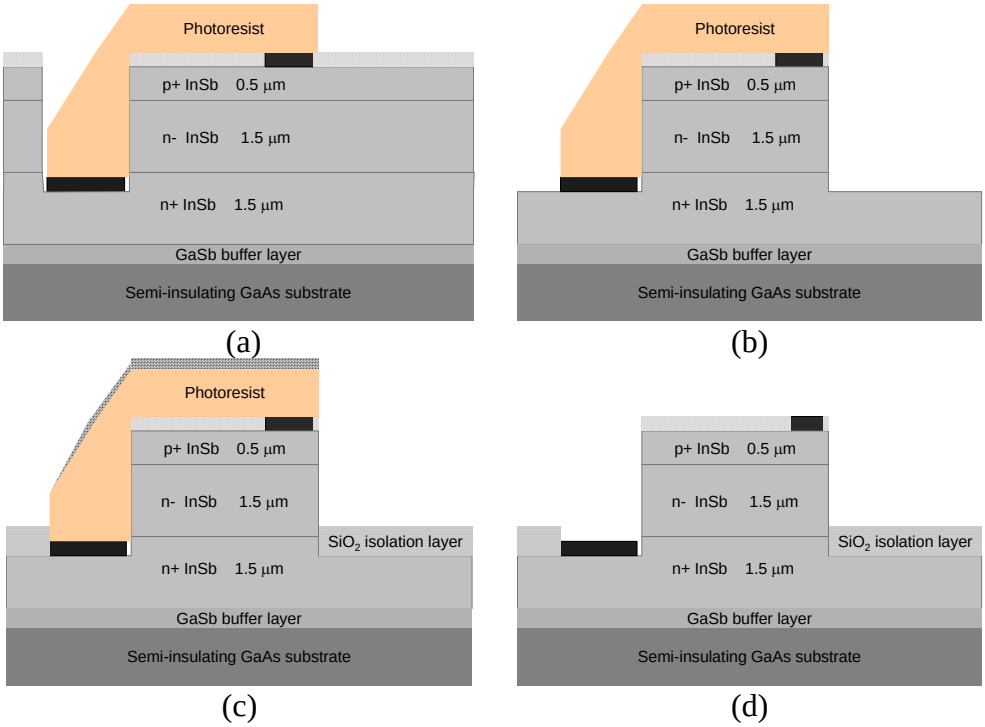

Figure 5.4: Modified mesa isolation step used during the fabrication of InSb photodetectors.

3) **Mesa isolation etch:** Active area and the n+ ohmic contacts were protected with dielectric and photoresist. We used two different methods for the mesa isolation. The first was similar to the fabrication of the previous GaAs and InGaAs based photodetectors. All the layers were etched down to the semi-insulating GaAs substrate. The total height of the mesa was around 4 μm. The tall mesa was a major problem for small area detectors, as it was impossible to make image-reversal lithography, which was essential for thick interconnect

metallization. Due to this problem the mesa etches were modified. The second method had a thinner etch and an additional dielectric deposition. The layers were etched down to 2.4 μm. Without cleaning the photoresist, 0.5 μm thick SiO_2 layer was grown on the sample using PECVD at 80 ^oC. This layer later acted as the insulating medium between the highly conductive InSb layer and the interconnect metal. Very thin dielectric layer was also deposited on top of the photoresist, but the photoresist was lifted-off without problem. Finally the thin Si_3N_4 layer was removed with diluted HF solution. These steps are shown on Figure 5.4.

4) **Dielectric deposition:** The whole sample was covered with Si_3N_4 layer that acts as both passivation and antireflection coating. After the lithography, some regions on top of the ohmic contacts were etched with diluted HF solution.
5) **Interconnect metallization:** After the image reversal lithography, titanium (12 nm) and gold (800 nm) were deposited and lifted-off.

The photodetectors were fabricated with different active areas changing from 30 to 150 μm in diameter. Figure 5.5(a) shows the cross-section of a fabricated photodetector, while the photograph of 150 μm diameter photodetector is shown on figure 5.5(b).

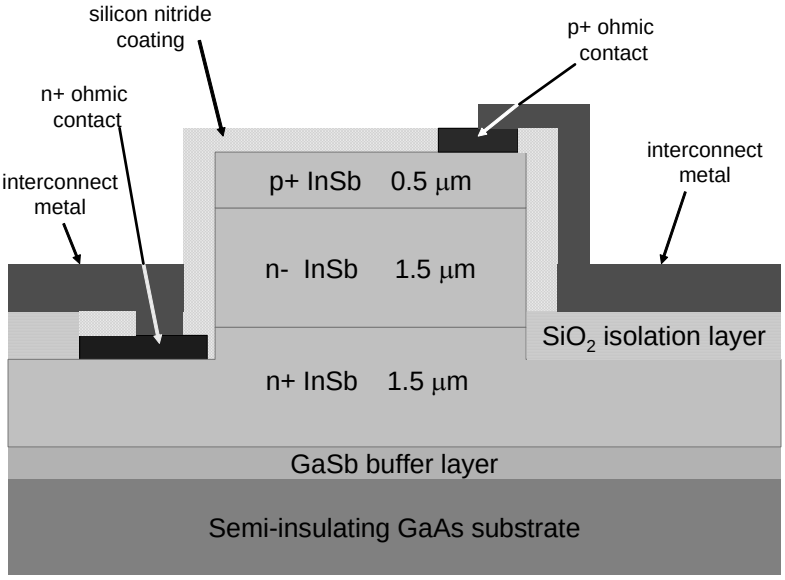

(a)

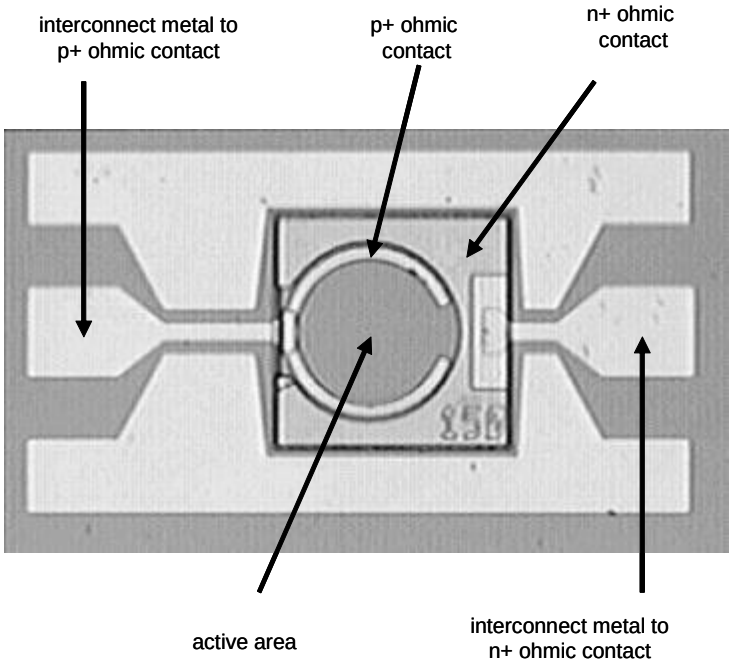

(b)

Figure 5.5: (a) Cross-section of a fabricated photodetector (b) Photograph of photodetector with 150 μm diameter.

5.3 Measurements

Properties of the photodetectors were measured both at room (300 K) and liquid nitrogen (77 K) temperature.

5.3.1 Current-Voltage Characteristics

Current-voltage (I-V) characteristics of the photodetectors were measured using a Modular DC Source/Monitor Unit. Photodetectors were biased between –2.0 and +0.5 volts at 300K background. Active area of the photodetectors ranged from 7.06×10^{-6} cm^2 (30 μm in diameter) to 2.25×10^{-4} cm^2 (150×150 μm^2). Initially I-V measurements were done at room temperature. Diode characteristics were observed only at small area (30 and 60 μm diameter) photodetectors. This is due to the high carrier concentration at the lightly doped layer. Room temperature carrier concentration of InSb is above 2.0×10^{16} cm^{-3} for epitaxial layers grown on GaAs substrate due to lattice mismatch. This high carrier concentration prevented us from observing a good p-n junction. Then the temperature of the sample was decreased to 77 K.

Figure 5.6(a) shows the I-V characteristics of 30 μm diameter photodetector. At room temperature dark current was 6.4 μA at zero bias and 4 mA at 1 V reverse bias. At 77 K, the dark current was 20 nA at zero bias and 41 μA at 1 V reverse bias. Figure 5.6 (b) shows the calculated differential resistance of the photodetector. At room temperature differential resistance was 65 Ω at zero bias, and the highest value was 650 Ω at 440 mV reverse bias. The peak position of the differential resistance shifted to higher bias voltages as the temperature was lowered [84]. When the diode was cooled to 77 K, the differential resistance at zero bias was 150 kΩ and the highest value was 170 kΩ at 40 mV forward bias.

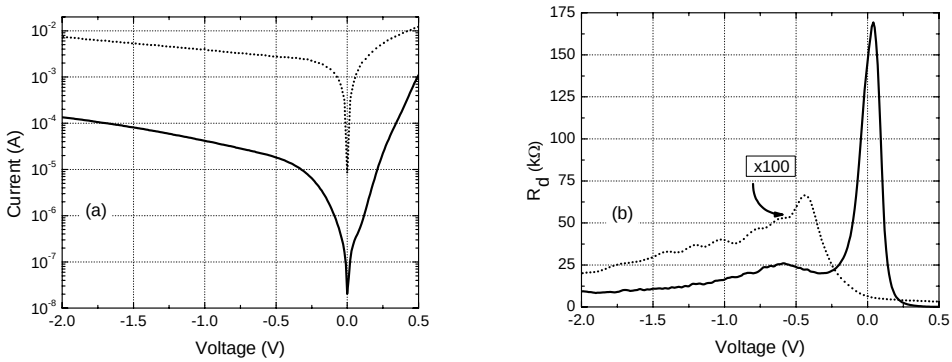

Figure 5.6: Current-voltage characteristics and differential resistance of 30 μm diameter photodetector at 300 K (dotted line) and 77 K (solid line).

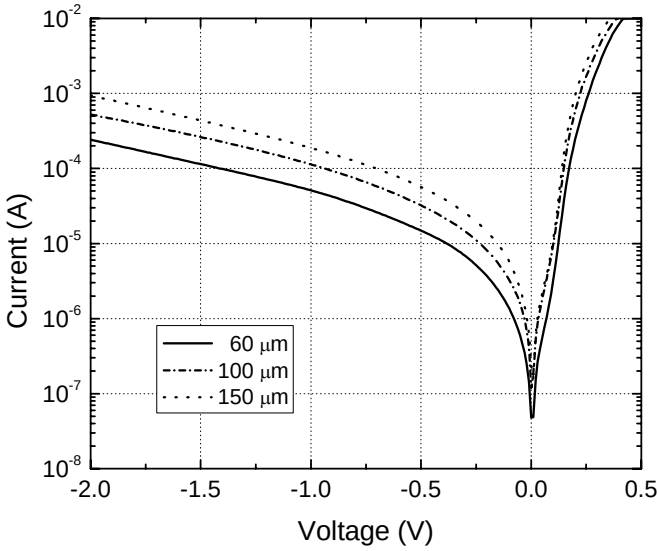

Figure 5.7: Measured current-voltage characteristics of 60, 100, and 150 μm diameter photodetectors at 77 K.

Figure 5.7 shows the I-V characteristics of cooled photodetectors with 60 μm, 100 μm, and 150 μm diameter. Dark current of the photodetectors gradually increased with the increasing active area. Dark current at zero bias were 48 nA,

118 nA, and 239 nA for 60 μm, 100 μm, and 150 μm diameter photodetectors respectively.

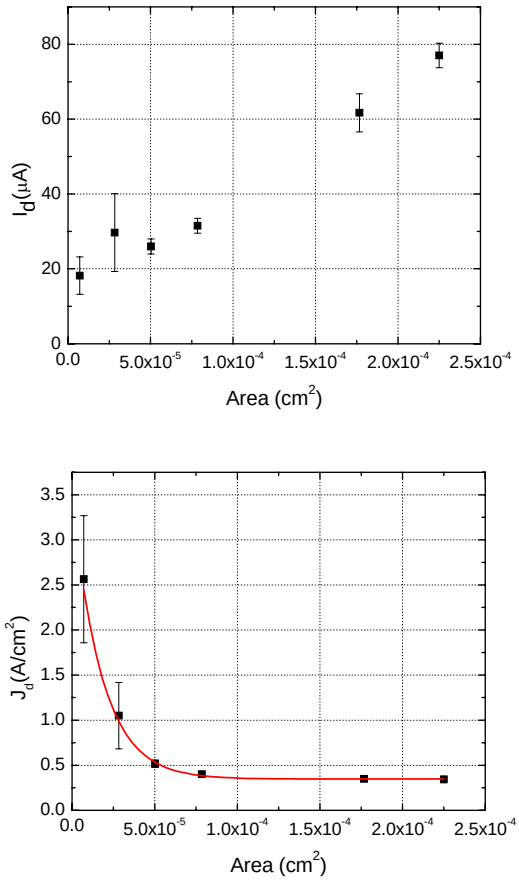

Figure 5.8: (a) Dark current at -0.5 V as a function of area, while (b) shows the dark current density (J_0) as a function of area.

Figure 5.8(a) shows the dark current of the photodetectors at -0.5 V bias. A linear increase can be seen for large area photodetectors. When the dark current density was calculated at -0.5 V bias at 77 K, we saw that dark current density was large for small area photodetectors. The calculated values can be seen on Figure 5.8 (b). Dark current density (J_0) analysis as a function of area showed that the surface diffusion and generation current was dominant for low reverse

bias values [85]. The exponential fit to the J_0 vs. area data showed that the limit value for the large photodetectors was 0.34 A/cm^2.

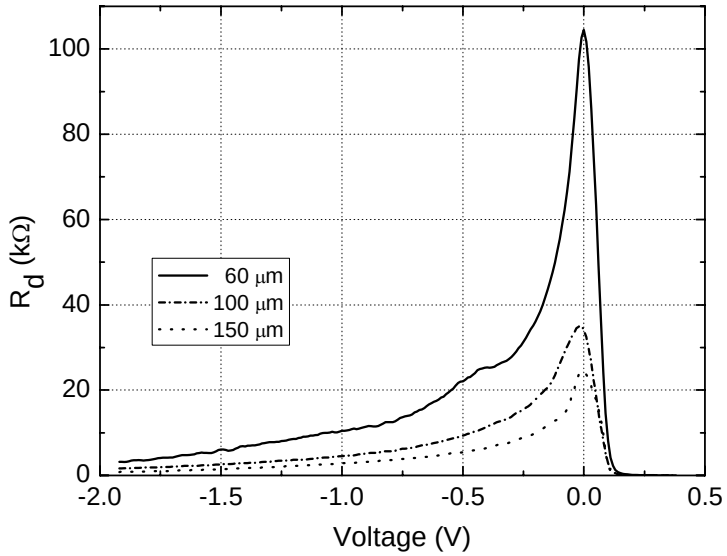

Figure 5.9: Calculated differential resistance (R_d) as a function of bias voltage.

Finally the differential resistance (R_d) of the photodetectors was calculated by differentiating the current-voltage data. Figure 5.9 shows the R_d as a function of bias voltage. The peak value of R_d was at 0 V bias, and gradually decreased as we increased the reverse bias voltage. Zero bias differential resistance (R_0) showed an exponential decrease as a function of area that is represented in Figure 5.10(a). According to this fit, R_0 had almost constant value of 20 kΩ for large area detectors. Zero-bias differential resistance area product (R_0A) for 30 μm diameter diodes was 1 $\Omega \cdot cm^2$. This product increased to 4.5 $\Omega \cdot cm^2$ for 150×150 μm^2 area diodes. Our values were comparable to the reported R_0A values. The R_0A for InSb photodetectors grown on Si were 1 $\Omega \cdot cm^2$ (400×400 μm^2 area) and 2.6 $\Omega \cdot cm^2$ (400×80 μm^2

area) [84,85]. R_0A was 0.5 $\Omega \cdot cm^2$ for 50×200 μm^2 area InAsSb photodetector grown on GaAs [82].

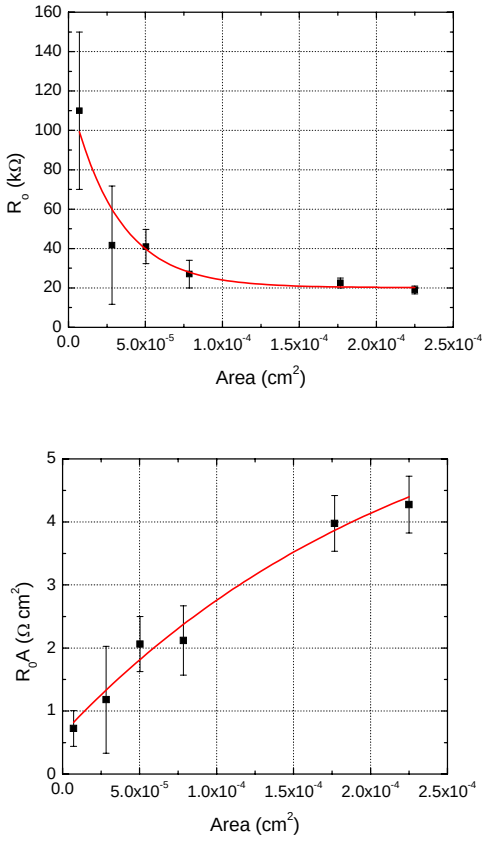

Figure 5.10: (a) The zero bias differential resistance (R_0) as a function of detector area. (b) Resistance-area product (R_0A) as a function of detector area.

5.3.2 Responsivity Characteristics

Responsivity measurements were initially done at room temperature using a tunable laser diode. The output of the laser was coupled to a single-mode fiber and delivered to the active area of the photodetector using a fiber probe. The photocurrent was recorded by digital ammeter while the detectors were biased using a DC voltage source. First the responsivity of the photodetectors at 1550

nm was measured as a function of bias voltage. The responsivity increased with the increase of the reverse bias as shown in Figure 5.11. Under 0.2 V reverse bias the responsivity was 0.58 A/W, which corresponds to 46 % quantum efficiency (QE). Due to the internal gain, the QE exceeded unity with the increase of the reverse bias above 0.6 V. Spectral responsivity measurements were made in the 1500 – 1600 nm spectral range which were also shown at the inset of Figure 5.11. The photoresponse was nearly constant in the given range.

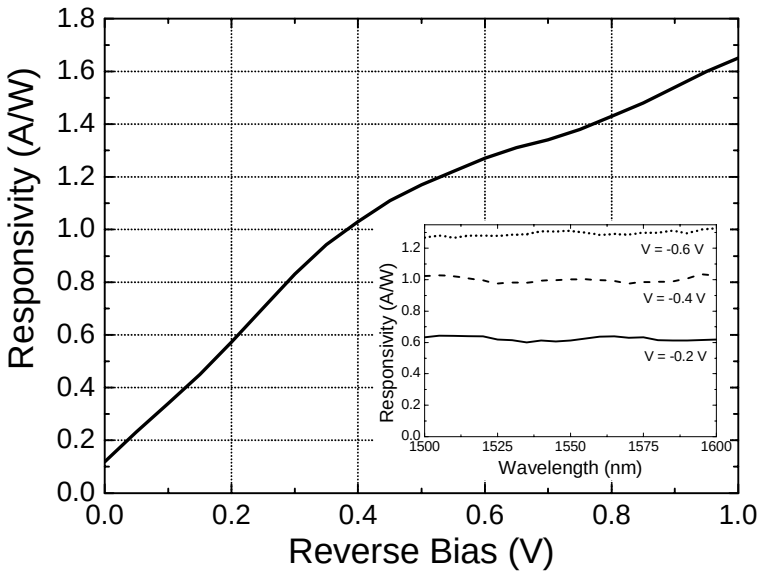

Figure 5.11: Responsivity of the photodetectors at 1550 nm as a function of the reverse bias. The inset shows the spectral responsivity measurement under different reverse bias voltages ranging from 0.2 to 0.6 V.

These results were also in agreement with the spectral absorption simulations based on the transfer matrix method. Figure 5.12 shows the simulation results of reflection and absorption for the fabricated detector. Below 1400 nm, most of the optical signal was absorbed in the upper p+ InSb

layer due to high absorption coefficient [86, 87]. Between 1400 and 2000 nm, the absorption in the n- layer was nearly constant. Simulations show that a further increase in the QE can be achieved by using a thinner p+ layer and by tuning the anti-reflection coating to the desired wavelength.

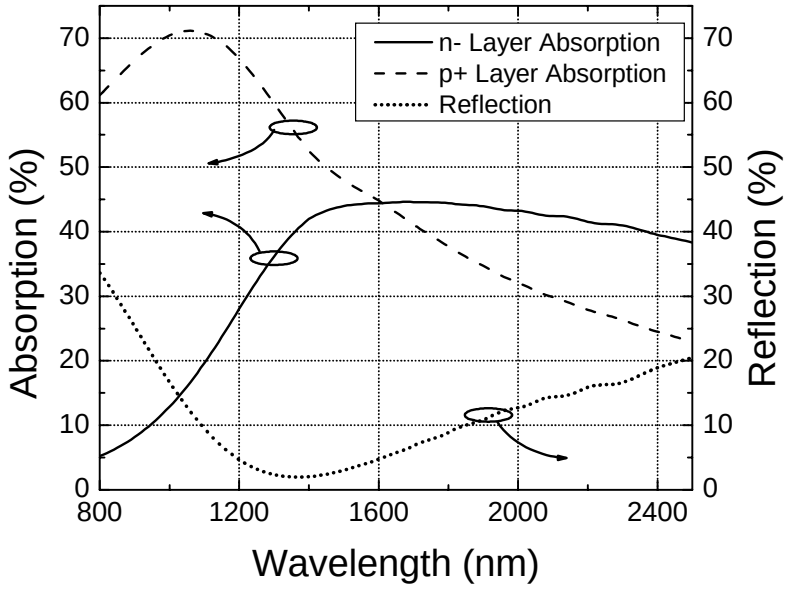

Figure 5.12: Spectral simulation results for optical reflection and absorption in the p+ and n- InSb layers.

After obtaining these results at room temperature, the measurements were repeated at 77 K. Samples were mounted on an alumina substrate with thermally conductive epoxy. Electrical connections were made with wire bonding. Alumina holder was placed in a dewar with ZnSe optical window for characterization. A blackbody at 774 K was used as the infrared (IR) light source. The amplitude peak of the radiation from the source was at the mid-IR wavelength region. Detector signal and noise were measured using a low noise preamplifier and a lock-in amplifier, while the IR light was chopped at 680 Hz.

Figure 5.13: Picture of the setup from Electrical Engineering of METU.

The spectral measurements were made in 2.5 μm to 6.0 μm wavelength range using an Oriel MIR-8000 FTIR system and a pyroelectric reference detector. Figure 5.14 shows the 77 K spectral response of 80 μm (solid line) and 60 μm (dotted line) diameter photodetectors. The cut-off wavelength (where the responsivity dropped to half of the maximum) was 5.33 μm. This corresponded to an energy bandgap of 0.23 eV, which was in good agreement with the theoretical value at 77 K.

Responsivity decreased sharply after cut-off wavelength and it was two orders of magnitude below the maximum value at 6.0 μm. In the responsivity spectrum, two dips at 3.1 and 4.6 μm can be seen easily. This was due to the absorption peaks of ice in the IR region [88, 89]. Due to leakage in the vacuum, water vapor accumulated on the detector forming ice, which degraded the performance of the detectors. Maximum responsivities of the detectors were

1.00×10^5 V/W and 4.41×10^4 V/W, respectively at 4.35 μm. Both photodetectors had nearly equal current responsivity of 1.8 A/W and 1.7 A/W, respectively which corresponds to 49 % quantum efficiency. We also measured high detectivities for the photodetectors. Peak detectivities of the photodetectors were 3.41×10^9 cm $Hz^{1/2}$/W for 80 μm diameter detector and 7.98×10^9 cm $Hz^{1/2}$/W for 60 μm diameter detector.

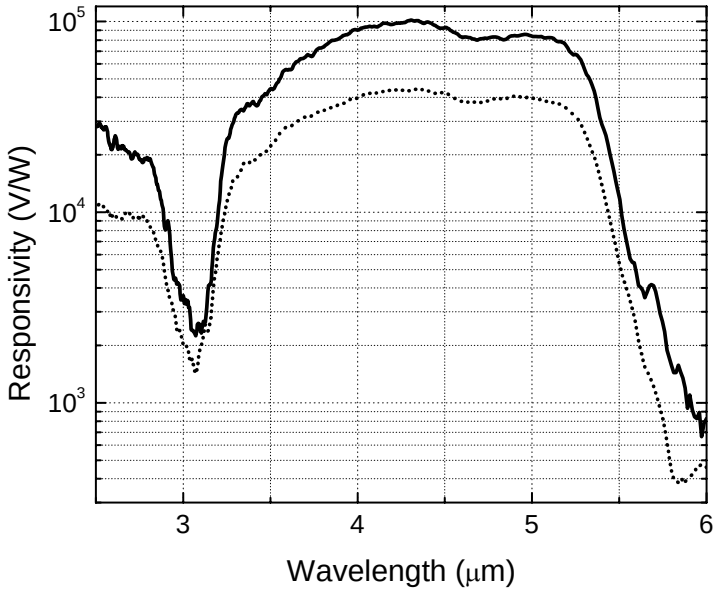

Figure 5.14: Results of the spectral responsivity measurements are shown for 80 μm (solid line) diameter and 60 μm (dotted line) diameter photodetector.

5.3.3 High Speed Characteristics

Due to lack of suitable measurement setup, high-speed measurements had to be done at room temperature. Picosecond full-width at half maximum (FWHM) pulses were generated using a $KTiOAsO_4$ (KTA) based optical parametric oscillator (OPO) at 2500 nm. Figure 5.15 (a) shows the schematics of the OPO.

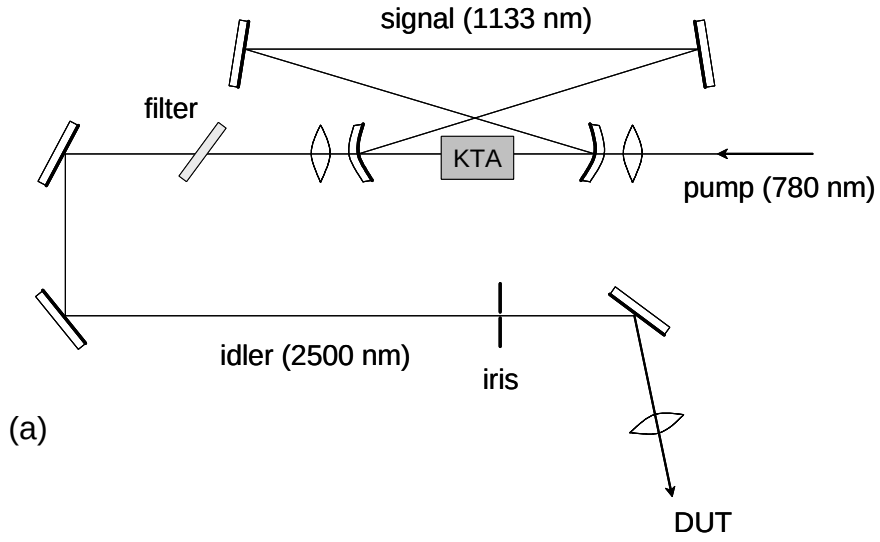

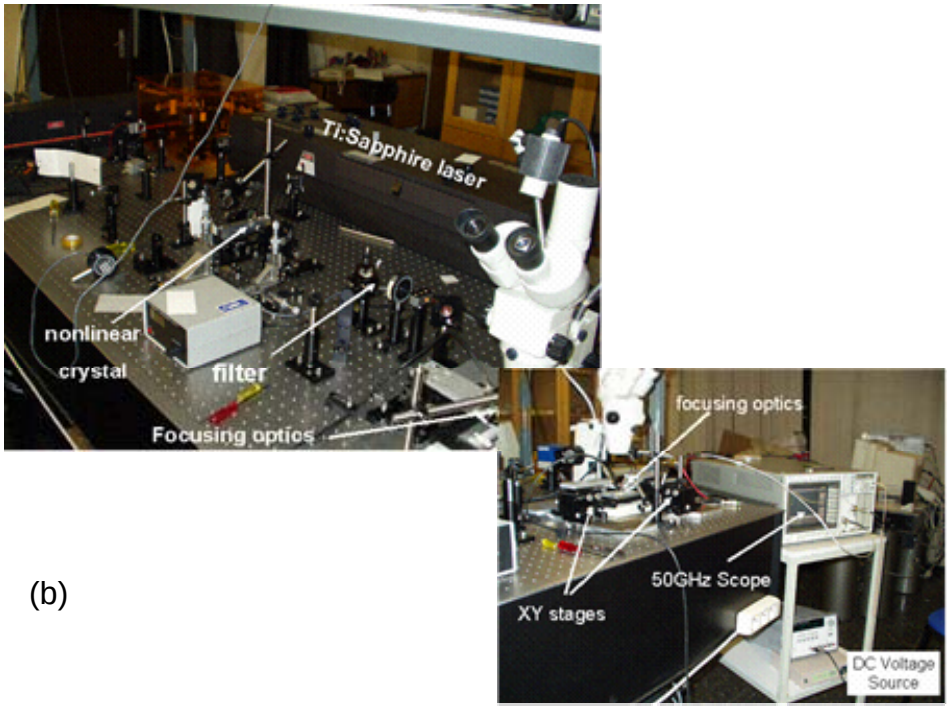

Figure 5.15: (a) The schematic diagram of the optical parametric oscillator, (b) pictures of the experimental setup.

The OPO consisted of an optical resonator with four mirrors that were highly reflective at the signal wavelength and a 20 mm long KTA crystal that

has been cut for non-critical phase matching along the $\theta = 90^o$ and $\phi = 0^o$ direction. Type-II polarization geometry was employed to achieve parametric creation [90]. OPO was pumped by a mode-locked Ti:Sapphire laser operating at 780 nm wavelength with 150 femtosecond FWHM pulses at 76 MHz repetition rate. Figure 5.15 (b) shows the pictures of the experimental setup. Phase matching was achieved yielding a signal at 1133 nm and an idler at around 2500 nm. At the output of the OPO the pump and the signal were filtered out. The idler signal was then focused on the active area of the photodetectors using an iris and infrared lens [68]. These pulses had a 1 picosecond FWHM.

The temporal response of the photodetectors was measured on a 50 GHz sampling scope and the detectors were biased using a 40 GHz bias-tee [91]. Temporal responses of 30 and 60 μm diameter photodetectors were measured as a function of reverse bias. Without bias, the responses had long tails. This tail was due to the diffusion of carriers in the intrinsic region, which could not be depleted without bias at room temperature. With the application of bias voltage, we observed a reduction of the FWHM of the detector responses. At 0.5 V bias, the FWHM values were measured as 59 and 104 psec for 30 and 60 μm diameter photodetectors respectively. After 1 V bias, FWHM values decreased linearly with voltage up to 2.5 V. Measured FWHM values for the detectors biased with 1.0 and 2.5 V were 41 and 33 psec for 30 μm, 65 and 40 psec for 60 μm. Figure 5.16 and figure 5.17 shows the temporal response of the 30 μm and 60 μm diameter photodetectors under 0.5 V, 1.0 V, and 2.5 V biases. For each detector, both the FWHM and the fall time decreased as we increased the bias voltage. Frequency responses of the detectors were calculated using Fast Fourier Transform (FFT). Figure 5.18 (a) and (b) show

the calculated FFT results of the detectors as a function of bias voltage. Figure 5.18 (c) shows the 3-dB bandwidth of the detectors as a function of bias. The linear increase in bandwidth with the bias can be seen easily beyond 1.0 V bias. The maximum bandwidth measured for 30 μm diameter detector was 8.5 GHz. Similar or better high-speed responses are expected when the photodetectors are cooled to 77 K. The detector active area should be depleted easier and the diffusion related slow responses can be eliminated.

Such high-speed infrared photodetectors can be used for optical heterodyne detection and microwave mixing, infrared laser inspection, and free space communication [92, 93]. It is known that mid-IR and far-IR wavelength region (3-5 μm, and 8-14 μm) are better than visible or near infrared regions in terms of transmission and background noise [94].

5.4 Conclusion

This study has shown the high speed operation of InSb based infrared detectors for the first time in scientific literature [83, 95]. These detectors had 49 % peak quantum efficiency at 4.35 μm. Also the detectivity was measured as 7.98×10^{9} cm $Hz^{1/2}/W$ for 60 μm diameter detectors. Finally the 3-dB bandwidth of 30 μm diameter detectors was 8.5 GHz under 2.5 V reverse bias at room temperature.

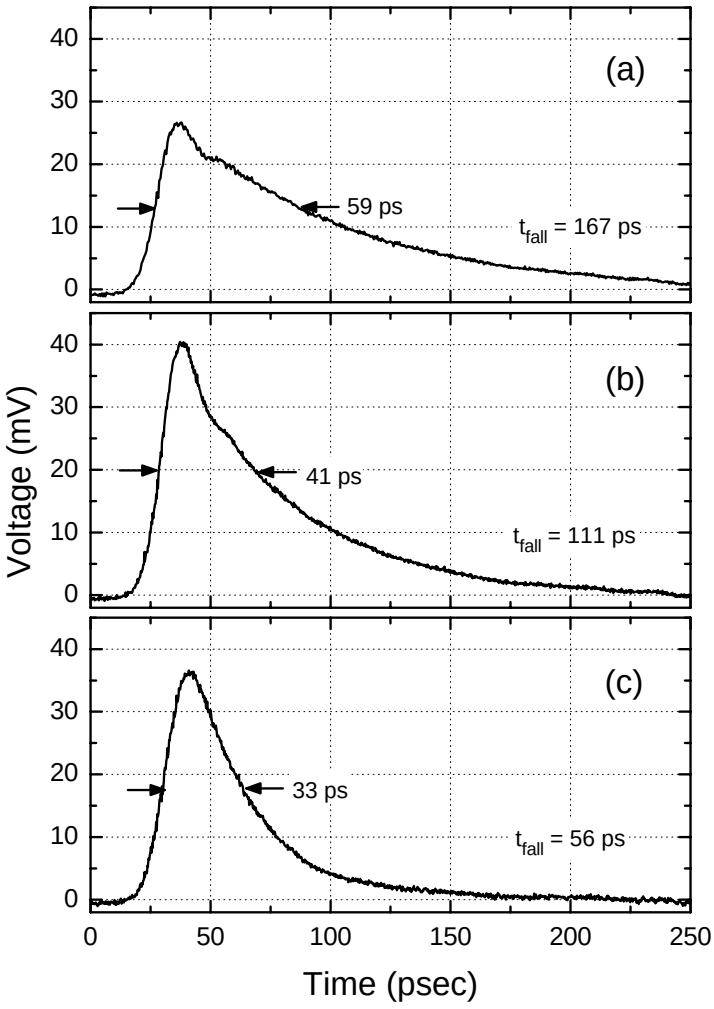

Figure 5.16: Temporal response of a 30 μm diameter detector under (a) 0.5V, (b) 1.0V, and (c) 2.5V bias.

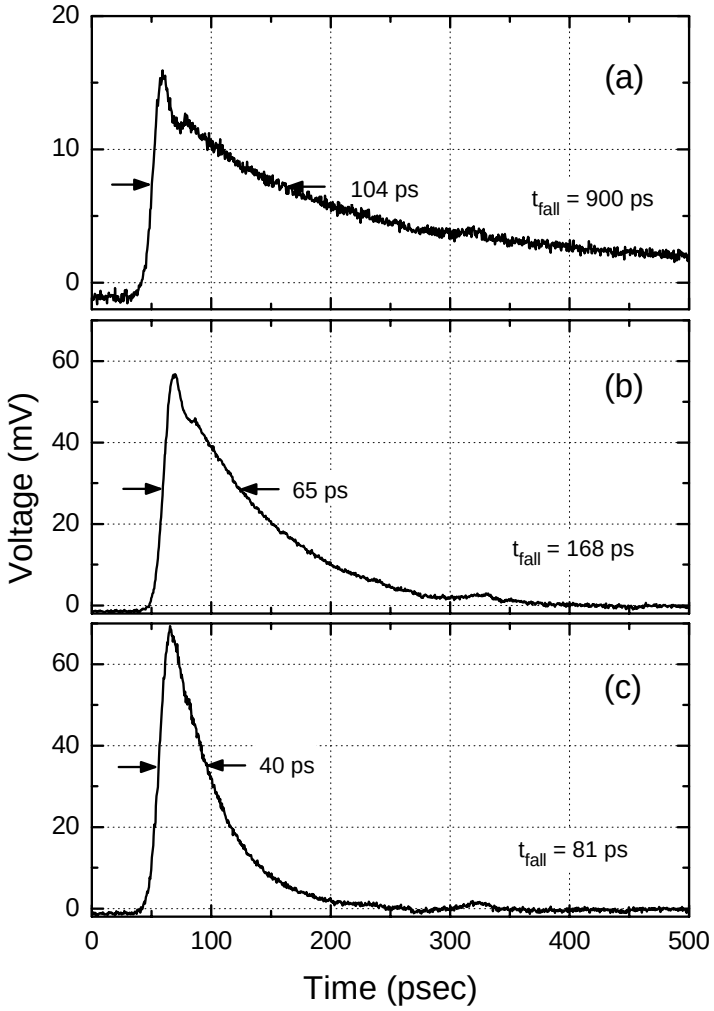

Figure 5.17: Temporal response of a 60 μm diameter detector under (a) 0.5V, (b) 1.0V, and (c) 2.5V bias.

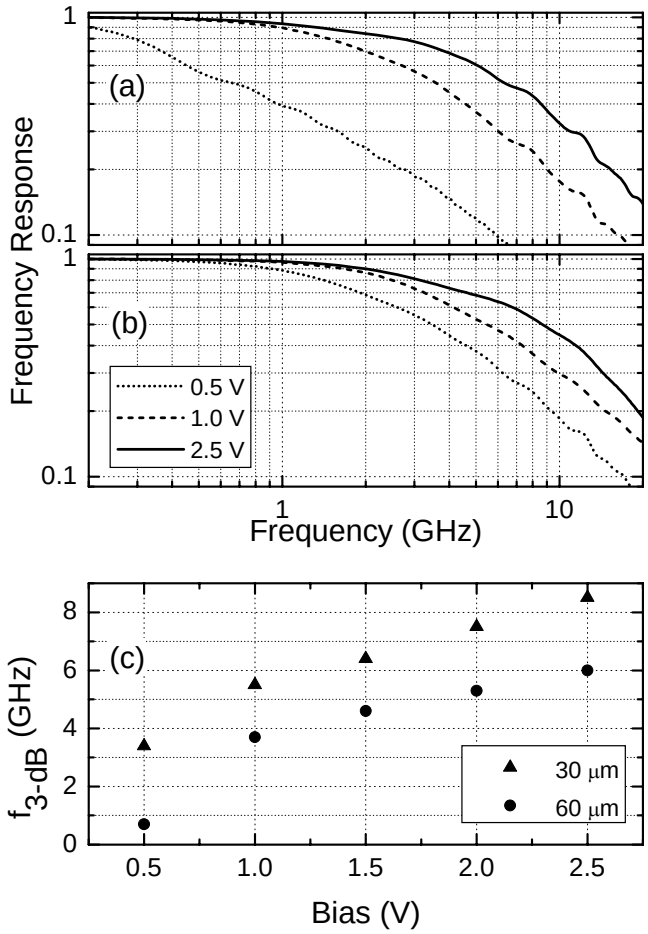

Figure 5.18: Fast Fourier Transform of the temporal responses of the photodetectors. Results for (a) 60 μm diameter and (b) 30 μm diameter photodetectors as a function of bias are shown. (c) 3-dB bandwidth of the 30 and 60 μm diameter photodetectors as a function of applied bias.

Chapter 6
Conclusion and Suggestions for Further Research

This thesis presented the design, fabrication, and characterization of high speed and high efficiency infrared photodetectors. The design steps included detailed material selection and optimization. The electrical properties also kept in mind during the designs. After the growth, the wafers were characterized by optical methods. Microwave compatible fabrication processes were made at Class-100 clean room environment at Bilkent University Department of Physics, while measurement were done at the same laboratory in the Class-10000 clean room environment

The first photodetector was based on InGaAs for the operation around 1550 nm wavelength. The resonant cavity enhancement (RCE) effect was successfully applied to this detector design to improve the quantum efficiency. Measurements showed that the detectors had 66% peak quantum efficiency at 1572 nm, which had 3 fold increases with respect to conventional detector design. The detector had linear response up to 7.4 mW optical power under 4V reverse bias. The high speed characteristics of the detectors showed 31 GHz bandwidth for small area photodetectors. For 10x10 μm^2 area detectors, those had the full optical coupling from a single mode fiber; the 3-dB bandwidth was

measured as 28 GHz under 6V reverse bias. The corresponding bandwidth-efficiency-product (BEP) was 18.5 GHz. Although this was the best BEP for vertical RCE photodetectors, the characteristics of these detectors can be further improved.

1. The p+ ohmic contact resistance was one of the limiting properties for the high speed characteristics of the detectors. When this resistance is lowered, higher bandwidths can be measured from these photodetectors. A solution is to use different alloy for the contact, which would give lower resistances when annealed at 450 ^{o}C.
2. The grading layers can be improved by using material grading between InGaAs and InAlAs layers. This grading can be grown by using different semiconductor layers having energy gap values sorted in increasing order from InGaAs to InAlAs. This would overcome the charge trapping problem at the interfaces.

The second detector was based on InSb. It was intended for operation between 3 and 5 μm wavelengths. The detectors layers were grown on semi-insulating GaAs substrates. Although there were a large lattice mismatch between the substrate and the detector layers, very good electrical and optical characteristics were observed at 77K. The detectors had low dark noise and high differential resistance around zero bias. Also the responsivity measurements showed 49% quantum efficiency. The detectivity was measured as 7.98×10^{9} cm $Hz^{1/2}/W$ for 60 μm diameter detectors. Finally the high speed measurements showed 8.5 and 6.0 GHz bandwidth for 30 μm and 60 μm diameter detectors, respectively. These are the first reported high speed characteristics of InSb based photodetectors in the literature. To improve the

characteristics of these detectors, some modifications can be made during the fabrication and measurements:

1. The high speed characteristics should be measured at 77 K to get the true performance of the detectors. The bandwidth of the detectors must increase at low temperatures, which corresponds to better characteristics in terms of bandwidth.
2. The fabrication must be simplified to increase the fabrication yield. A new mask should be designed without an interconnect metallization along the sidewalls of the mesa. This metallization is hard made with image reversal lithography due to large mesa heights.

In conclusion, the contribution of this research is the development of design and fabrication methods to achieve high speed and highly efficient vertical illuminated photodetectors.

Bibliography

[1] J. S. Kilby, "Turning potential into realities: The invention of the integrated circuit," From "Nobel Lectures, Physics 1996-2000," Editor Gösta Ekspong, (World Scientific Publishing Co., Singapore, 2002).

[2] Z. Alferov, "Double heterostructure lasers: early days and future perspectives," *IEEE. J. Select Topics Quantum Electron.*, **6**, 832 (2000).

[3] D. Keck, "A future full of light," *IEEE. J. Select Topics Quantum Electron.*, **6**, 1254 (2000).

[4] H. Kogelnik, "High-capacity optical communications: personal recollections," *IEEE. J. Select Topics Quantum Electron.*, **6**, 1279 (2000).

[5] G. Cancellieri and F. Chiaraluce, "Recent Progress in Fibre Optics," *Prog. Quant. Elect.*, **18**, 39 (1994).

[6] S. Y. Wang and D. M. Bloom, "100 GHz bandwidth planar GaAs Schottky photodiode," *Electron. Lett.*, **19**, 554 (1983).

[7] E. Ozbay, K. D. Li, and D. M. Bloom, "2.0 psec GaAs monolithic photodetector and all electronic sampler," *IEEE Photon. Tech. Lett.*, **3**, 570 (1991).

[8] K. D. Li, A. S. Hou, E. Ozbay, B. A. Auld, and D. M. Bloom, "2-picosecond, GaAs photodiode optoelectronic circuit for optical correlation applications," *Appl. Phys. Lett.*, **61**, 3104 (1992).

BIBLIOGRAPHY

[9] Y. G. Wey, K. S. Giboney, J. E. Bowers, M. J. Rodwell, P. Silvistre, P. Thiagarajan, and G. Y. Ribbons, "110 GHz GaInAs/InP p-i-n Photodiodes with Integrated Bias Tees and Matched Resistors," *IEEE Photon. Tech. Lett.*, **5**, 1310 (1993).

[10] M. S. Unlu, S. Strite, "Resonant cavity enhanced photonic devices," *J. Appl. Phys.*, **78**, 607 (1995).

[11] W. Schottky, "Halbleitertheorie der Sperrschicht," *Natursissenschaften*, **26**, 843 (1938).

[12] B. L. Sharma, *Metal-Semiconductor Schottky Barrier Junctions and Their Applications* (Plenum Press, 1984).

[13] H. A. Bethe, "Theory of the Boundary Layer of Crystal Rectifiers," *MIT Radiat. Lab. Rep.*, **43-12** (1942).

[14] C. R. Crowell and S. M. Sze, "Current Transport in Metal-Semiconductor Barriers," *Solid State Electron.*, **9**, 1035 (1966).

[15] S. M. Sze, *Physics of Semiconductor Devices* (John Wiley & Sons, New York, 1981).

[16] E. Ozbay, M. S. Islam, B. Onat, M. Gokkavas, O. Aytur, G. Tuttle, E. Towe, R. H. Herderson, M. S. Unlu, "Fabrication of High-Speed Resonant Cavity Enhanced Schottky Photodiodes," *IEEE Photon. Technol. Lett.*, **9**, 672 (1997).

[17] B. M. Onat, M. Gokkavas, E. Ozbay, E. P. Ata, E. Towe, M. S. Unlu, "100-GHz Resonant Cavity Enhanced Schottky Photodiodes," *IEEE Photon. Technol. Lett.*, **10**, 707 (1998).

[18] B. Corbett, L. Considine, S. Walsh and W. M. Kelly, "Narrow bandwith long wavelength resonant cavity photodiodes," *Electron. Lett.*, **29**, 2148 (1993).

[19] A. Srinivasan, S. Murtaza, J. C. Campbell and B. G. Streetman, "High quantum efficiency dual wavelength resonant-cavity photodetector," *Appl. Phys. Lett.*, **66**, 535 (1995).

[20] E. Ozbay, I. Kimukin, N. Biyikli, O. Aytur, M. Gokkavas, G. Ulu, M. S. Unlu, R. P. Mirin, K. A. Bertness, D. H. Christensen, "High-speed >90% quantum-efficiency p-i-n photodiodes with a resonance wavelength adjustable in the 795-835 nm range," *Appl. Phys. Lett.*, **74**, 1072 (1999).

[21] K. A. Anselm, S. S. Mustaza, C. Hu, H. Nie, B. G. Streetman, and J. C. Campbell, "A Resonant-Cavity, Seperate-Apsorption-and-Multiplication, Avalanche Photodiode with Low Excess Noise Factor," *IEEE Electron Dev. Lett.*, **17**, 91 (1997).

[22] H. Nie, A. Anselm, C. Hu, S. S. Mustaza, B. G. Streetman, and J. C. Campbell, "High-speed resonant-cavity seperate absorption and multiplication avalanche photodiodes with 130 GHz gain-bandwith product," *Appl. Phys. Lett.*, **70**, 161 (1997).

[23] P. Yeh, *Optical Waves in Layered Media* (Wiley, New York, 1998).

[24] L. A. Coldren and S. W. Corzine, *Diode Lasers and Photonic Integrated Circuits* (Wiley, New York, 1995).

[25] M. Born and E. Wolf, *Principals of Optics* (Pergamon, 1980).

[26] G. Kinsley, C. Lenox, H. Nie, J. C. Campbell and B. G. Streetman,

"Resonant Cavity Photodetector with Integrated Spectral Notch Filter," *IEEE Photon. Technol. Lett.*, **10**, 1142 (1998).

[27] M. D. Learmouth, N. P. Hewett, I. Reid, M. J. Robertson, "Integrated Dielectric Wavelength Filters on InGaAs PIN Photodetectors," *Electron. Lett.*, **26**, 576 (1990).

[28] T. Baba, S. Tamura, Y. Kokubin, and S. Watanabe, "Monolitic Integration of Multilayer Filter on Vertival Surface of Semicionductor Substrate by a Bias-Sputtering Technique," *IEEE Photon. Technol. Lett.*, **2**, 191 (1990).

[29] Datasheet "AZ 5214 E Image Reversal Photoresist," by Clarient GmbH, Germany available online at www.microchemicals.com.

[30] Imprint "Lithography process, and how to make them more reproducible," by Microchemicals GmbH, Germany available online at www.microchemicals.com.

[31] S. J. Pearton in *InP HBTs: Growth, Processing, and Applications* editors B. Jalali and S. J. Pearton (Artech House, Boston, 1995).

[32] L. Zavieh, C. D. Nordquist, and T. S. Mayer, "Optimization of $In_{0.53}Ga_{0.47}As$ reactive ion etch with CH_4/H_2 using design of experiment methods," *J. Vac. Sci. Technol. B.*, **16**, 1024 (1998).

[33] R. Grover, J. V. Hryniewicz, O. S. King, and V. Van, "Process development of methane-hydrogen-argon-based dry etching of InP for high aspect-ratio structures with facet-quality sidewalls," *J. Vac. Sci. Technol. B.*, **19**, 1694 (2001).

[34] Y. B. Hahn, J. W. Lee, G. A. Vawter, R. J. Shul, C. R. Abernathy, D. C.

Hays, E. S. Lambers, and S. J. Pearton, "Reactive ion beam etching of GaAs ans related compounds in an inductive coupled plasma Cl_2-Ar mixture," *J. Vac. Sci. Technol. B.*, **17**, 366 (1999).

[35] Necmi Biyikli, "High-performance $Al_xGa_{1-x}N$-based UV photodetectors for visible/solar-blind applications," Bilkent University PhD Thesis, May 2004.

[36] Feridun Ay, "Silicon oxynitride layers for applications in optical waveguides," Bilkent University Ms Thesis, September 2000.

[37] Ralph Williams, *Modern GaAs Processing Methods* (Artech House, 1990).

[38] Jin-Wei Shi, Kian-Giap Gan, Yi-Jen Chiu, Chi-Kuang Sun, Ying-Jay Yang, and John E. Bowers, "Metal-semiconductor-metal traveling-wave photodetectors," *IEEE Photon. Technol. Lett.*, **16**, 623 (2001).

[39] I-Hsing Tan, Chi-Kuang Sun, Kirk S. Giboney, John E. Bowers, Evelyn L. Hu, B. I. Miller, and R. J. Capik, "120-GHz long-wavelength low-capacitance photodetector with an air-bridge coplanar metal waveguide," *IEEE Photon. Technol. Lett.*, **7**, 1477 (1995).

[40] E. Drödge, E. H. Böttcher, St. Kollakowski, A. Strittmatter, D. Bimberg, O. Riemann, and R. Steingrüber, "78 GHz InGaAs MSM photodetector," *Electron. Lett.*, vol. 34, no. 23, pp. 2241-2243, 1998.

[41] G. S. Kinsey, C. C. Hansing, A. L. Holmes, Jr., B. G. Streetman, J. C. Campbell, and A. G. Dentai, "Waveguide $In_{0.53}Ga_{0.47}As$-$In_{0.52}Al_{0.48}As$ Avalanche Photodiode," *IEEE Photon. Technol. Lett.*, **12**, 416 (2000).

[42] S. Murthy, T. Jung, T. Chau, M. C. Wu, D. L. Sivco, and A. Y. Cho, "A

novel monolithic distributed traveling-wave photodetector with parallel optical feed," *IEEE Photon. Technol. Lett.*, **12**, 681 (2000).

[43] Y. Hirota, T. Hirono, T. Ishibashi, and H. Ito, "Traveling-wave photodetector for 1.55 μm wavelength fabricated with unitraveling-carrier photodiodes," *Appl. Phys. Lett.*, **78**, 3767 (2001).

[44] K. Kato, A. Kozen, Y. Muramoto, Y. Itaya, T. Nagatsuma, and M. Yaita, "110 GHz 50%-Efficiency Mushroom-Mesa Waveguide p-i-n Photodiode for a 1.55-μm Wavelength," *IEEE Photon. Technol. Lett.*, **6**, 719 (1994).

[45] M. S. Unlu, K. Kishino, J. I. Chyi, L. Arsenault, J. Reed, and H. Morkoc, "Wavelength demultiplexing heterojunction phototransistor," *Electron. Lett.*, **26**, 1857 (1990).

[46] S. S. Murtaza, I. H. Tan, J. E. Bowers, E. H. Lu, K. A. Anselm, M. R. Islam, R. V. Chelakara, R. D. Dupuis, B. G. Streetman, and J. C. Campbell, "High-finesse resonant-cavity photodetectors with an adjustable resonance frequency," *J. Lightwave Technol.*, **14**, 1081 (1996).

[47] H. Nie, K. A. Anselm, C. Hu, S. S. Murtaza, B. G. Streetman, and J. C. Campbell, "High-speed resonant-cavity separate absorption and multiplication avalanche photodiodes with 130 GHz gain-bandwidth product," *Appl. Phys. Lett.*, **70**, 161 (1997).

[48] I. Kimukin, E. Ozbay, N. Biyikli, T. Kartaloğlu, O. Aytür, S. Ünlü, and G. Tuttle, "High-speed GaAs-based resonant-cavity-enhanced 1.3μm photodetector," *Appl. Phys. Lett.*, **77**, 3890 (2000).

[49] N. Biyikli, I. Kimukin, O. Aytur, M. Gokkavas, M. S. Unlu, E. Ozbay, "45-

GHz bandwidth-efficiency resonant-efficiency-enhanced ITO-schottky photodiodes," *IEEE Photon. Technol. Lett.*, **13**, 705 (2001).

[50] A. Strittmatter, S. Kollakowski, E. Drödge, E. H. Böttcher, and D. Bimberg, "High speed, high efficiency resonant-cavity enhanced InGaAs MSM photodetectors," *Electron. Lett.*, **32**, 1231 (1996).

[51] S. M. Spaziani, K. Vaccaro, and J. P. Lorenzo, "High-performance substrate-removal InGaAs Schottky photodetectors," *IEEE Photon. Technol. Lett.*, **10**, 1144 (1998).

[52] S. Y. Hu, J. Ko, and L. A. Coldren, "Resonant-cavity InGaAs/InAlGaAs/InP photodetector arrays for wavelength demultiplexing applications," *Appl. Phys. Lett.*, **70**, 2347 (1997).

[53] W. A. Wohlmuth, J.-W Seo, P. Fay, C. Caneau, and I. Adesida "A high speed ITO-InAlAs-InGaAs Schottky-barrier photodetector," *IEEE Photon. Technol. Lett.*, **9**. 1388 (1997).

[54] C. Lennox, H. Nie, P. Yuan, G. Kinsey, A. L. Holmes, B. G. Streetman, and J. C. Campbell, "Resonant-cavity InGaAs-InAlAs avalanche photodiodes with gain-bandwidth product of 290 GHz," *IEEE Photon. Technol. Lett.*, **11**, 1162 (1999).

[55] S. S. Murtaza, I-H Tan, R. V. Chelakara, M. R. Islam, A. Srinivasan, K. A. Anselm, J. E. Bowers, E. L. Hu, R. D. Dupuis, B. G. Streetman, J. C. Campbell, "High-efficiency, dual wavelength wafer-fused resoanat-cavity photodetector operating at long wavelengths," *IEEE Photon. Technol. Lett.*, **7**, 679 (1995).

[56] Th. Engel, E. Drodge, G. Unterborsch, E. H. Bottcher, and D> Blimberg,

"Reactive matching of millimeter-wave photodetectors using coplanar waveguide technology," *Electron. Lett.*, **34**, 1690 (1998).

[57] M. Horstmann, K. Schimpf, M. Marso, A. Fox, and P. Kordos, "16 GHz bandwidth MSM photodetector and 45/85 f_T/f_{max} HEMT prepared on an identical InGaAs/InP layer structure," *Electron. Lett.*, **32**, 763 (1996).

[58] J. H. Kim, H. T. Griem, R. A. Friedman, E. Y. Chan, ands. Ray, "High-performance bak-illuminated InGaAs/InP MSM photodetector with a record responsivity of 0.96 A/W," *IEEE Photon. Technol. Lett.*, **11**, 1241 (1992).

[59] T. Chau, L. Fan, D. T. K. Tong, S. Mathai, M. C. Wu, D. L. Sivco, and A. Y. Cho, "long wavelength velocity matched distributed photodetectors for RF fibre optic links," *Electron. Lett.*, **34**, 1422 (1998).

[60] M. S. Islam, S. Murthy, T. Itoh, M.C. Wu, D. Novak, R. Waterhouse, D.L. Sivco, and A.Y. Cho, "Velocity-matched distributed Photodetectors and Balanced Photodetectors with p-i-n Photodiodes," *IEEE Trans. Microwave Theory Tech.*, **49**, 1914 (2001).

[61] O. Madelung, *Semiconductors – Basic Data* (Springer, Berlin, 1996).

[62] D. A. Humphreys, R. J. King, D. Jenkins, and A. J. Moseley, "Measurement of absorption coefficients of $Ga_{0.47}In_{0.53}As$ over the wavelength range 1.0-1.7 μm," *Electron. Lett.*, **21**, 1187 (1985).

[63] O. Blum, I. J. Fritz, L. R. Dawson, A. J. Howard, T. J. Headley, J. F. Klem, and T. J. Drummond, "Highly reflective, long wavelength AlAsSb/GaAsSb distributed Bragg reflector grown by molecular beam epitaxy in InP substrates," *Appl. Phys. Lett.*, **66**, 329 (1995).

[64] Sadao Adachi, "Refractive indices of III-V compounds: Key properties of InGaAsP relevant to device design," *J. Appl. Phys.*, **53**, 5863 (1982).

[65] Sadao Adachi, "Optical dispersion relations for GaP, GaAs, GaSb, InP, InAs, InSb, $Al_xGa_{1-x}As$, and $In_{1-x}Ga_xAs_yP_{1-y}$," *J. Appl. Phys.*, **66**, 6030 (1989).

[66] A. J. Moseley, J. Thompson, D. J. Robbins, and M. Q. Kearly, "High-reflectivity AlGaInAs/InP multilayer mirrors grown by low-pressure MOVPE for application to long-wavelength high-contrast-ratio multi-quantum-well modulators," *Electron. Lett.*, **25**, 1717 (1989).

[67] J. –Ph. Debray, N. Bouché, G. Le Roux, R. Raj, and M. Quillec, "Monolithic vertical cavity device lasing at 1.55μm in InGaAlAs system," *Electron. Lett.*, **33**, 868 (1997).

[68] M. Guden, and J. Piprek, "Material parameters of quaternary III-V semiconductors for multilayer mirrors and 1.55 μm wavelength," *Modelling Simul. Mater. Sci. Eng.*, 4, 349 (1996).

[69] Y. Takeda, in *InP-Based Materials and Devices: Physics and Technology* edited by O. Wada, and H. Hasegawa (John Wiley & Sons, Inc., New York, 1999).

[70] M. J. Mondry, D. I. Babic, J. E. Bowers, and L. A. Coldren, "Refractive indexes of (Al, Ga, In)As epilayers on InP for optoelectronic applications," *IEEE Photon. Tech. Lett.*, **4**, 627 (1992).

[71] C.C. Barron, C.J. Mahon, B.J. Thibeault, G. Wang, W. Jiang, L.A. Coldren, and J.E. Bowers, "Resonant-cavity-enhanced pin photodetector with 17

GHz bandwidth-efficiency product," *Electron. Lett.*, **30**, 1796 (1994).

[72] Newport Online Catalog. 818 Series Cylindrical detectors. [Online]. Available: http://www.newport.com.

[73] L. Y. Lin, M. C. Wu, T. Itoh, T. A. Vang, R. E. Muller, D. L. Sivco, and A. Y. Cho, "High-power high-speed photodetectors-Design, analysis, and experimental demonstration," *IEEE Trans. Microwave Theory. Tech.*, **45**, 1320 (1997).

[74] C. Lennox, H. Nie, G. Kinsey, P. Yuan, A. L. Holmes, Jr., B. G. Streetman, and J. C. Campbell, "Improved optical response of superlattice graded InAlAs/InGaAs p-i-n photodetectors," *Appl. Phys. Lett.*, **73**, 3405 (1998).

[75] A. Rogalski, "Quantum well photoconductors in infrared detector technology," *J. Appl. Phys.*, **93**, 4355 (2003).

[76] J. J. Lee, J. D. Kim, and M. Razeghi, "Growth and characterization of InSbBi for longwavelength infrared photodetectors," *Appl. Phys. Lett.*, **70**, 3266 (1997).

[77] J. D. Kim, S. Kim, D. Wu, J. Wojkowski, J. Xu, J. Piotrawski, E. Bigan, and M. Razeghi, "8-13 μm InAsSb heterojunction photodiode operating at near room temperature," *Appl. Phys. Lett.*, **67**, 2645 (1995).

[78] T. Ashley, A. B. Dean, C. T. Elliott, C. F. McConville, and C. R. Whitehouse, "Molecular-beam growth of homoepitaxial InSb photovoltaic detectors," *Electron. Lett.*, **24**, 1270 (1988).

[79] A. Rakovska, V. Berger, X. Marcadet, B. Vinter, G. Glestre, T. Oksenhendler, and D. Kaplan, "Room temperature InAsSb photovoltaic

midinfrared detector," *Appl. Phys. Lett.*, **77**, 397 (2000).

[80] D. T. Cheung, A. M. Andrews, E. R. Gertner, G. M. Williams, J. E. Clarke, J. G. Pasko, and J. T. Longo, "Backside-illuminated $InAs_{1-x}Sb_x$-InAs narrow-band photodetectors," *Appl. Phys. Lett.*, **30**, 587 (1977).

[81] S. Ozer and C. Besikci, "Assessment of InSb photodetectors on Si substarate," *J. Phys. D: Appl. Phys.*, **36**, 559 (2003).

[82] C. Besikci, S. Ozer, C. V. Hoof, L. Zimmermann, J. John, and P. Merken, "Characteristics of $InAs_{0.8}Sb_{0.2}$ photodetectors on GaAs substarate," *Semicond. Sci. Technol.*, **16**, 992 (2001).

[83] I. Kimukin, N. Biyikli, and E. Ozbay, "InSb high-speed photodetectors grown on GaAs substrate," *J. Appl. Lett.*, **94**, 5414 (2003).

[84] E. Michel, J. Xu, J. D. Kim, I. Ferguson, and M. Razeghi, "InSb infrared photodetectors on Si substrates grown by molecular beam epitaxy," *IEEE Photon. Tech. Lett.*, **8**, 673 (1996).

[85] A. Tevke, C. Besikci, C. V. Hoof, and G. Borghs, "InSb infrared p-i-n photodetectors grown on GaAs coated Si substrate by molecular beam epitaxy," *Solid-State Electron.*, **42**, 1039 (1998).

[86] Edward D. Palik, *Handbook of Optical Constants of Solids* (Academic Press, Orlando, 1998), Vol. 1.

[87] T. S. Moss, in *Semiconductors and Semimetals*, edited by R. K. Willardson, and A. C. Beer, (Academic Press, New York, 1966), Vol. 2.

[88] S. G. Warren, "Optical constants of ice from ultraviolet to the microwave," *Appl. Opt.*, **23**, 1206 (1984).

[89] David M. Wieliczka, Shengshan Weng, and Marvin R. Querry, "Wedge shaped cell for highly absorbent liquids: infrared optical constants of water," *Appl. Opt.*, **28**, 1714 (1989).

[90] T. Kartaloğlu and O. Aytür, "Femtosecond self-doubling optical parametric oscillator based on KTiOAsO4," *IEEE J. Quantum. Electron.*, **39**, 65 (2003).

[91] I. Kimukin, N. Biyikli, B. Butun, O. Aytur, S. Ünlü, and E. Ozbay, " InGaAs Based High Performance p-i-n Photodiodes," *IEEE Photon. Tech. Lett.*, **14**, 366 (2002).

[92] E. R. Brown, K. A. McIntosh, F. W. Smith, and M. J. Manfa, "Coherent detection with GaAs/AlGaAs multiple quantum well structure," *Appl. Phys. Lett.*, **62**, 1513 (1993).

[93] H. C. Liu, G. E. Jenkins, E. R. Brown, K. A. McIntosh, K. B. Nichols, and M. J. Manfra, "Optical heterodyne detection and microwave rectification up to 26 GHz using quantum well infrared photodetectors," *IEEE Electron. Device Lett.*, **16**, 253 (1995).

[94] H. Manor and S. Arnon, "Performance of an optical wireless communication as a function of wavelength," *Appl. Opt.*, **42**, 4285 (2003).

[95] I. Kimukin, N. Biyikli, T. Kartaloglu, O. Aytur, and E. Ozbay, "High-speed InSb photodetectors on GaAs for Mid-IR applications," *IEEE. J. Select Topics Quantum Electron.*, **10**, 759 (2004).

Appendix A

Frequency Response calculation for a photodetector

Based on the results by Barron et. al. (IEE Electron. Lett. vol.30 p.1796)

```
Clear[f];
sinc[x_] := N[Sin[x] / x];
ϵ0 = 8.85 * 10^-14;
ϵ = 12;
μ = 1 * 10^-4;
fRC[d_, A_, R_] := 1.73 / (2 * Pi * R * (ϵ * ϵ0 * A / d));

(* Transit time for electron and hole *)
te = 4.9 10^-12;
th = 7.6 10^-12;

(* Capacitance limited frequency for the 50 ohm load *)
frc = fRC[0.47 * μ, 200 * μ^2, 50];
Print["  RC frequency = ", frc];

(* find the 3-dB frequency of the photodetector *)
f3dB = FindRoot[2 == (sinc[Pi * f * te]^2 + sinc[Pi * f * th]^2)^2 / (1 + f^2 / frc^2),
    {f, 5 * 10^9}][[1, 2]];
Print["3-dB frequency = ", f3dB];
```

```
  RC frequency = 1.21854×10^11
3-dB frequency = 4.55337×10^10
```

Appendix B

TMM based detector design

This program is used during the design of the InGaAs based 1550nm pin RCE photodetector

```
(* read the program file used for normal incidance *)
<<"c:/ibrahim/mathematica/newoblique/normal.txt";

(* set the calculation parameters *)
InitialWavelength=1400;
FinalWavelength=1700;
NumberOfWavelength=301;
DataFileDirectory="c:/ibrahim/mathematica/material-data/";
Layers={
      {"air", 0},
      {DBR, 0, {"si3n4", 223}, {"sio2", 267} },
      {"ingaas",  40},
      {"inalas", 310},
      {"ingaas", 300},
      {"inalas", 630},
      {DBR, 25, {"inalas", 121}, {"inalgaas", 112} },
      {"inp", 0}
      };

(* calculate the electric field values *)
InitializeStructure[];

(* Reflectivity calculation for the grown wafer *)
refle=FindReflection[];
ListPlot[refle,PlotJoined→True,PlotStyle→{RGBColor[0,0,1]},Fram
e→True,FrameLabel→{"Wavelength (nm)","Reflectivity (%)"},
PlotLabel->"Calculation  for the reflectivity of InGaAs RCE pin
wafer", TextStyle->{FontFamily→"Arial",FontSize→12},
ImageSize→550,
GridLines→{{Automatic,Dashing[{0.0075}]},{Automatic,Dashing[{0.
0075}]}}];
```

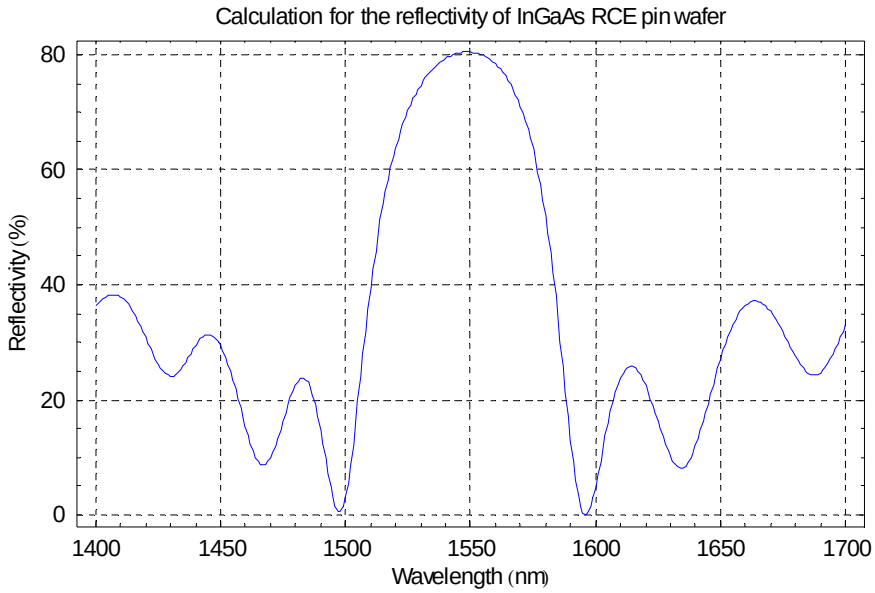

Find the properties of the photodetector after the process is over and the tuning done

```
(* make the simulation for the new thickness of the layers *)
Layers={
      {"air", 0},
      {DBR, 0, {"si3n4", 223}, {"sio2", 267} },
      {"ingaas",     0},
      {"inalas", 245},
      {"ingaas", 300},
      {"inalas", 630},
      {DBR, 25, {"inalas", 121}, {"inalgaas", 112} },
      {"inp", 0}
      };
InitializeStructure[];

refle=FindReflection[];
ListPlot[refle,PlotJoined→True,PlotRange→{-
1,81},PlotStyle→{RGBColor[0,0,1]},Frame→True,FrameLabel→{"Wavel
ength (nm)","Reflectivity (%)"}, PlotLabel->"Calculation  for
the reflectivity of InGaAs RCE pin Photodetector", TextStyle-
>{FontFamily→"Arial",FontSize→12}, ImageSize→550,
GridLines→{{Automatic,Dashing[{0.0075}]},{Automatic,Dashing[{0.
0075}]}}];
```

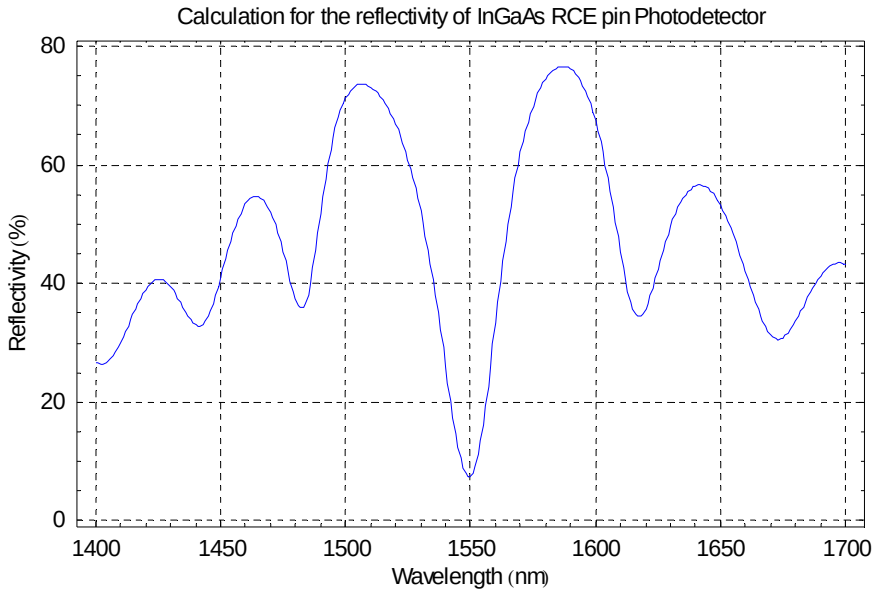


```
abso=FindAbsorption[5];
ListPlot[abso,PlotJoined→True,PlotRange→{-
1,81},PlotStyle→{RGBColor[0,0,1]},Frame→True,FrameLabel→{"Wavel
ength (nm)","Quantum Efficiency (%)"}, PlotLabel->"Calculation
for the QE of InGaAs RCE pin Photodetector", TextStyle-
>{FontFamily→"Arial",FontSize→12}, ImageSize→550,
GridLines→{{Automatic,Dashing[{0.0075}]},{Automatic,Dashing[{0.
0075}]}}];
```

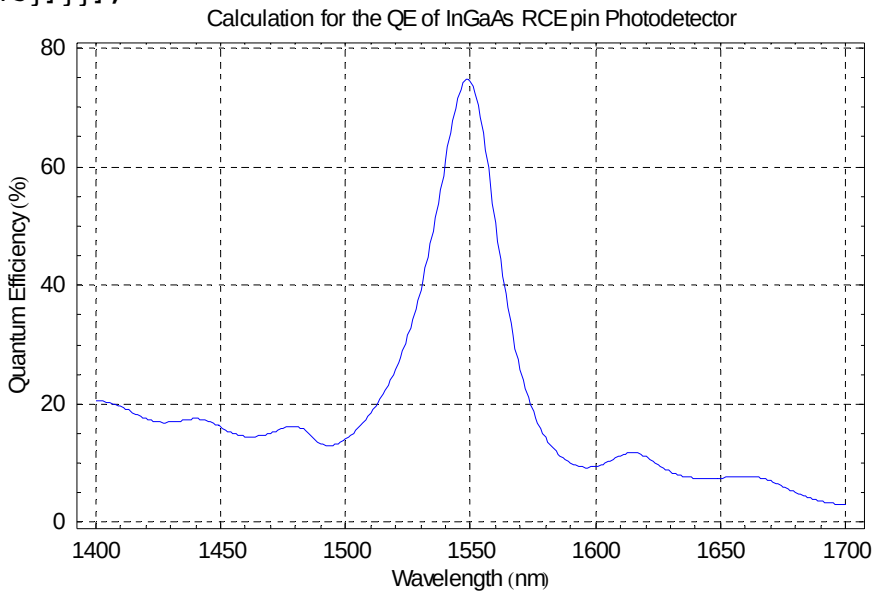


```
trans=FindTransmission[8];
```

```
ListPlot[trans,PlotJoined→True,PlotRange→{-1,81},
PlotStyle→{RGBColor[0,0,1]},Frame→True,FrameLabel→{"Wavelength
(nm)","Transmittivity (%)"}, PlotLabel->"Calculation  for the
transmittivity of InGaAs RCE pin Photodetector", TextStyle-
>{FontFamily→"Arial",FontSize→12}, ImageSize→550,
GridLines→{{Automatic,Dashing[{0.0075}]},{Automatic,Dashing[{0.
0075}]}}];
```

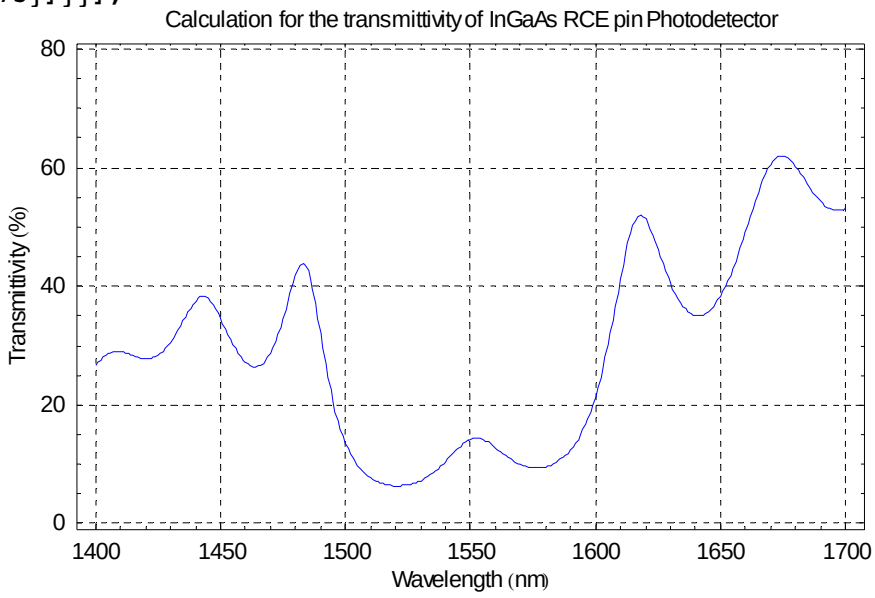

Appendix C

List of Publications

Our work on RCE photodetectors were mostly in the infrared region. This work started with GaAs based photodetectors operating around 800 nm, and we continued up to 1550 nm for different applications. The related publications with increasing operating wavelength are as follows:

1. Ekmel Ozbay, Ibrahim Kimukin and Necmi Biyikli, "Ultrafast & Highly Efficient Resonant Cavity Enhanced Photodiodes," Materials Science Forum, volume 384-385, p. 241 (2002).
2. Ekmel Ozbay, Ibrahim Kimukin, Necmi Biyikli, Orhan Aytür, Mutlu Gökkavas, Gökhan Ulu, R. Mirin, D. H. Christensen, and M.Selim Ünlü, "High-Speed >90% Quantum-Efficiency p-i-n Photodiodes with a Resonance Wavelength Adjustable in 795-835 nm Range," Applied Physics Letters , volume 74, p. 1072 (1999).
3. Necmi Biyikli, Ibrahim Kimukin, Orhan Aytür, Mutlu Gokkavas, Selim Ünlü, Ekmel Ozbay, "45-GHz Bandwidth-Efficiency Resonant-Cavity-Enhanced ITO-Schottky Photodiodes," IEEE Photonics Technology Letters , volume 13, p. 705 (2001).
4. Ibrahim Kimukin, Ekmel Ozbay, Necmi Biyikli, Tolga Kartaloglu, Orhan Aytür, Selim Ünlü, Gary Tutle, "High-speed GaAs-based

resonant-cavity-enhanced 1.3μm photodetector," Applied Physics Letters , volume 77, p. 3890 (2000).

5. Bayram Butun, Necmi Biyikli, Ibrahim Kimukin, Orhan Aytur, Ekmel Ozbay, P. A. Postigo, J. P. Silveira, and A. R. Alija, "High-speed 1.55 μm operation of low-temperature-grown GaAs-based resonant-cavity-enhanced p-i-n photodiodes," Applied Physice Letters, volume 84, p. 4185 (2004).
6. Ibrahim Kimukin, Necmi Biyikli, Bayram Butun, Orhan Aytur, Selim Unlu, Ekmel Ozbay, "InGaAs Based High Performance p-i-n Photodiodes," IEEE Photonics Technology Letters, volume 14, p. 366 (2002).

The publications for InSb based photodetectors are:

7. Ibrahim Kimukin, Necmi Biyikli, and Ekmel Ozbay, "InSb high-speed photodetectors grown on GaAs substrate," Journal of Applied Physics, volume 94, p. 5414 (2003).
8. Ibrahim Kimukin, Necmi Biyikli, Tolga Kartaloglu, Orhan Aytur, and Ekmel Ozbay, "High-speed InSb photodetectors on GaAs for Mid-IR applications," IEEE Journal of Selected Topics in Quantum Electronics, volume 10, issue 4, p. 766 (2004).

In addition to infrared photodetectors, I also work on wide band-gap semiconductors, especially GaN based photodetectors. My work was mostly on the design, characterization, and initial process development for GaN based structures. Our publications are as follows in chronological order:

9. Necmi Biyikli, Tolga Kartaloglu, Orhan Aytur, Ibrahim Kimukin, Ekmel Ozbay, "High-speed visible-blind GaN-based indium–tin–oxide

Schottky photodiodes," Applied Physics Letters, volume 79, p. 2838 (2001).

10. Necmi Biyikli, Orhan Aytur, Ibrahim Kimukin, Turgut Tut, Ekmel Ozbay, "Solar-blind AlGaN-based Schottky photodiodes with low noise and high detectivity", Applied Physics Letters, volume 81, p. 3272 (2002).
11. Necmi Biyikli, Tolga Kartaloglu, Orhan Aytur, Ibrahim Kimukin, Ekmel Ozbay, "High-Performance Solar-Blind AlGaN Schottky Photodiodes," MRS Internet Journal of Nitride Semiconductor Research, volume 8, p. 2 (2003).
12. Necmi Biyikli, Ibrahim Kimukin, Tolga Kartaloglu, Orhan Aytur, Ekmel Ozbay, "High-speed Solar-Blind photodetectors with indium-tin-oxide Schottky contacts," Applied Physics Letters, volume 82, p. 2344 (2003).
13. Necmi Biyikli, Tolga Kartaloglu, Orhan Aytur, Ibrahim Kimukin, Ekmel Ozbay, "High-Speed Visible-Blind Resonant Cavity Enhanced AlGaN Schottky Photodiodes," MRS Internet Journal of Nitride Semiconductor Research, volume 8, p. 8 (2003).
14. Necmi Biyikli, Ibrahim Kimukin, Tolga Kartaloglu, Orhan Aytur, Ekmel Ozbay, "High-Speed Colar-Blind AlGaN-based metal-semiconductor-metal photodetectors," Physics Status Solidi C, volume 0, p. 2314 (2003).
15. Necmi Biyikli, Ibrahim Kimukin, Orhan Aytur, Ekmel Ozbay, "Solar-blind AlGaN-based p-i-n photodiodes with low dark current and high detectivity," IEEE Photonics Technology Letters, volume 16, p. 1718 (2004).

16. Necmi Biyikli, Ibrahim Kimukin, Turgut Tut, Tolga Kartaloglu, Orhan Aytur, Ekmel Ozbay, "High-speed characterization of solar-blind Al(x)Ga(1-x)N p-i-n photodiodes," Semiconductor Science and Technology, volume 19, p. 1259 (2004).
17. Ekmel Ozbay, Necmi Biyikli, Ibrahim Kimukin, T. Tut, T. Kartaloglu, and Orhan Aytur, "High-Performance Solar-Blind Photodetectors Based on Al(x)Ga(1-x)N Heterostructures," IEEE Journal of Selected Topics in Quantum Electronics, volume 10, issue 4, p. 742 (2004).
18. Necmi Biyikli, Ibrahim Kimukin, Bayram Butun, Orhan Aytur, and Ekmel Ozbay, "ITO-Schottky Photodiodes for High-Performance Detection in the UV-IR Spectrum," IEEE Journal of Selected Topics in Quantum Electronics, volume 10, issue 4, p. 759 (2004).
19. Turgut Tut, Necmi Biyikli, Ibrahim Kimukin, Tolga Kartaloglu, Orhan Aytur, M. Selim Unlu, and Ekmel Ozbay, "High bandwidth-efficiency solar-blind AlGaN Schottky photodiodes with low dark current," Solid State Electronics, volume 49, issue 1, p. 117 (2005).